Liquid exfoliation of layered metal oxides and their Langmuir-Blodgett films

Huiyu Yuan

Ph. D. committee

Chairman

Prof. dr. ir. H. Hilgenkamp	University of Twente

Promotor

Prof. dr. ir. J. E. ten Elshof	University of Twente

Members

Prof. dr. G. H. Gelinck	Eindhoven University of Technology
Prof. dr. F. M. Mulder	Delft University of Technology
Prof. dr. ir. P. Jonkheijm	University of Twente
Prof. dr. ir. R.G.H. Lammertink	University of Twente
Prof. dr. ir. G. Koster	University of Twente

Cover: Front cover shows an artistic impression of rapid exfoliation of layered metal oxides driven by acid-base reaction. Back cover presents an atomic force microscopic image of a Langmuir-Blodgett film of titanate nanosheets. The background image is a photograph of leaves floating on water, taken in the Volkspark, Enschede, symbolizing the nanosheets at the liquid-air interface.

The research described in this thesis was carried out in the Inorganic Materials Science group within the faculty of science and technology, and the MESA+ Institute for Nanotechnology at the University of Twente. This work was financially supported by the Chemical Sciences division of the Netherlands Organization for Scientific Research (NWO-CW) and China Scholarship Council (CSC, No.2011704003).

Liquid Exfoliation of Layered Metal Oxides and Their Langmuir-Blodgett Films
Ph.D. Thesis, University of Twente, Enschede, The Netherlands
Printed by Gildeprint drukkerijen, Enschede, The Netherlands

ISBN: 978-90-365-4012-4
DOI: 10.3990/1.9789036540124

LIQUID EXFOLIATION OF LAYERED METAL OXIDES AND THEIR LANGMUIR-BLODGETT FILMS

DISSERTATION

to obtain

the degree of doctor at the University of Twente,

on the authority of the rector magnificus,

Prof. dr. H. Brinksma,

on account of the decision of the graduation committee,

to be publicly defended

on Thursday, 28 January 2016, at 14:45

by

Huiyu Yuan

born on 20 April 1986

in Henan, China

This dissertation has been approved by the promotor:

Prof. dr. ir. J. E. ten Elshof

Dedicated to my beloved family

and

my dear supervisor Prof. dr. ir. J. E. ten Elshof

Table of Contents

Chapter 1

Introduction

A brief introduction of the research on two dimensional materials (nanosheets), especially metal oxide nanosheets is presented in this chapter. A synthesis strategy of metal oxide nanosheets is introduced. The scope and outline of this thesis are described at the end of the chapter.

1.1 RISE OF TWO DIMENSIONAL MATERIALS

The development of human society relies on the evolution of materials science. In the modern society, the development of technology is more critical to its materials so that its importance becomes more obvious. New functional materials are the “gold” human society is pursuing. In the last decade, what is the super star in materials science? Undoubtedly, it is graphene, an atomically thin two-dimensional (2D) carbon material. The discovery of graphene has initiated intensive research on this 2D material since 2004 and led to the Nobel Prize for Andre Geim and Konstantin Novoselov, who first isolated graphene from graphite.[1,2] This single atomic layer of carbon has surprised us with its exotic properties due to its 2D structure.[3] The rise of graphene also brings a class of materials, so called 2D materials or nanosheets, to the frontier of materials science.[4-6] Figure 1 shows some samples of 2D materials including graphene. A common feature of 2D materials is their extremely high aspect ratio with thicknesses of nanometers in one dimension and micrometers in the other dimensions. From the point of view of morphology one may regard 2D materials as a bed sheet on nanometer scale. Although 2D materials include 2D organic nanosheets,[7,8] the nanosheets mentioned in this thesis will refer to inorganic substances.

Figure 1. Crystal structures, naturally occurring forms, and exfoliated products of four examples of layered materials. (**A**) Graphite, (**B**) is a naturally occurring mineral, and (**C**) is graphene. (**D**) Vermiculite (typically $Mg_{1.8}Fe_{0.9}Al_{4.3}SiO_{10}(OH)_2 \cdot 4(H_2O)$, (**E**) is found naturally as a mineral and (**F**) can be exfoliated. (**G**) MoS_2, (**H**) is found naturally as the mineral molybdenite and (**I**) MoS_2 monolayers. (**J**) Layered manganese dioxide, (**K**) as birnessite and (**L**) MnO_2 nanosheets. This picture is adapted from ref. (*14*). Reprinted with permission from AAAS.

2D materials are attracting much attention because of their interesting properties. Take graphene as an example: graphene is the thinnest material but also the strongest material ever tested.[9] Besides graphene, other nanosheets also show interesting properties for different applications. For example, 2D titanium carbide delaminated from MAX phases show extraordinary performances as supercapacitor electrodes;[10]

MoS_2 nanosheets exhibit excellent electrocatalytic performance for hydrogen evolution.[11] Metal oxides nanosheets are promising candidates for nanoelectronics.[12]

1.2 STATE OF THE ART IN EXFOLIATION

Nanosheets are normally isolated from their parent layered compounds, which typically have strong covalent or ionic in-plane bonds and weak Van der Waals or electrostatic out-of-plane interactions.[13] This process is called exfoliation or delamination, see schematic diagram in Figure 2. Besides graphite, several groups of inorganic layered compounds have been reported to have been exfoliated successfully, such as metal oxides, clays, layered metal dichalcogenides, layered double hydroxides, and MAX phases.[14] In order to exfoliate these layered compounds, different approaches have been applied depending on the interaction force between the host layers. For graphite, MAX phases and layered metal dichalcogenides, the current exfoliation methods are manual mechanical exfoliation,[1] ultrasonication-assisted solvent exfoliation[15, 16] and the lithium intercalation exfoliation method.[17] For layered metal oxides, clays, and layered double hydroxides, ion intercalation-based exfoliation is generally used.[13, 14]

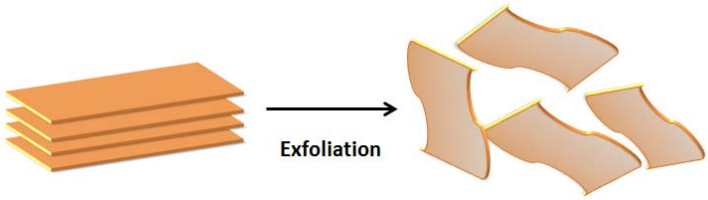

Figure 2. Schematic diagram of exfoliation of layered materials.

Even though all of the exfoliation methods have been serving for years in the laboratory, their potential on the industrial scale is limited. For example, ultrasonication assisted solvent exfoliation is struggling with inhomogeneity of the exfoliation process and damage to the nanosheets.[14] The lithium intercalation exfoliation method produces a high yield of nanosheets, but it needs a complex system.[17] The ion intercalation-based exfoliation produces high yields of monolayer nanosheets and no damage is induced in the exfoliation process.[13] This method is easy to scale-up because it's driven by chemical reaction, which makes it a promising

route for industry. However, the exfoliation has been regarded as a slow process and normally takes several weeks to complete.[14, 18]

1.3 GENERAL CONCEPT OF ION INTERCALATION-BASED EXFOLIATION

A promising approach for industrial scale processing is ion intercalation-based exfoliation, which can be utilized in the synthesis of a large group of inorganic layered materials, such as metal (hydro)oxides including more than 30 different compounds.[14] Key to exfoliate these layered compounds is the weakening of the electrostatic interactions between the layers and the disassembly of the ordered layered structure into single individual sheets.[19] Especially layered titanates $Cs_{0.7}Ti_{1.825}O_4$ (CTO) have been intensively studied as a model compound in order to gain insight into the details of the exfoliation of layered metal oxides in general.[19-22] The well-established concept is that first the layered metal oxides are protonated, and then the protons are exchanged for bulky organic species, for example, tetra *n*-butylammonium ions (TBA^+) to separate the layers. Figure 3 sketches the procedure taking CTO as an example.[22]

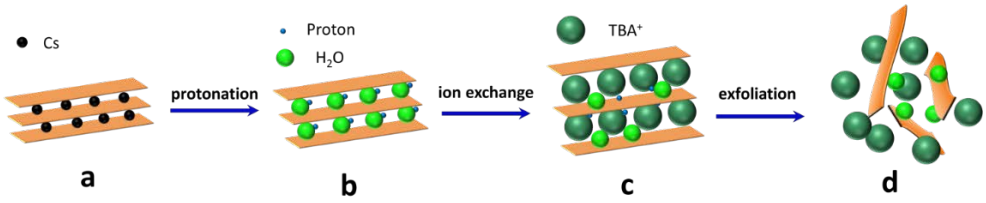

Figure 3. Schematic diagram of ion intercalation-based exfoliation.

This generally accepted mechanism involves the layered structure to swell due to hydration in aqueous media containing TBA^+ ions (Figure 3b → c), and the degree of swelling depends on the electrolyte (TBA^+) concentration.[22] When the amount of TBA^+ ions is insufficient to cover the surface of the titanate sheets, intercalation occurs. A TBA^+ content approximately half the equivalent of the exchangeable protons has been found to be a lower threshold for delamination (Figure 3c → d) below which only the usual intercalation reaction occurred, i.e. the process ends at point c in Figure 3. When the number of TBA^+ ions is high, osmotic swelling takes place. By decreasing the concentration of TBA^+ the swollen structure expands further. Under optimized conditions, the swollen structure falls apart into single

nanosheets. Thus, the exfoliation is regarded as a result of infinite swelling in this concept.[23]

Following this concept a slow ion exchange process between protons and TBA^+ ions is expected because of steric hindrance effects during the first intercalation process. It is noted that the generally accepted concept as outlined in Figure 3 has been based on findings from *ex situ* studies (with varying TBA^+ concentrations), that is, the results were obtained from the final states of exfoliation at different TBA^+ concentrations. And those studies were usually not looking at the kinetics of exfoliation and intercalation processes. An *in situ* study or direct operando observation of the exfoliation process has been missing in this field, despite the fact that it is highly important to understand this process and its kinetics in detail.

1.4 SCOPE AND OUTLINE OF THESIS

The diversity of inorganic nanosheet compositions offers many opportunities for application of nanosheets in various types of technologies. Controllable synthesis of nanosheets is required to move them from the lab to the practical application. In order to control the synthesis process a full understanding the exfoliation mechanism is essential, which requires *in situ* studies of the exfoliation process and more. The research in this thesis is focused on the *in situ* study of the exfoliation mechanism of layered metal oxides into metal oxides nanosheets, and shows strategies to improve the synthesis and lateral size of metal oxides nanosheets. Moreover, efforts have been made to synthesize new layered compounds.

In chapter 2, details of the exfoliation mechanism of layered titanates using TBAOH as exfoliation agent are elucidated by *in situ* experimental techniques. Time resolved small angle X-ray scattering (SAXS) measurements provided insight into the structure evolution of layered titanate by reaction with TBAOH. The results show that the exfoliation driven by acid-base reaction is a rapid process, and the structure evolution turns out to be such that direct exfoliation is followed by restacking, ultimately resulting in a hybrid layered structure. Additional measurements such as time resolved pH and Fourier transform infrared spectroscopy (FTIR) measurements and X-ray photoelectron spectroscopy (XPS) measurements provide informative details about the exfoliation chemistry behind the rapid exfoliation.

Chapter 3 describes the influence of exfoliation conditions on nanosheet formation at the liquid-air interface and inside a solution. The yield of nanosheets at the liquid-air interface was evaluated by determining trends in the lift-up point in the Langmuir Blodgett deposition process. On the other hand, UV-vis spectroscopy was used to determine the yield of nanosheets in solution.

In chapter 4, a method to gain high quality nanosheets is demonstrated. In this research, step exfoliation was established on the basis of a study of exfoliation under concentration deficient exfoliation agent conditions. The process was able to screen defective nanosheets and gain high quality nanosheets for further applications.

The synthesis of calcium niobate (CNO) nanosheets with varying sizes is demonstrated in chapter 5. Using a flux synthesis method, potassium calcium niobate (KCNO, precursor for CNO nanosheets) with different crystal sizes were obtained. Protonation of the yielded KCNO crystals was accomplished, and the exfoliation conditions were optimized to obtain small and large sized CNO nanosheets. A further study in which these nanosheets were used as seed layers for the fabrication of piezoMEMS was carried out to investigate the size dependency of piezoMEMS on nanosheet films.

In chapter 6, some remaining key issues regarding the formation and characterization of metal oxide nanosheet films for further application of nanosheets are addressed. Potential applications of nanosheets in solution processes are described.

REFERENCES

1. Novoselov, K.S., et al., *Electric Field Effect in Atomically Thin Carbon Films.* Science, 2004. **306**(5696): p. 666-669.

2. The Nobel Prize in Physics 2010". Nobelprize.org. Nobel Media AB 2014. Web. 12 Jul 2015. <http://www.nobelprize.org/nobel_prizes/physics/laureates/2010/>

3. Geim, A.K. and K.S. Novoselov, *The rise of graphene.* Nature Materials, 2007. **6**(3): p. 183-191.

4. Mas-Balleste, R., et al., *2D materials: to graphene and beyond.* Nanoscale, 2011. **3**(1): p. 20-30.

5. Rao, C.N.R., H.S.S. Ramakrishna Matte, and U. Maitra, *Graphene Analogues of Inorganic Layered Materials.* Angewandte Chemie International Edition, 2013.

6. Bonaccorso, F., et al., *Graphene, related two-dimensional crystals, and hybrid systems for energy conversion and storage.* Science, 2015. **347**(6217).

7. Zhang, Y., et al., *Mesoscopic organic nanosheets peeled from stacked 2D covalent frameworks.* Chemical Communications, 2011. **47**(26): p. 7365-7367.

8. Chandra, S., et al., *Chemically Stable Multilayered Covalent Organic Nanosheets from Covalent Organic Frameworks via Mechanical Delamination.* Journal of the American Chemical Society, 2013. **135**(47): p. 17853-17861.

9. Lee, C., et al., *Measurement of the elastic properties and intrinsic strength of monolayer graphene.* Science, 2008. **321**(5887): p. 385-388.

10. Ghidiu, M., et al., *Conductive two-dimensional titanium carbide `clay' with high volumetric capacitance.* Nature, 2014. **516**(7529): p. 78-81.

11. Voiry, D., et al., *Conducting MoS2 Nanosheets as Catalysts for Hydrogen Evolution Reaction.* Nano Letters, 2013. **13**(12): p. 6222-6227.

12. Osada, M. and T. Sasaki, *Exfoliated oxide nanosheets: new solution to nanoelectronics.* Journal of Materials Chemistry, 2009. **19**(17): p. 2503-2511.

13. Ma, R. and T. Sasaki, *Two-Dimensional Oxide and Hydroxide Nanosheets: Controllable High-Quality Exfoliation, Molecular Assembly, and Exploration of Functionality.* Accounts of Chemical Research, 2014.

14. Nicolosi, V., et al., *Liquid Exfoliation of Layered Materials.* Science, 2013. **340**(6139).

15. Coleman, J.N., et al., *Two-Dimensional Nanosheets Produced by Liquid Exfoliation of Layered Materials.* Science, 2011. **331**(6017): p. 568-571.

16. Naguib, M., et al., *Two-Dimensional Transition Metal Carbides.* Acs Nano, 2012. **6**(2): p. 1322-1331.

17. Zeng, Z., et al., *An Effective Method for the Fabrication of Few-Layer-Thick Inorganic Nanosheets.* Angewandte Chemie International Edition, 2012. **51**(36): p. 9052-9056.

18. Sasaki, T., et al., *Fabrication of Titanium Dioxide Thin Flakes and Their Porous Aggregate.* Chemistry of Materials, 1997. **9**(2): p. 602-608.

19. Wang, L. and T. Sasaki, *Titanium Oxide Nanosheets: Graphene Analogues with Versatile Functionalities.* Chemical Reviews, 2014. **114**(19): p. 9455-9486.

20. Sasaki, T., et al., *Preparation and Acid-Base Properties of a Protonated Titanate with the Lepidocrocite-like Layer Structure.* Chemistry of Materials, 1995. **7**(5): p. 1001-1007.

21. Sasaki, T., et al., *Macromolecule-like aspects for a colloidal suspension of an exfoliated titanate. Pairwise association of nanosheets and dynamic reassembling process initiated from it.* Journal of the American Chemical Society, 1996. **118**(35): p. 8329-8335.

22. Sasaki, T. and M. Watanabe, *Osmotic Swelling to Exfoliation. Exceptionally High Degrees of Hydration of a Layered Titanate.* Journal of the American Chemical Society, 1998. **120**(19): p. 4682-4689.

23. Geng, F., et al., *Gigantic Swelling of Inorganic Layered Materials: A Bridge to Molecularly Thin Two-Dimensional Nanosheets.* Journal of the American Chemical Society, 2014. **136**(14): p. 5491-5500.

24. Sasaki, T., et al., *A Mixed Alkali Metal Titanate with the Lepidocrocite-like Layered Structure. Preparation, Crystal Structure, Protonic Form, and Acid−Base Intercalation Properties.* Chemistry of Materials, 1998. **10**(12): p. 4123-4128.

Chapter 2

The rapid exfoliation and subsequent restacking of layered titanates driven by Acid-Base reaction

Two-dimensional (2D) (hydro)oxide materials, that is, nanosheets, enable the preparation of advanced 2D materials and devices. The general synthesis route of nanosheets involves exfoliating layered metal (hydro)oxide crystals. This exfoliation process is considered to be time-consuming, hindering their industrial-scale production. Based on *in situ* exfoliation studies on the protonated layered titanate $H_{1.07}Ti_{1.73}O_4 \cdot H_2O$ (HTO), it is now shown that ion intercalation-assisted exfoliation driven by chemical reaction provides a viable and fast route to isolated nanosheets. Contrary to the general expectation, data indicate that direct exfoliation of HTO occurs within seconds after mixing of the reactants, instead of proceeding via a swollen state as previously thought. These findings reveal that ion intercalation-assisted exfoliation driven by chemical reaction is a promising exfoliation route for large-scale synthesis.

*This chapter has been published in *Angewandte Chemie International Edition* **54**, 9239 (2015).

2.1 INTRODUCTION

Inorganic layered materials, such as graphite[1], oxides[2], clays[3], layered metal dichalcogenides[4], layered double hydroxides[5], and MAX phases[6] have been attracting much attention because they can be exfoliated or delaminated into unilamellar sheet units, so-called nanosheets, which exhibit interesting properties due to their two-dimensional (2D) nature. These nanosheets can be used to build advanced materials and devices.[6-7] For example, $Ti_{0.87}O_2$ nanosheets are attractive candidates for ultrathin high-κ dielectric films with low leakage currents.[8] Nanosheets may also be used to control the orientation of crystalline films.[7f, 9] Van der Waals heterostructures, e.g. multilayer hybrid films of alternating graphene and $Ti_{0.91}O_2$ layers show ultrafast electron transfer and have potential applications in photocatalysis, capacitors and sensors.[10] Alternating $Ti_{0.8}Co_{0.2}O_2$-$Ti_{0.6}Fe_{0.4}O_2$ supperlattices show enhanced magneto-optical properties.[11] Developing or discovering an efficient and high yield exfoliation route to exfoliate the layered parent compounds would certainly be a key step towards the application of nanosheets. To achieve exfoliation, several techniques have been employed, such as manual mechanical exfoliation[7b], ultrasonication-assisted solvent exfoliation[12] and ion intercalation-based exfoliation.[13] Among these methods, manual mechanical exfoliation[7b] and ultrasonication-assisted solvent exfoliation[12] are relatively straightforward. However, manual mechanical exfoliation suffers from low yields[13] and ultrasonication-assisted solvent exfoliation is known to result in mechanical damage to the nanosheets[14]. Ion intercalation-based exfoliation is normally driven by chemical reactions and provides a much milder route. The latter exfoliation method serves for the preparation of 2D metal oxides and other ionic layered compounds, encompassing more than 30 compounds till date.[13] Moreover, this route can yield large quantities of dispersed nanosheets and is potentially the most promising for large-scale production processes among the mentioned exfoliation methods. For example, the chemical exfoliation and intercalation of lepidocrocite-type $Ti_{0.87}O_2$ titanates in water has been reported as an efficient way to prepare two dimensional titania nanosheets and new titania-based hybrid materials with large lateral sizes.[15] However, it is generally thought that the structural evolution of layered oxides upon ion intercalation passes via a swollen state into the exfoliated state.[16] This type of exfoliation via ion intercalation is considered to be time

consuming due to slow diffusion processes and takes typically 1-2 weeks according to several reports.[16a, 17] This slow process is one of the main concerns hampering further development.[13]

Here, based on *in situ* studies on exfoliation of the lepidocrocite-type titanate $H_{1.07}Ti_{1.73}O_4 \cdot H_2O$ (HTO), one of the best known study model for layered metal oxides, we show that ion intercalation exfoliation driven by an acid-base reaction is in fact a very rapid and time-efficient process. Contrary to previous conclusions from *ex situ* studies[16], our *in situ* experimental data demonstrate that exfoliation occurs directly after mixing of reactants. Isolated nanosheets form that may restack into a hybrid layered structure as illustrated in Figure 1.

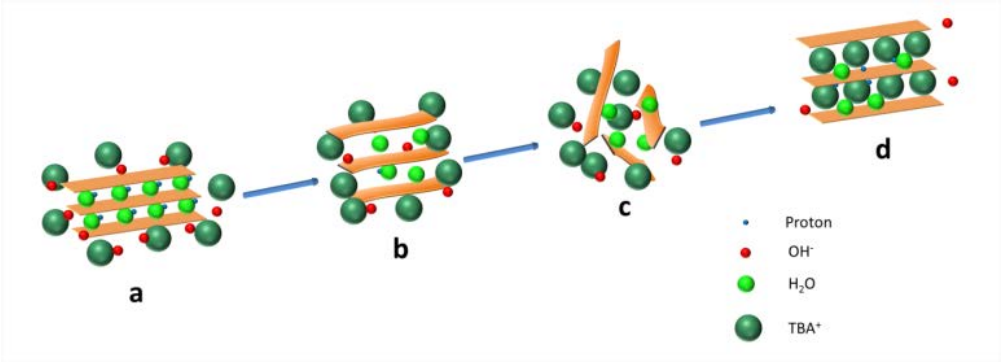

Figure 1. Schematic diagram of the proposed intercalation mechanism. (a) The acid-base reaction starts with diffusion of OH^- ions from tetra-butyl ammonium hydroxide (TBAOH) into HTO, followed by their reaction with protons; (b) The layered structure of HTO loses its stability because of the acid (HTO) – base (OH^-) reaction; (c) Isolated nanosheets; (d) Nanosheets restack into a final hybrid state.

2.2 RESULTS AND DISCUSSION

By using the Langmuir-Blodgett technique, a single layer nanosheet film on a silicon substrate was obtained from an aqueous HTO+TBAOH solution after a reaction time of only 30 s (Figure 2a). See Sections S1 and S2 in the Appendices for experimental details. Clearly a substantial concentration of single nanosheets was already present in the solution after this short period of time. The UV-vis spectra showed that this solution had the same characteristics as an exfoliated nanosheet solution after a reaction time of two weeks (Figure 2b),[15a] even though the TBAOH/HTO ratio of the former solution was so high that it is typically thought yield a swollen hybrid

state rather than isolated nanosheets.[16a] To elucidate the details of this unexpected rapid exfoliation process, we applied time-resolved *in situ* Small Angle X-ray Scattering (SAXS) to reveal the dynamics of exfoliation and monitor the structure evolution. SAXS data of the first 27 s of reaction are shown in Figure 2c. The quickly evolving SAXS curves of reacting TBAOH/HTO dispersions indicate fast structure evolution.

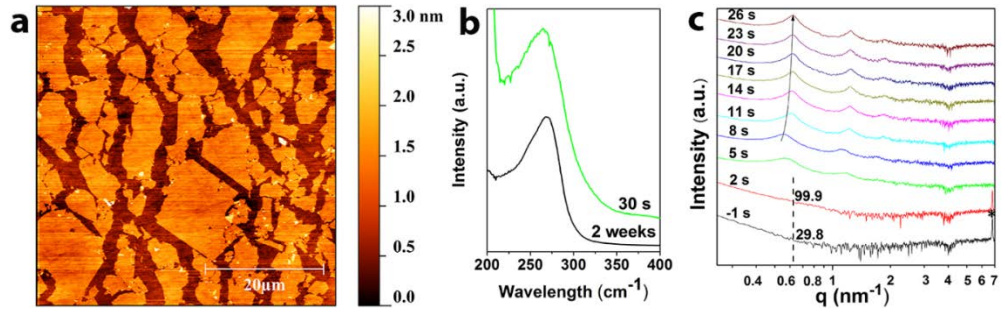

Figure 2. (a) AFM image obtained from a Langmuir-Blodgett film obtained from a HTO+TBAOH solution after 30 s reaction time. (b) UV-vis spectra of titanate solutions after 30 s (TBAOH/HTO= 4/1) and after 2 weeks (TBAOH/HTO= 1/1) of reaction time. (c) Time-resolved SAXS curves of HTO solution after mixing with TBAOH. The drawn line illustrates the trend of the first correlation maximum in the newly evolving structure.

The time of injection was 8 s and started at $t = 0$. Scattering curves before adding TBAOH ($t < 0$) showed a sharp peak at $q = 6.792$ nm^{-1}, indicating the presence of layered HTO with an interlayer spacing of $d = 2\pi/q = 0.92$ nm.[18] At $t = 2$ s (Figure 2c), the same peak was still present. No other peaks were observed, but the background scattering intensity had increased sharply over the entire q range. For example, the scattering intensity at $q = 0.622$ nm^{-1} increased from 29.8 (arb. units) at $t = -1$ s to 99.9 (arb. units) at $t = 2$ s. In a reference experiment without HTO we verified that the intensity change originated from the reaction (Appendices Figure S1). At $t = 2$ s, the net TBAOH/HTO ratio in the solution was 1, a condition where isolated nanosheets are known to form.[17a, 19] The high background scattering intensity suggests a contribution from entities that do not have a pronounced SAXS signature, i.e. isolated nanosheets. At $t = 5$ s a new correlation peak was clearly visible at $q = 0.576$ nm^{-1}, and the peak at $q = 6.792$ nm^{-1} had disappeared completely. This indicates that a new layered structure with clear Bragg-like correlation peaks had just formed, while the original layered structure of HTO had disappeared. The

emerging correlation peaks suggest a restacking process of nanosheets into a new layered structure with larger spacings. 'Swollen' hybrid structures have indeed been reported for systems with a TBAOH/HTO ratio of 4, although they were thought to form via another pathway, i.e. intercalation of TBA^+, and only after much longer periods of time[17b].

The experimental SAXS data were fitted to the modified Fluctuating Gap Model (FGM) developed by Connolly *et al.*[20] for layered systems such as clays and oxides, and modified by Besselink *et al.*[17b]. See section S3 in the Appendices for further details. Figure 3a shows the stack number *m* and the interlayer spacing *d* derived from best fits of the modified FGM to the emerging correlation peak of the newly forming phase. The stack number *m* describes the average number of layers in a stack of sheets in the colloidal state. Its value increased slowly with time, implying that the new structure grew, most likely by restacking of isolated nanosheets. The interlayer spacing *d* between these nanosheet platelets in a stack decreased with time, until they reached a more or less constant distance of 10.1 nm after 20 s. The final values are similar to separation distances reported elsewhere for similar HTO+TBAOH mixtures[17b]. The gradually decreasing interlayer spacing, evidenced by the first correlation peak (Figure 2c) as shown in Figure 3a, supports the conclusion that restacking occurs following a very fast exfoliation process. It is noted that *in situ* SAXS data of a similar system with a TBAOH/HTO ratio of 6 : 1 showed the same trend as presented in Figure 2c for TBAOH/HTO = 4 : 1 (Appendices Figure S2a). Direct intercalation of TBA^+ into an existing stack to yield a 'swollen' state[2] would lead to an increasing interlayer spacing with time (correlation maximum at decreasing *q*), rather than a decreasing spacing with time (correlation maximum at increasing *q*) as the experimental data in Figure 3a show. We ruled out the possibility of TBA^+ intercalation prior to exfoliation by conducting SAXS experiments with a reference solution with a low TBAOH/HTO ratio of 1 : 1 (Figure S2b). At this ratio only exfoliation has been reported,[17a, 19] and our data showed that intercalation/swelling did not occur. Hence, the data presented above show clearly that exfoliation of HTO occurs upon reaction with TBAOH, yielding isolated nanosheets which then (partially) restack into a new layered hybrid material when the TBAOH/HTO ratio is 4 : 1. The conclusion is consistent with the results from kinetic modeling as discussed below.

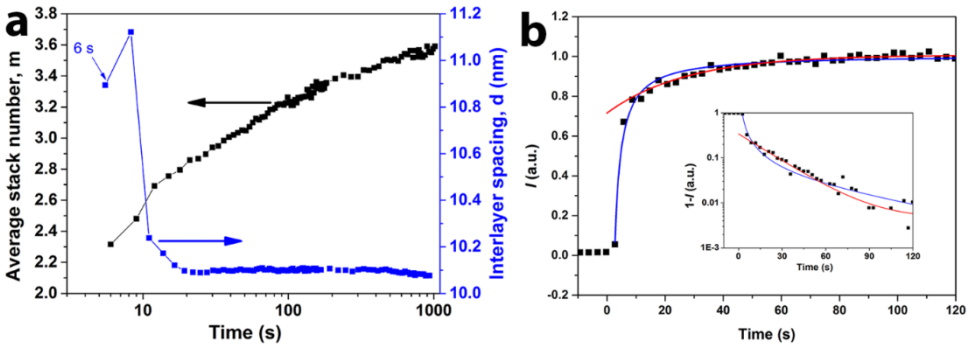

Figure 3. (a) Average stack number *m* and interlayer spacing *d* between layers in hybrid stack derived from the modified FGM by fitting to time resolved SAXS profiles of HTO upon reaction with TBAOH. (b) The curve depicts the scattering intensity at $q = 0.622$ nm^{-1} (at $t < 5$ s) or at the first peak position (peak height) (at $t > 5$ s). The inset shows the normalized intensity data on a logarithmic scale.

We developed a general kinetic model for the sequence of exfoliation and restacking reactions (see Section S4 in Appendices) and used the time-resolved peak intensity of the first correlation maximum to extract kinetic data. In the proposed sequence of reactions, one of two steps will be rate-limiting unless their rates are roughly the same. By fitting the kinetic data in Figure 3b with the kinetic expressions for each of the two limiting cases, we found that the rate of restacking followed second order kinetics at $t < 15$ s, while at $t > 15$ s the restacking rate followed first order kinetics (Figure 3b). These results indicate that the restacking process is rate-limiting in the early stages of reaction (i.e. fast exfoliation rate due to high concentration of HTO, but slow restacking rate due to low concentration of isolated nanosheets), while the exfoliation process becomes rate-determining in the later stages (i.e. slow exfoliation rate due to depletion of HTO and fast restacking rate due to high concentration of 2D nanosheets). This result is in good agreement with the conclusion drawn above that exfoliation of HTO precedes restacking of nanosheets into a new layered hybrid material.

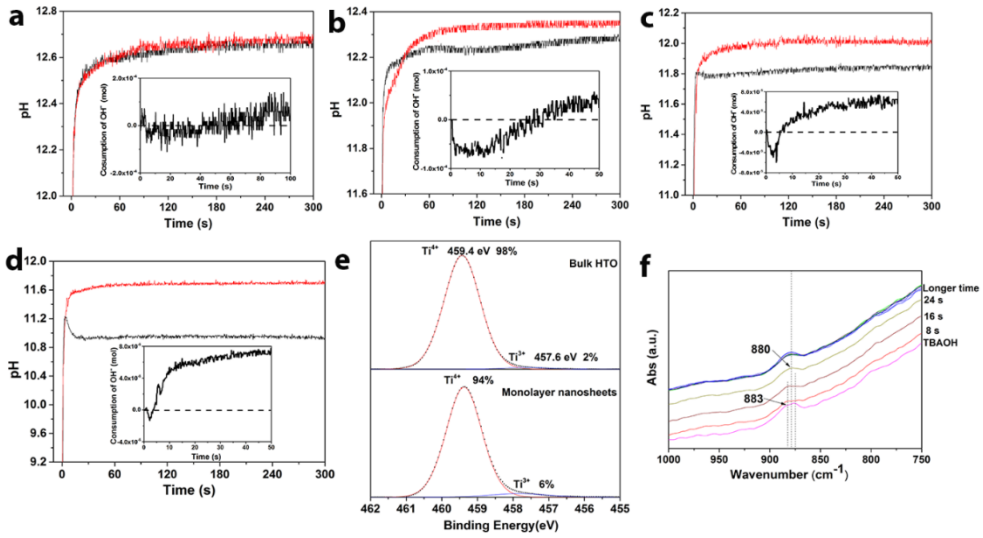

Figure 4. pH change during reaction at varying TBAOH/HTO ratios: (a) 2 : 1, (b) 1 : 1, (c) 1 : 2 and (d) 1 : 4. The black line represents the pH in a HTO-TBAOH solution; the red line represents the reference curve obtained from a water-TBAOH solution. The inset shows the net consumption/release of OH^- in a reacting solution calculated from the difference between the two curves. (e) High resolution XPS spectra of bulk HTO and monolayer $Ti_{0.87}O_2$ nanosheets for Ti $2p_{3/2}$. (f) Time resolved FTIR data at a TBAOH/HTO molar ratio of 4 : 1.

An acid-base reaction between OH^- from TBAOH and protons from HTO was required to initiate the exfoliation of HTO (Figure S3). Figure 4a-d shows an unexpected temporary rise of pH, especially for low TBAOH/HTO ratios, when TBAOH was added to HTO (black curve). A smaller pH rise was seen when TBAOH was added to a solution in absence of HTO (red curve). The temporary pH rise upon reaction indicates that initially, a net amount of OH^- was formed, probably resulting from the exfoliation process. To investigate the exfoliation chemistry in more detail, XPS and *in situ* FTIR measurements were carried out. High resolution XPS measurements were done on HTO powders and exfoliated monolayer nanosheets. The Ti $2p_{3/2}$ XPS spectra shown in Figure 4e show peaks at 459.4 eV and 457.6 eV, which can be assigned to Ti^{4+} and Ti^{3+}, respectively.[21] The concentration of Ti^{3+} in monolayer nanosheets was higher than in HTO powders. It increased from 2 at% before to 6 at% after exfoliation, indicating that partial electron gain (reduction) of Ti atoms occurred upon exfoliation of HTO.[22] The same phenomenon has also been reported by Sun *et al*, and they recently showed that the valence state of metal

elements in 2D metal oxide nanosheets is lower than in the corresponding bulk materials.[21] The *in situ* FTIR data in Figure 4f (full range FTIR data shown in Figure S4a) show that a new peak appeared at 880 cm^{-1} in the investigated spectral range after reaction times of 16-24 s and longer. The peak at 880 cm^{-1} can be assigned to fully covered hydroxyl groups in lepidocrocite-type titanates.[23] The presence of hydroxyl groups was verified by O 1*s* XPS spectra of monolayer $Ti_{0.87}O_2$ nanosheets (Figure S4b). The data suggest that a large number of protons adsorbed onto nanosheets to form hydroxyl groups after the acid-base and exfoliation reactions. This is consistent with the high pH of all solutions irrespective of TBAOH/HTO ratio after 30 min of reaction time (Table S1), and it indicates that HTO crystals did not release large numbers of protons. Hence, the reduction of Ti leads to adsorption of more (positive) ions to compensate for the loss of positive charge in the sheet. The resulting uptake of protons from solution will then lead to an increase of pH in the reaction solution to temporarily higher values than in the corresponding reference solution, as shown in Figure 4a-d. We propose that the massive uptake of protons is required for exfoliation and nanosheet surface charge compensation (see Section S5 in Appendices). Combination of partial electron gain (reduction) of Ti ions and massive uptake of protons from the aqueous solution by the exfoliating HTO crystals leads to *in situ* OH^- formation, serving as reactant for further acid-base reaction. Because of relative long diffusion path for reactants in the layered structure, the *in situ* generation of OH^- may accelerate the exfoliation process substantially.

2.3 CONCLUSIONS

In summary, we found that the exfoliation of layered titanate driven by acid-base reaction is much faster than was generally believed. Exfoliation occurred directly instead of proceeding via an intermediate swollen state. We observed the reduction of transition metal titanium atoms and *in situ* OH^- generation in layered titanate upon exfoliation. Rapid exfoliation was also observed by us in other layered oxides, i.e. protonated calcium niobate ($HCa_2Nb_3O_{10}•H_2O$) and protonated titanoniobate ($HTi_2NbO_7•H_2O$, $H_3Ti_5NbO_{14}•H_2O$) not shown here. Our results highlight the exfoliation process driven by chemical reaction as a promising route for rapid and efficient large scale synthesis of 2D materials. Our findings also indicate that a short period of exfoliation is needed to synthesize isolated nanosheets, as they would reorganize into a hybrid stack of sheets after a given period of time when the

TBA/HTO ratio > 2.[2] We expect that the technique may find more widespread use to exfoliate layered metal oxides and other ionic layered compounds, and may even serve as guidance for exfoliation strategies for non-ionic layered compounds, in order to achieve rapid and efficient exfoliation via alternative ways such as chemical modification.

REFERENCES

1. M. Cai, D. Thorpe, D. H. Adamson, H. C. Schniepp, *J. Mater. Chem.* **2012**, *22*, 24992-25002.

2. L. Wang, T. Sasaki, *Chem. Rev.* **2014**, *114*, 9455-9486.

3. aD. Kong, C. E. Park, *Chem. Mat.* **2002**, *15*, 419-424; bT. Lan, T. J. Pinnavaia, *Chem. Mat.* **1994**, *6*, 2216-2219.

4. M. Chhowalla, H. S. Shin, G. Eda, L.-J. Li, K. P. Loh, H. Zhang, *Nature Chemistry* **2013**, *5*, 263-275.

5. Q. Wang, D. O'Hare, *Chem. Rev.* **2012**, *112*, 4124-4155.

6. M. Naguib, V. N. Mochalin, M. W. Barsoum, Y. Gogotsi, *Adv. Mater.* **2014**, *26*, 992-1005.

7. aA. K. Geim, K. S. Novoselov, *Nat. Mater.* **2007**, *6*, 183-191; bK. S. Novoselov, A. K. Geim, S. V. Morozov, D. Jiang, Y. Zhang, S. V. Dubonos, I. V. Grigorieva, A. A. Firsov, *Science* **2004**, *306*, 666-669; cT. Shibata, T. Ohnishi, I. Sakaguchi, M. Osada, K. Takada, T. Kogure, T. Sasaki, *J. Phys. Chem. C* **2009**, *113*, 19096-19101; dA. K. Geim, I. V. Grigorieva, *Nature* **2013**, *499*, 419-425; eS. Stankovich, D. A. Dikin, G. H. B. Dommett, K. M. Kohlhaas, E. J. Zimney, E. A. Stach, R. D. Piner, S. T. Nguyen, R. S. Ruoff, *Nature* **2006**, *442*, 282-286; fM. Nijland, S. Kumar, R. Lubbers, D. H. A. Blank, G. Rijnders, G. Koster, J. E. ten Elshof, *ACS Appl. Mater. Interfaces* **2014**, *6*, 2777-2785; gI. Y. Kim, Y. K. Jo, J. M. Lee, L. Wang, S.-J. Hwang, *The Journal of Physical Chemistry Letters* **2014**, *5*,

4149-4161; hF. Bonaccorso, L. Colombo, G. Yu, M. Stoller, V. Tozzini, A. C. Ferrari, R. S. Ruoff, V. Pellegrini, *Science* **2015**, *347*, 1246501.

8. M. Osada, Y. Ebina, H. Funakubo, S. Yokoyama, T. Kiguchi, K. Takada, T. Sasaki, *Adv. Mater.* **2006**, *18*, 1023-1027.

9. T. Shibata, K. Fukuda, Y. Ebina, T. Kogure, T. Sasaki, *Adv. Mater.* **2008**, *20*, 231-235.

10. K. K. Manga, Y. Zhou, Y. Yan, K. P. Loh, *Adv. Funct. Mater.* **2009**, *19*, 3638-3643.

11. M. Osada, Y. Ebina, K. Takada, T. Sasaki, *Adv. Mater.* **2006**, *18*, 295-299.

12. J. N. Coleman, M. Lotya, A. O'Neill, S. D. Bergin, P. J. King, U. Khan, K. Young, A. Gaucher, S. De, R. J. Smith, I. V. Shvets, S. K. Arora, G. Stanton, H.-Y. Kim, K. Lee, G. T. Kim, G. S. Duesberg, T. Hallam, J. J. Boland, J. J. Wang, J. F. Donegan, J. C. Grunlan, G. Moriarty, A. Shmeliov, R. J. Nicholls, J. M. Perkins, E. M. Grieveson, K. Theuwissen, D. W. McComb, P. D. Nellist, V. Nicolosi, *Science* **2011**, *331*, 568-571.

13. V. Nicolosi, M. Chhowalla, M. G. Kanatzidis, M. S. Strano, J. N. Coleman, *Science* **2013**, *340*, 1226419.

14. R. Mas-Balleste, C. Gomez-Navarro, J. Gomez-Herrero, F. Zamora, *Nanoscale* **2011**, *3*, 20-30.

15. aT. Sasaki, M. Watanabe, *The Journal of Physical Chemistry B* **1997**, *101*, 10159-10161; bT. Sasaki, Y. Ebina, Y. Kitami, M. Watanabe, T. Oikawa, *The Journal of Physical Chemistry B* **2001**, *105*, 6116-6121; cT. Sasaki, *J. Ceram. Soc. Jpn.* **2007**, *115*, 9-16; dM. Onoda, Z. P. Liu, Y. Ebina, K. Takada, T. Sasaki, *J. Phys. Chem. C* **2011**, *115*, 8555-8566; eT. Sasaki, F. Izumi, M. Watanabe, *Chem. Mat.* **1996**, *8*, 777-782; fT. Tanaka, K. Fukuda, Y. Ebina, K. Takada, T. Sasaki, *Adv. Mater.* **2004**, *16*, 872-875.

16. aT. Sasaki, M. Watanabe, *J. Am. Chem. Soc.* **1998**, *120*, 4682-4689; bF. Geng, R. Ma, Y. Ebina, Y. Yamauchi, N. Miyamoto, T. Sasaki, *J. Am. Chem. Soc.* **2014**, *136*, 5491-5500.

17. aT. Tanaka, Y. Ebina, K. Takada, K. Kurashima, T. Sasaki, *Chem. Mat.* **2003**, *15*, 3564-3568; bR. Besselink, T. M. Stawski, H. L. Castricum, D. H. A. Blank, J. E. ten Elshof, *J. Phys. Chem. C* **2010**, *114*, 21281-21286.

18. T. Sasaki, F. Kooli, M. Iida, Y. Michiue, S. Takenouchi, Y. Yajima, F. Izumi, B. C. Chakoumakos, M. Watanabe, *Chem. Mat.* **1998**, *10*, 4123-4128.

19. H. Yuan, R. Lubbers, R. Besselink, M. Nijland, J. E. ten Elshof, *ACS Appl. Mater. Interfaces* **2014**, *6*, 8567-8574.

20. J. Connolly, J. S. van Duijneveldt, S. Klein, C. Pizzey, R. M. Richardson, *Langmuir* **2006**, *22*, 6531-6538.

21. Z. Sun, T. Liao, Y. Dou, S. M. Hwang, M.-S. Park, L. Jiang, J. H. Kim, S. X. Dou, *Nat Commun* **2014**, *5*, 3813.

22. S. Wendt, P. T. Sprunger, E. Lira, G. K. H. Madsen, Z. Li, J. Ø. Hansen, J. Matthiesen, A. Blekinge-Rasmussen, E. Lægsgaard, B. Hammer, F. Besenbacher, *Science* **2008**, *320*, 1755-1759.

23. H. Yuan, R. Besselink, Z. Liao, J. E. ten Elshof, *Sci. Rep.* **2014**, *4*, 4584.

APPENDICES

S1. Materials and methods: Materials synthesis

The $K_{0.8}Ti_{1.73}Li_{0.27}O_4$ (KLTO) precursor was obtained with a flux method developed by Tanaka et al.[1] Titanium(IV) dioxide TiO_2 (Riedel-de Haen), anhydrous potassium carbonate K_2CO_3 (Fluka), lithium carbonate Li_2CO_3 (Riedel-de Haen), and molybdenum(VI) oxide MoO_3 (Sigma-Aldrich) (1.73 : 1.67 : 0.13 : 1.27 molar ratio) were heated to 1150°C, held at that temperature for 30 min, and then slowly cooled down to 950 °C at a speed of 4 °C/h. The oven was then allowed to cool further to room temperature by natural cooling. The resulting KLTO powder was washed 3 times in 250 mL water to remove K_2MoO_4. Then KLTO powder was dispersed in a 2 mol/L HNO_3 solution (250 mL) at room temperature while stirring. The acidic solution was replaced daily by a fresh one via decantation. After treatment for 3 days, the acid-exchanged crystals were collected by filtration and washed with a copious quantity of pure water, then air dried to get $H_{1.07}Ti_{1.73}O_4 \cdot H_2O$ (HTO) powder. Tetra *n*-butylammonium hydroxide TBAOH (40 wt% H_2O, Alfa Aesar) were used as received to exfoliate HTO crystals. Demineralized water was used throughout the experiments.

S2. Materials and methods: Methods

S2.1 LB deposition and analysis

Langmuir-Blodgett (LB) deposition using nanosheet dispersions was carried out after varying reaction times (0.5 min, 1 min, 2 min, 5 min, 10 min, 20 min, 30 min, 1 h, 2 h, 3 h) at a molar ratio TBAOH : HTO = 4 : 1. In LB deposition, 2 ml of stock suspension with nominal concentration 5 g/l was diluted to a total volume of 500 ml by addition of water. The diluted solution was kept standing for 5 min, then 50 ml was separated from the middle/top part of the nanosheet suspension using a syringe. After 2 min the separated suspension was poured into a Langmuir Blodgett trough (KSV Minimicro, a Teflon trough with an active trough surface area of 100 cm^2, L195 x W51 x D4 mm3 and a dipping well L10 x W28 x D28 mm^3, trough volume 48 cm^3) and left for 5 min to equilibrate and stabilize the surface pressure before the deposition process started. Generally, a film was deposited at the highest surface pressure that we were able to reach. The trough was cleaned prior to every experiment with ethanol and a soft brush, rinsed several times with distilled water to remove ethanol and then blown dry with nitrogen. The silicon substrate was first cleaned with a CO_2 snow jet to remove dust particles and adsorbates. Then it was

cleaned in a Harrick Plasma PDC-002 oxygen plasma cleaner (25 W) for 5 min to oxidize any organic residues on the substrate surface. Subsequently, the silicon substrate was immersed vertically into the suspension. The surface pressure was measured using a Wilhelmy plate attached to the KSV Minimicro frame.

Tapping mode Atomic Force Microscopy (AFM; Veeco Dimension Icon) was used to determine the morphology of the final LB films. The AFM data were further analyzed using the Gwyddion (version 2.31) software package.

S2.2 In situ SAXS measurements

The SAXS experiments were carried out using synchrotron radiation on the Dutch-Belgian beam line, DUBBLE BM-26B of the European Synchrotron Radiation Facility (ESRF) in Grenoble.[2] The X-ray beam energy was 12 keV. The Pilatus 1M detector was placed at a distance of 1.3 m from the sample to acquire data in the range $0.15 < q < 8.00$ nm^{-1}. SAXS patterns were recorded every 3 s, of which the SAXS software needed 1.5 s to save the recorded data of each curve, so the recording time for each pattern was 1.5 s. The mixing setup consisted of a SAXS measurement chamber, a mixing chamber, a timing injection system and a pump system. During measurements, the solution was cycled between the SAXS measurement chamber and the mixing chamber. Meanwhile, the solution in the mixing chamber was stirred. In a typical measurement, 5 ml TBAOH solution corresponding with a molar ratio of TBAOH/HTO of 4 : 1 or 1 : 1 was injected into the mixing chamber which already contained 15 ml water and 0.1 g HTO. The total injection time was 8 s.

S2.3 In situ pH measurements

The pH measurements were performed using an USB DrDAQ recorder with a pH electrode. The data were recorded every 0.1 s. In a typical measurement, 15 ml water and 0.1 g HTO were placed in a reaction bottle, and then the solution was stirred. During the pH measurements, 5 ml TBAOH solution of varying concentration was manually injected into the reaction bottle while monitoring the pH simultaneously. The injection time was controlled to be less than 3 s, and the pH meter can respond within 3 s to the pH change.

S2.4 In situ FTIR measurements

Attenuated Total Reflection Fourier transform infrared spectroscopy (FTIR; Bruker TENSOR27 with a Pike GladiATR) was used to monitor the bond changes during reaction. 0.01 g HTO powder was first put into the sample compartment for liquid measurements and then the *in situ* FTIR measurements started with a recording speed of 8 s per scan. 0.169 ml as-received TBAOH solution was manually added to the sample compartment during measurement. The injection time was controlled to be less than 2 s.

S2.5 XPS and UV-vis measurements

X-ray photoelectron spectroscopy (XPS) was used to investigate the atomic concentrations before exfoliation on HTO, and after exfoliation on monolayer nanosheets obtained by LB deposition. The XPS measurements were conducted on an Omicron nanotechnology GmbH (Oxford Instruments) Surface Analysis system with a photon energy of 1486.7 eV (Al Kα X-ray source). The pass energy was set to 20 eV. The peak position of Ti $2p_{3/2}$ in the spectrum of monolayer nanosheets sample was corrected using the binding energy of Ti $2p_{3/2}$ in the bulk HTO sample as a reference. A standard Shirley background is used for all the spectra analysis. UV-Vis spectra for samples were recorded with a Cary 50 UV-Vis spectrophotometer in transmission mode. A solution of 20 ml containing 0.1 g HTO was mixed with TBAOH in a TBA^+/H^+ molar ratio of 4 : 1 for 30 s. Then the suspension was diluted prior to the measurement. The exfoliated nanosheets sample for the UV-Vis measurement was obtained from a solution of 20 ml containing 0.1 g HTO was mixed with TBAOH in a TBA^+/H^+ molar ratio of 1 : 1 for 2 weeks.

S3. Modified Fluctuating Gap Model

The scattering intensity for a diluted mixture of sheets and stacked sheets can be described by [3]:

$$I(q) = A \cdot \left(\frac{\sin^2\left(\frac{q \cdot h}{2}\right)}{q^2 \cdot \left(\frac{q \cdot h}{2}\right)^2} \right) \cdot \left(\frac{\sum_{n=1}^{\max} X(n) \cdot \sin^2\left(\frac{q \cdot n \cdot d}{2}\right)}{\sin^2\left(\frac{q \cdot d}{2}\right)} \right) \quad (1)$$

where h is the thickness of a single sheet (in nm), d represents the center-to-center separation distance between two adjacent sheets in a stack of sheets, n is a particular number of sheets being stacked, ranging from $n = 1$ to $n = \max$, $X(n)$ is a distribution function of a stack with n sheets, and A is a scaling constant. The latter constant A is proportional to the overall number of electron density fluctuations (Δn_e) and depends on the particle number density (N) and the contrast in electron density between particles and their surroundings ($\Delta\rho$).

Connolly et al. applied a distribution function for similar clay-like suspensions:[3a]

$$X(n) = n(X_1 \exp(\alpha))^n \exp(-\alpha) \qquad (2)$$

where X_1 is the concentration of single layered sheets and α is a constant that is related to the adhesive forces between sheets. Substitution of equation (2) into (1) gives:

$$I(q) = A \exp(-\alpha) \left(\frac{\sin^2\left(\frac{qh}{2}\right)}{q^2\left(\frac{qh}{2}\right)^2} \right) \left(\frac{\sum_{n=1}^{\max} n(X_1 \exp(\alpha))^n \sin^2\left(\frac{qnd}{2}\right)}{\sin^2\left(\frac{qd}{2}\right)} \right) \qquad (3)$$

Note that this equation contains a singularity, i.e. several combinations of A, α and X_1 exist that result in exactly the same intensity curves. Such a singularity complicates the optimization process. Connolly and co-workers resolved the problem by setting the overall concentration C of platelets as a constant. Consequently, X_1 was not considered as a fit parameter and was calculated from C and α. Nevertheless, in the current work a variety of different systems has been examined, and the efficiency of exfoliation and overall concentration of dispersed platelets is not exactly known. We therefore used a different approach to reduce the number of optimization parameters, namely by the introduction of two new parameters (B and β) defined by:

$$B = A \cdot \exp(-\alpha) \qquad (4)$$

$$\beta = \alpha + \ln(X_1) \qquad (5)$$

where B is a new scaling parameter and β is a similar parameter as α. It can be associated with the adhesive strength between particles. By this approach the three

parameters X_1, A and α were reduced to two parameters, the singularity was removed and the resulting intensity function can be described by

$$I(q) = B \cdot \left(\frac{\sin^2\left(\frac{q \cdot h}{2}\right)}{q^2 \cdot \left(\frac{q \cdot h}{2}\right)^2} \right) \cdot \left(\frac{\sum_{n=1}^{\max} n \cdot (\exp(\beta))^n \cdot \sin^2\left(\frac{q \cdot n \cdot d}{2}\right)}{\sin^2\left(\frac{q \cdot d}{2}\right)} \right) \qquad (6)$$

To speed up the calculation process, it was convenient to solve the Riemann's sum analytically. For $\beta < 0$ the Riemann's sum converges and its solution is given by

$$\sum_{n=1}^{\infty} n \cdot (\exp(\beta))^n \cdot \sin^2\left(\frac{q \cdot n \cdot d}{2}\right) = \frac{\exp(\beta)}{2 \cdot (\exp(\beta)-1)^2} - \frac{\exp(\beta + i \cdot d \cdot q)}{4 \cdot (\exp(\beta + i \cdot d \cdot q)-1)^2} - \frac{\exp(\beta - i \cdot d \cdot q)}{4 \cdot (\exp(\beta - i \cdot d \cdot q)-1)^2} \qquad (7)$$

where i is the imaginary number. Equation (7) was rearranged into a combination of exponential cosine and hyperbolic cosine functions by applying Euler's equations, which resulted in

$$\sum_{n=1}^{\infty} n \cdot (\exp(\beta))^n \cdot \sin^2\left(\frac{q \cdot n \cdot d}{2}\right) = \left(\frac{1}{2} - \frac{(\exp(\beta)-1)^2 \cdot (\cosh(\beta) \cdot \cos(d \cdot q) - 1)}{2 \cdot \exp(\beta) \cdot \left(2 \cdot (\cosh(\beta))^2 - 4 \cos(d \cdot q) \cdot \cosh(\beta) + \cos(2 \cdot d \cdot q) + 1\right)} \right) \qquad (8)$$

From β, the average number of sheets that contributes to a single stack of sheets, i.e. the average stack number m, can be calculated by

$$m = \frac{\sum_{n=2}^{\infty} n \cdot X(n)}{\sum_{n=2}^{\infty} X(n)} = \frac{1 - 2 \cdot \exp(-\beta)}{1 - \exp(-\beta)} \qquad (9)$$

Please note that single nanosheets are not included in the average stack number m. The value of β can be derived from m via

$$\beta = \ln\left(\frac{m-2}{m-1}\right) \qquad (10)$$

Nevertheless, several experimental SAXS curves indicated that even with relatively narrow pseudo-Bragg-peaks, a relatively large background signal (with $I \sim q^{-2}$) was present that was attributed to a unilamellar nanosheet fraction. In other words, even with a relatively large m, X_1 remained large as well. Consequently, better fitting

results were obtained when X_1 was considered as a separate variable that deviated from the distribution function Equation (2). The intensity function equation (6) was therefore rearranged to

$$I(q) = B\left(\frac{\sin^2\left(\frac{qh}{2}\right)}{q^2\left(\frac{qh}{2}\right)^2}\right)\left(\frac{X_{ss}m}{X_{ss}m+(1-X_{ss})} + \left(\frac{1-X_{ss}}{X_{ss}m+(1-X_{ss})}\right)S_m(q)\right) \quad (11)$$

where X_{ss} is the mass-weighted single sheet fraction by the introduction of the weighting factor m, and $S_m(q)$ is the structure function for multilayered nanosheets:

$$S_m(q) = \frac{\left(\frac{1}{2}\frac{(\exp(\beta)-1)^2(\cosh(\beta)\cos(qd)-1)}{2\exp(\beta)(2(\cosh(\beta))^2-4\cos(qd)\cosh(\beta)+\cos(2qd)+1)}\right)}{sin^2\left(\frac{qd}{2}\right)} - \exp(\beta) \quad (12)$$

Please note that the term –exp(β) was introduced to subtract the contribution of single nanosheets in the structure function of multilayered sheets.

Fits of experimental data to the modified FGM yielded the parameters fraction of isolated sheets in solution *x*, spacing between plates/sheets *d*, average number of planes in a stack *m*, and thickness of one plate/nanosheet *h*. In the fitting process, we left all parameters free to optimize, except for *h*, which was kept constant at *h* = 0.75 nm.[5] The fitting data for the fraction of nanosheets *x* increased with time from 12.4% to 42.3%. The fitting data for the stacking number *m* and the interlayer spacing *d* are shown in the main text. A typical best fit of the experimental SAXS data at *t* = 120 s (green curve) to the modified Fluctuating Gap Model (FGM) (black curve) is shown below.

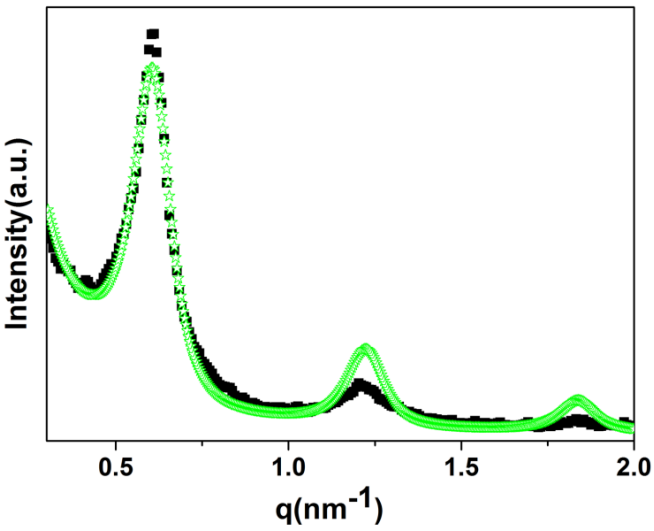

Figure A1. Typical best fit of the experimental SAXS data at t = 120 s (black curve) to the modified Fluctuating Gap Model (FGM) (green curve).

The optimized values from the fit were m = 3.26, d = 10.10 nm, and x = 32.2%. The faster intensity decay of the experimental curve is caused by an inhomogeneity in the nanosheet thickness for short periods of exfoliation as illustrated below.

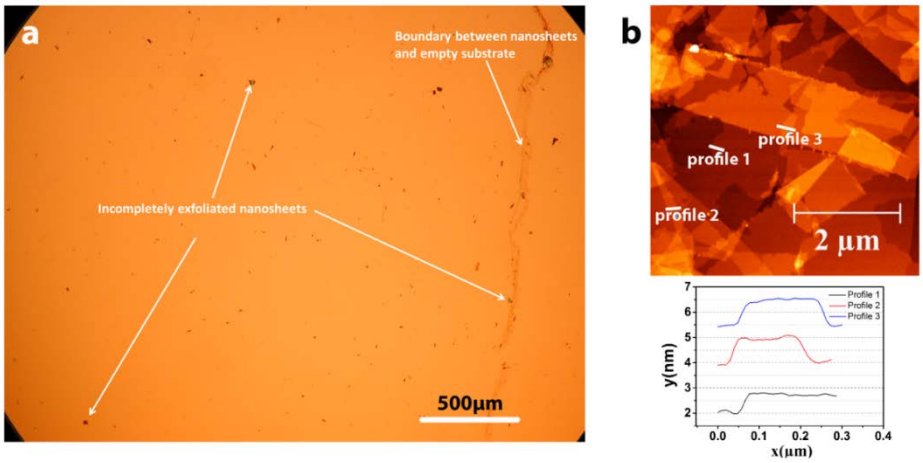

Figure A2. (a) Microscope image of LB film obtained from HTO suspensions after reaction with TBAOH for 30 s (TBAOH/HTO molar ratio = 4 : 1, c_{HTO}=5 g/l). (b) AFM image of selected area where incompletely exfoliated nanosheets obtained from HTO suspensions after reaction with TBAOH for 10 min (TBAOH/HTO molar ratio = 4 : 1, c_{HTO}=5 g/l) were present. The height profiles were recorded on the film shown in the AFM image.

Figure A2(a) shows a microscope image of an LB film obtained from HTO suspensions after reaction with TBAOH for 30 s (TBAOH/HTO molar ratio = 4 : 1, c_{HTO} = 5 g/l). The exfoliation of HTO upon reaction with TBAOH was fast enough to form a monolayer nanosheet film within 30 s as shown in Figure 2a of the main text. However, we also found some incompletely exfoliated nanosheets. Figure A2(b) shows an AFM image of a selected area where incompletely exfoliated nanosheets obtained from HTO suspensions after reaction with TBAOH for 10 min (TBAOH/HTO molar ratio = 4 : 1, c_{HTO}=5 g/l) present. The corresponding height profiles recorded on these films are also shown. The height profiles have an offset with respect to each other. Two different thicknesses of nanosheets (0.7 nm and 1.1 nm) were found in the LB film made after 10 min of reaction. The thickness of 0.7 nm (e.g. profile 1) is close to the individual layer thickness of non-exfoliated HTO.[5] These non-exfoliated crystals consist of 2–4 layers of nanosheets. The thickness of ~1.1 nm (e.g. profiles 2 and 3) is consistent with the thickness of exfoliated titania nanosheets.[1] It is noted that according to the AFM studies on different areas the

concentration of non-exfoliated HTO was small and ~100% monolayer nanosheet films could be easily obtained from the solution with short reaction time, by keeping the diluted solution standing for 1 h before LB deposition.

S4. Kinetic model for the exfoliation and restacking reactions

S4.1 Kinetics of sequential exfoliation and restacking reactions

We suppose an initial dispersion of HTO consisting of stacks of nanosheets. The concentration of HTO particles in the dispersion at a given time t is defined as $N_0(t)$. It is assumed that HTO exfoliates into isolated nanosheets following the scheme

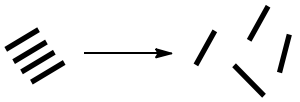

The rate of exfoliation is proportional to the concentration of HTO, i.e.

$$\frac{dN_1(t)}{dt} = k_1 \cdot N_0(t) \qquad (13)$$

Here $N_1(t)$ is the concentration of isolated, unilamellar nanosheets, and k_1 is the rate constant of the 1st order exfoliation reaction.

Following their formation, isolated nanosheets may restack into a hybrid structure. Restacked nanosheets are typically observed as a correlation peak in the SAXS curves when the TBAOH/HTO ratio is larger than 2-3. For the sake of simplicity, we assume here that only nanosheet dimers are formed. This assumption is in fair agreement with the experimental SAXS data after fitting to the FGM model as discussed in the main text. These model fits showed that the average stack number m of the restacked hybrid was < 3 during the first 60 s of reaction (see Figure 3a in the main text). The dimerization reaction can be schematically depicted as

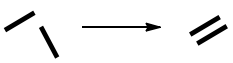

Since two nanosheets are needed to form one dimer, the rate of restacking is proportional to the square of the nanosheet concentration N1(t). Hence, the rate with which nanosheet dimers form can be expressed as

$$\frac{dN_2(t)}{dt} = k_2 \cdot (N_1(t))^2 \qquad (14)$$

Here $N_2(t)$ is the concentration of dimers, and k_2 the rate constant of the dimerization reaction. Since nanosheets are consumed in this reaction, equation (13) should be expanded to include the follow-up reaction, yielding

$$\frac{dN_1(t)}{dt} = k_1 \cdot N_0(t) - 2 \cdot k_2 \cdot (N_1(t))^2 \quad (15)$$

The rate with which nanosheets and dimers are formed is proportional to the rate with which HTO is consumed, i.e.

$$-\alpha \frac{dN_0(t)}{dt} = \frac{dN_1(t)}{dt} + 2\frac{dN_2(t)}{dt} \quad (16)$$

Here α is a proportionality constant that expresses the average number of nanosheets in an initial HTO particle. The factor 2 in the second term on the right hand side indicates the number of nanosheets present in one dimer. By combining equations (14), (15) and (16) we can isolate $dN_0(t)/dt$:

$$\frac{dN_0(t)}{dt} = -\frac{k_1}{\alpha} \cdot N_0(t) \quad (17)$$

By integration we obtain:

$$N_0(t) = N_0(0) \cdot \exp\left(-\left(\frac{k_1}{\alpha}\right) \cdot t\right) \quad (18)$$

Equation (18) is substituted into equation (15):

$$\frac{dN_1(t)}{dt} = k_1 \cdot N_0(0) \cdot \exp\left(-\left(\frac{k_1}{\alpha}\right) \cdot t\right) - 2 \cdot k_2 \cdot (N_1(t))^2 \quad (19)$$

A solution to the differential equation (19) was obtained using a symbolic differential solver in Matlab R2014, which yielded the following general solution:

$$N_1(t) = \frac{A \cdot F(t)}{2 \cdot k_2} \cdot \frac{C \cdot \mathrm{J}_1\left(\frac{A}{B} \cdot F(t)\right) - \mathrm{Y}_1\left(\frac{-A}{B} \cdot F(t)\right)}{C \cdot \mathrm{J}_0\left(\frac{A}{B} \cdot F(t)\right) + \mathrm{Y}_0\left(\frac{-A}{B} \cdot F(t)\right)} \quad (20)$$

Here

$A = \sqrt{-2 \cdot N_0(0) \cdot k_1 \cdot k_2}$,

$B = \frac{k_1}{2 \cdot \alpha}$ and

$F(t) = \exp(-B \cdot t)$.

The functions J_1, J_0, Y_1 and Y_0 are first and zeroth order Bessel functions of the first and second kind, respectively. C is an integration constant and in view of the boundary condition $N_1(0) = 0$, C is defined by

$$C = \frac{Y_1\left(-\frac{A}{B}\right)}{J_1\left(\frac{A}{B}\right)} \tag{21}$$

Since the values of $N_0(0)$, k_1 and k_2 are positive, the value of A is imaginary, and C is a complex number. The imaginary arguments can be diminished by replacing the Bessel function with modified Bessel functions, so that we obtain:

$$N_1(t) = \frac{A_R \cdot F(t)}{2 \cdot k_2} \cdot \frac{K_1\left(\frac{A_R}{B} F(t)\right) - C_R \, I_1\left(\frac{A_R}{B} F(t)\right)}{K_0\left(\frac{A_R}{B} F(t)\right) + C_R \cdot I_0\left(\frac{A_R}{B} F(t)\right)} \tag{22}$$

Here

$$A_R = \left(\frac{A}{i}\right) = \sqrt{2 \cdot N_0(0) \cdot k_1 \cdot k_2} \quad \text{and}$$

$$C_R = \frac{i - C}{2 \cdot \pi} = \frac{K_1\left(\frac{A_R}{B}\right)}{I_1\left(\frac{A_R}{B}\right)} .$$

The values of B and $F(t)$ remain unchanged. The functions I_1, I_0, K_1 and K_0 are first and zeroth order modified Bessel functions of the first and second kind, respectively. The values of A_R and C_R are always real and positive. The rate of dimerization and the concentration of dimers can now be calculated by inserting equation (22) into equation (14) and integrating.

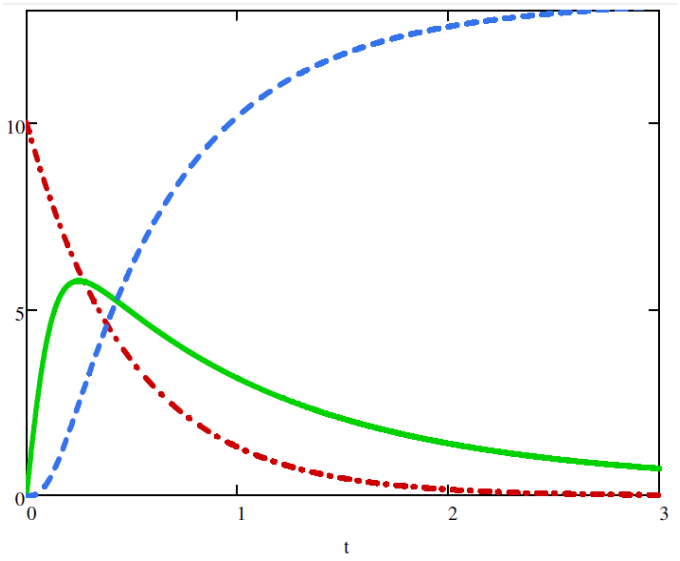

Figure A3. Simulated concentrations of HTO crystals N_0 (red curve), isolated nanosheets N_1 (green curve) and restacked hybrids N_2 (blue curve) based on our model.

For the sake of illustration, the simulated concentrations of N_0 (red curve), N_1 (green curve) and N_2 (blue curve) as a function of time, using arbitrary values $N_0(0) = 10$, $\alpha = 2.7$, $k_1 = 5.5$ and $k_2 = 0.5$, are shown in Figure A3. The concentration of HTO (N_0) decreases steadily. Nanosheets dimers (N_2) are formed after a short incubation time, in qualitative agreement with the experimental SAXS data, as discussed in the main text. Isolated nanosheets (N_1) are formed in the early stages of reaction, followed by their gradual consumption in the following restacking reaction. The concentration $N_2(t)$ increases to an ultimate value of $\frac{1}{2}\alpha N_0(0)$ if the reaction goes to completion.

When the function $N_2(t)$ of the above model is fitted to the experimental data of Figure 3b, reasonably good agreement is found as shown in Figure A4.

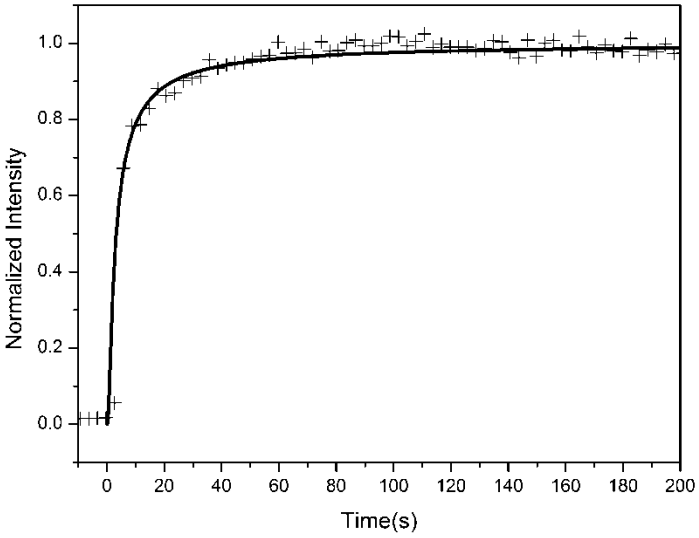

Figure A4. Best fit of our model to the experimental concentrations of restacked hybrids $N_2(t)$ as determined from the peak intensity of the first correlation peak in the SAXS curves.

Two limiting cases of the general kinetic model derived above can be distinguished, and these are discussed in more detail below.

S4.2 Limiting case 1: Exfoliation reaction much faster than restacking reaction

In the first limiting case the rate of nanosheet formation from HTO is much faster than the rate of restacking. This situation typically occurs in the first stages of reaction, when the concentration of HTO is high and the concentration of unilamellar nanosheets that can dimerize is low. Under such conditions the rate of dimer formation is fully limited by the rate of restacking of isolated sheets.

If we assume an infinitely fast exfoliation reaction ($k_1 \rightarrow \infty$), then the concentration of $N_0(t)$ is zero for all t, so that $dN_0(t)/dt = 0$. Equation (16) can then be simplified to

$$\frac{dN_1(t)}{dt} + 2\frac{dN_2(t)}{dt} = 0 \qquad (23)$$

Combination of equation (23) with the rate of dimer formation, equation (14) leads to

$$\frac{dN_1(t)}{dt} = -2k_1 N_1(t)\, N_1(t) \tag{24}$$

Solving equation (24) leads to

$$\frac{1}{N_1(t)} - \frac{1}{N_1(0)} = 2k_1 t \tag{25}$$

Since all HTO transformed into nanosheets at $t = 0$, it follows that $N_1(0) = \alpha N_0(0)$ and that $N_1(0) = N_1(t) + 2N_2(t)$. Hence, the final expression for $N_2(t)$ under these conditions reads

$$N_2(t) = \frac{1}{2} N_1(0)\left(1 - \frac{1}{1+2k_1 N_1(0) t}\right) \tag{26}$$

This equation is typical for 2nd order kinetic processes. Since $N_2(t)$ may be assumed to scale with the intensity of the SAXS correlation peak of the restacked structure, Equation (26) was fitted to the experimental data in Figure 3b (second order fitting curve).

S4.3 *Limiting case 2: Restacking reaction much faster than exfoliation reaction*

In the second limiting case, the rate of nanosheet formation from HTO is much slower than the rate of restacking. This situation typically occurs in the later stages of reaction, where the concentration of HTO is low and the concentration of unilamellar nanosheets is relatively high. Under such conditions the rate of dimer formation is fully limited by the rate of formation of isolated sheets.

If we assume that the dimerization reaction is infinitely fast ($k_2 \rightarrow \infty$), then the concentration of nanosheets $N_1(t)$ is (very close to) zero, so that

$$\alpha N_0(0) = \alpha N_0(t) + 2N_2(t) \tag{27}$$

Upon inserting equation (18) into equation (27), a final expression for $N_2(t)$ under these conditions is obtained:

$$N_2(t) = \frac{\alpha N_0(0)}{2}\left(1 - \mathrm{e}^{-\frac{k_1 t}{\alpha}}\right) \tag{28}$$

This equation is typical for 1st order kinetic processes. Since the concentration of dimers $N_2(t)$ may be assumed to scale with the intensity of the SAXS correlation peak of the restacked structure, Equation (28) was fitted to the experimental data in Figure 3b (first order fitting curve).

S5. Proposed exfoliation chemistry

The reason for the uptake of protons is possibly related to the dimension mismatch between TBA^+ and nanosheets and mobility differences between protons and TBA^+. It has been reported that the HTO crystals in this study have a charge density of $4.72q_e$ nm^{-2}, where q_e is the electron charge (1.6×10^{-19} C).[6] The data presented in our study show that the charge density of nanosheets is higher because of reduction of Ti^{4+} upon exfoliation. But given the molecular size of TBA^+, one TBA^+ ion has a charge density of $1.63q_e$ nm^{-2} only.[7] So the number of TBA^+ ions that can compensate the net negative charge on the nanosheet surface is insufficient, and the exfoliated sheets need additional positive charge (protons) to compensate their negative charge. Such charge compensation may take place by adsorption of protons forming a hydroxyl-covered surface, as was indeed confirmed by FTIR data. It is noted that next to TBA^+ ions and protons adsorbed on the surface of nanosheets, some TBA^+ ions will also remain in the diffuse double layer to play a role in the charge compensation process. However, the Debye length of the colloidal solution used here is ~0.87 nm, which indicates that complete charge compensation occurs very close to the surface of the nanosheets. Moreover, the mobility of H^+ (self-diffusion coefficient $D = 7.62 \times 10^{-9}$ m^2 s^{-1})[8] is much higher than that of TBA^+ (self-diffusion coefficient $D \ll 2 \times 10^{-14}$ m^2 s^{-1}).[9] So it is probable that due to their small size and high mobility, protons have a higher chance than TBA^+ to be absorbed by the negatively charged nanosheets and form hydroxyl groups. The observation of a small but continuous pH decrease after more than 500 s of mixing in the *in situ* pH experiments at a TBAOH/HTO ratio of 4 : 1, as shown in the figure directly below, can thus be explained by slow exchange of TBA^+ ions in solution and protons absorbed by nanosheets. So it is likely that even though the acid-base reaction, the exfoliation reaction and the restacking reaction occur fast, the final equilibration of protons and TBA^+ is relatively slow.

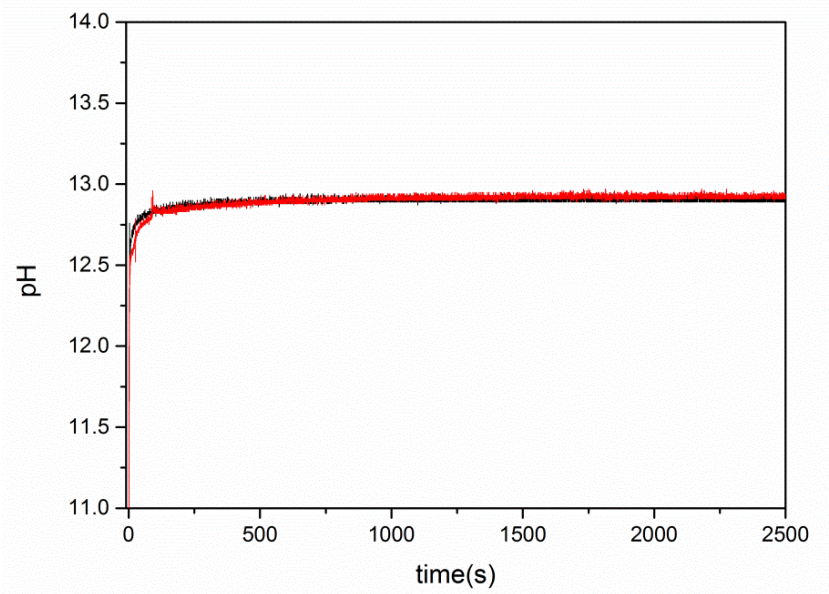

Figure A5. pH change of HTO solution after mixing with TBAOH (TBAOH/HTO ratio = 4 : 1, c_{HTO}=5 g/l) over a longer period of time. The black line is the reaction curve, and the red line is the reference curve.

Figure A5 shows the pH change of an HTO solution after mixing with TBAOH (TBAOH/HTO ratio = 4 : 1, c_{HTO}=5 g/l) over a longer period of time. It can be seen that the pH decreased slightly after 500 s.

Based on our observations, we propose a chemical reaction mechanism for the reaction of HTO with TBAOH as shown below, which would guide for the exfoliation of other compounds driven by chemical reaction.

$$x\mathrm{OH^-} + x\mathrm{TBA^+} + \mathrm{H}_x\mathrm{TO(bulk)} \rightarrow \mathrm{TO^-(sheet)} + x\mathrm{TBA^+} + x\mathrm{H_2O}\ x < 1 \quad (29)$$

$$\mathrm{TO^-(sheet)} + y\mathrm{TBA^+} + (1\text{-}y)\mathrm{H_2O} \rightarrow (1\text{-}y)\mathrm{OH^-} + \mathrm{H}_{(1\text{-}y)}\mathrm{TBA}_y\mathrm{TO(sheet)}\ \ y<0.345^* \quad (30)$$

* When one layer of TBA+ ions fully covers the surface of titania nanosheets, there is only 1/4.72=0.212 nm^2 to accommodate TBA^+ ions to compensate one negative charge on nanosheets. The equivalent charge carried by 0.212 nm^2 TBA^+ ions is 0.346 q_e. So TBA^+ ions can only compensate 0.346 q_e out of one negative charge on the nanosheet surface.

First the acid-base reaction between HTO and TBAOH takes place and triggers the exfoliation reaction (17). The layered HTO structure loses its stability and exfoliation begins. Because of partial reduction of Ti^{4+} ions, dimension mismatch

between HTO and TBA^+, and mobility differences between protons and TBA^+ ions, water molecules are dissociated by exfoliated nanosheets, forming protons for charge compensation and releasing OH^- into solution (reaction (18)). The OH^- ions formed in reaction (18) can then participate in the acid-base reaction (17) to form more exfoliated nanosheets when there are sufficient TBA^+ ions available to separate the nanosheets. If no sufficient number of TBA^+ ions is available, then reaction (19) occurs, as was indicated by the pH change at a TBAOH/HTO ratio of 1 : 4 (Figure 4d).

$$z\mathrm{OH}^- + \mathrm{H}_x\mathrm{TO(bulk)} \rightarrow \mathrm{H}_{(x-z)}\mathrm{TO}^{z-}\mathrm{(bulk)} + z\mathrm{H_2O} \quad z << x \qquad (31)$$

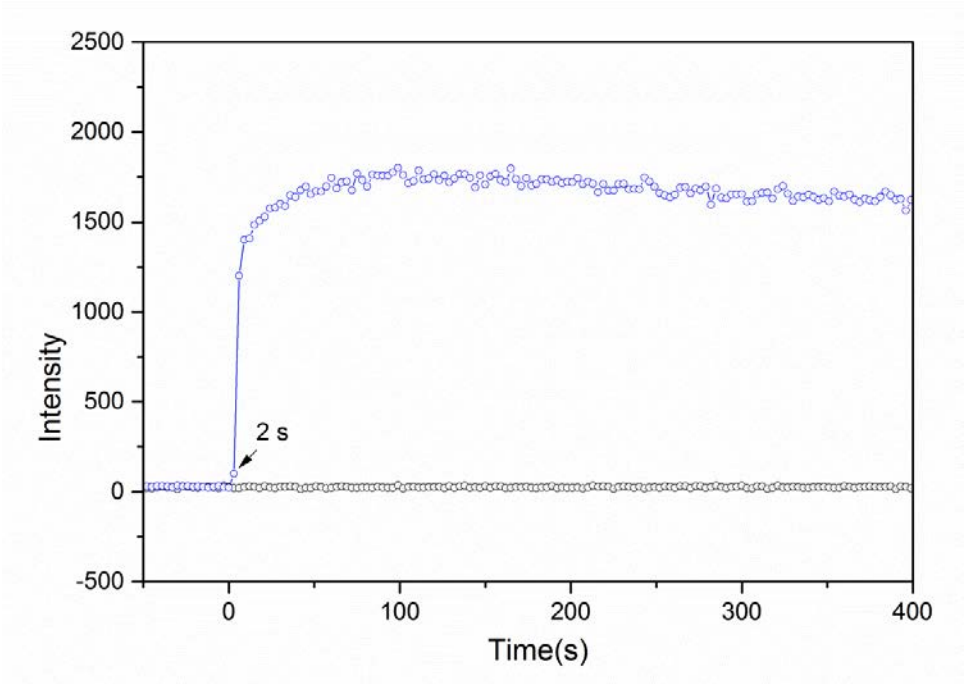

Figure S1. Scattering intensity (peak height) change at q = 0.622 nm^{-1} in the experiments with HTO (blue; TBAOH/HTO = 4) and without HTO (black). When HTO was absent, the injection of TBAOH did not introduce insignificant changes in the scattering intensity.

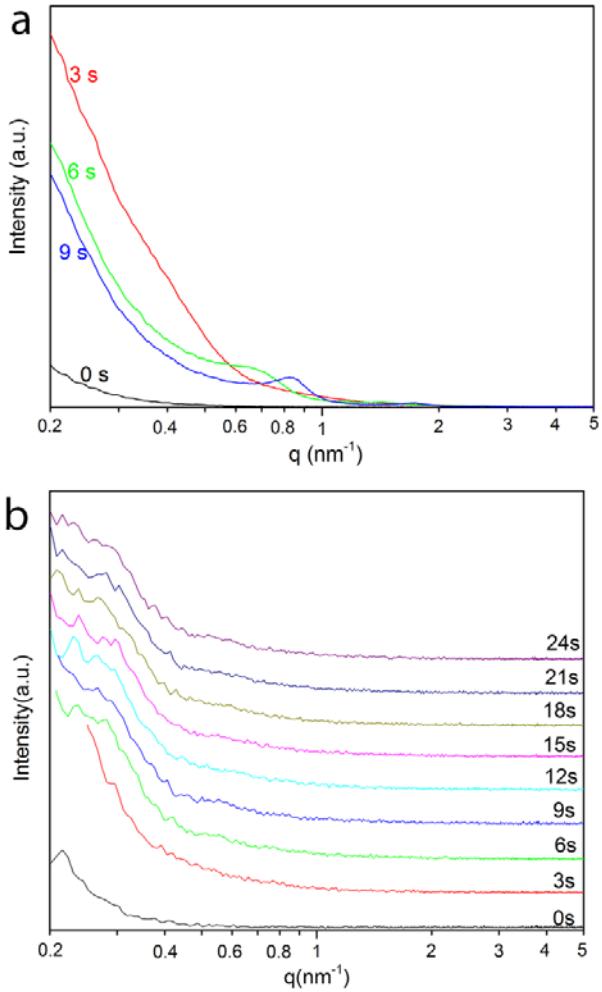

Figure S2. (a) SAXS curves of HTO after mixing with TBAOH (TBAOH/HTO molar ratio = 6 : 1, c_{HTO}=5 g/l) during the first 9 s after mixing. The same feature as in the main text, fast formation of isolated nanosheets before restacking, was found; (b) SAXS curves of HTO in mixing process with TBAOH (TBAOH/HTO molar ratio = 1 : 1, c_{HTO}=5 g/l) in the first 24 s after mixing. No correlation peaks were recorded, indicating that the HTO crystals were directly exfoliated into individual nanosheets, rather than that ion intercalation led to an intermediate swollen state prior to exfoliation.

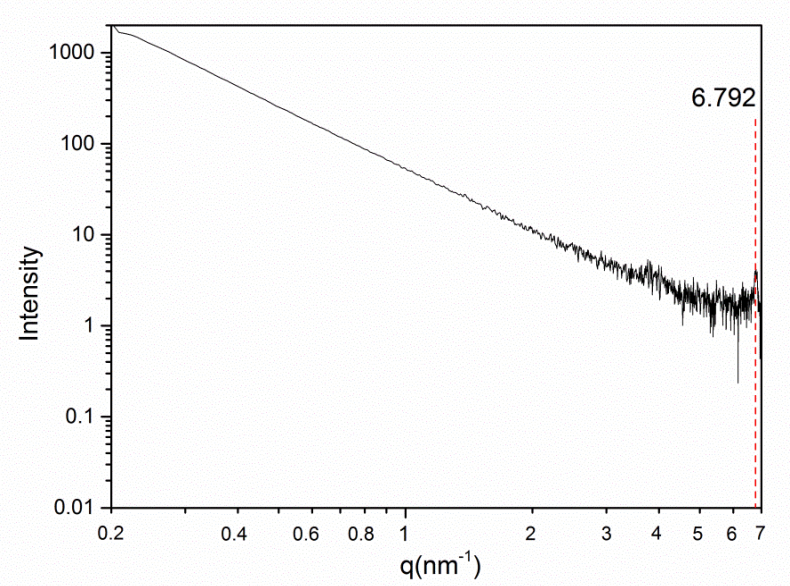

Figure S3. SAXS data of a colloidal solution of HTO and tetrabutyl ammonium bromide (TBABr) after 4 weeks of reaction. The TBABr/HTO molar ratio is 4. The correlation peak at q = 6.792 nm^{-1} indicates that the original layered HTO structure with an interlayer spacing of 0.92 nm was still present.

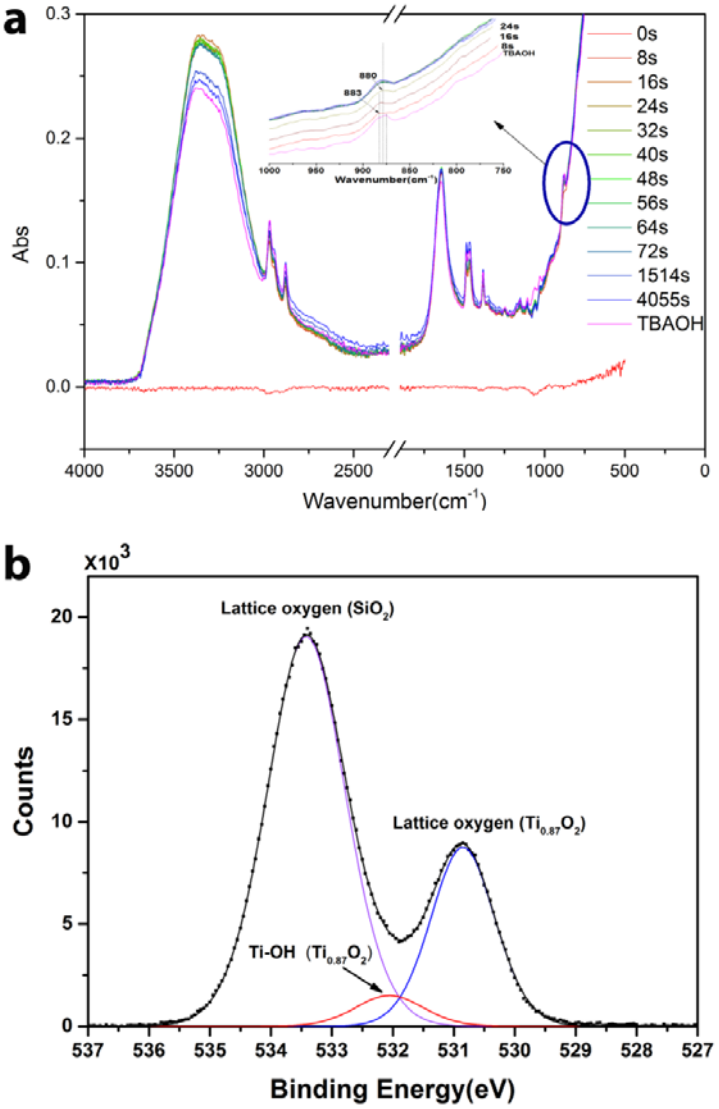

Figure S4. (a) Time-resolved FTIR data at a TBAOH/HTO molar ratio of 4 : 1. (b) High resolution O 1*s* XPS spectra of monolayer $Ti_{0.87}O_2$ nanosheets. The peak at 533.4 eV can be assigned to lattice oxygen of silica on the oxidized silicon substrate surface.[10] The peaks at 530.8 eV and 532.0 eV can be assigned to lattice oxygen in lepidocrocite-type titanates, and hydroxyl oxygens.[11] The presence of hydroxyl groups indicates that the protons were absorbed onto nanosheets to form hydroxyl groups after the acid-base and exfoliation reactions.

Table S1. Final pH values of solutions with different ratios of TBAOH/HTO after 30 min of reaction.

TBAOH/HTO ratio	**pH**	
	Reference curve	*Reaction curve*
2:1	12.71	12.67
1:1	12.34	12.31
1:2	12.01	11.78
1:4	11.70	10.71

REFERENCES

1. T. Tanaka, Y. Ebina, K. Takada, K. Kurashima, T. Sasaki, *Chem. Mat.* **2003**, *15*, 3564-3568.

2. W. Bras, I. P. Dolbnya, D. Detollenaere, R. van Tol, M. Malfois, G. N. Greaves, A. J. Ryan, E. Heeley, *Journal of Applied Crystallography* **2003**, *36*, 791-794.

3. aJ. Connolly, J. S. van Duijneveldt, S. Klein, C. Pizzey, R. M. Richardson, *Langmuir* **2006**, *22*, 6531-6538; bC. Pizzey, S. Klein, E. Leach, J. S. van Duijneveldt, R. M. Richardson, *Journal of Physics: Condensed Matter* **2004**, *16*, 2479.

4. R. Besselink, T. M. Stawski, H. L. Castricum, D. H. A. Blank, J. E. ten Elshof, *J. Phys. Chem. C* **2010**, *114*, 21281-21286.

5. T. Sasaki, M. Watanabe, *The Journal of Physical Chemistry B* **1997**, *101*, 10159-10161.

6. T. Sasaki, F. Kooli, M. Iida, Y. Michiue, S. Takenouchi, Y. Yajima, F. Izumi, B. C. Chakoumakos, M. Watanabe, *Chem. Mat.* **1998**, *10*, 4123-4128.

7. T. Sasaki, M. Watanabe, *Mol. Cryst. Liq. Cryst. Sci. Technol. Sect. A-Mol. Cryst. Liq. Cryst.* **1998**, *311*, 417-422.

8. S. H. Lee, J. C. Rasaiah, *The Journal of Chemical Physics* **2011**, *135*, 124505.

9. A. G. Stepanov, A. G. Maryasov, V. N. Romannikov, K. I. Zamaraev, *Magnetic Resonance in Chemistry* **1994**, *32*, 16-23.

10. E. Görlich, J. Haber, A. Stoch, J. Stoch, *J. Solid State Chem.* **1980**, *33*, 121-124.

11. aT. Gao, P. Norby, H. Okamoto, H. Fjellvåg, *Inorg. Chem.* **2009**, *48*, 9409-9418; bA. Atrei, A. M. Ferrari, D. Szieberth, B. Cortigiani, G. Rovida, *Phys. Chem. Chem. Phys.* **2010**, *12*, 11587-11595.

Chapter 3

Rapid synthesis of metal oxides nanosheets and their Langmuir Blodgett films

Nanosheet concentration at the liquid-air interface (LAI) is a key parameter to several applications, such as Langmuir Blodgett deposition for nanosheet thin films. Investigation of nanosheet concentration at the LAI regarding the synthesis conditions is one of key steps to understand the relevant process and archive controllable fabrication in those applications. In this chapter, the nanosheet concentration at the LAI was investigated by considering the trends of lift-up point (LUP) in the surface pressure-surface area isotherm of LB films as a function of process conditions. The nanosheet concentration in the bulk solution was also studied in sake of comparison. The results show that the time dependencies of the nanosheet concentrations in the bulk and at the interface are quite different.

*A manuscript based on this chapter is under preparation.

3.1 INTRODUCTION

Two-dimensional (2D) materials known also as nanosheets have large potential applications in optoelectronics, spintronics, catalysts, chemical and biological sensors, supercapacitors, solar cells, and lithium ion batteries.[1-4] Their 2D nature offers a path for researchers to design and develop advanced materials and devices.[5-7] Research interests in 2D materials has increased largely over the last decade.[1,2,5] To date, a large number of 2D materials have been discovered and synthesized in laboratories, such as graphene,[8] metal oxides,[9] layered metal dichalcogenides,[10] clays,[11] layered double hydroxides,[12] and MXenes.[4] However, in order to bring the application of 2D materials on industrial scale forward, a facile synthesis method to make them in large quantities is needed.[13] Among the several available synthesis methods for 2D materials, liquid exfoliation has been identified as the most promising strategy for large-scale production.[14] Ion intercalation exfoliation, one of the liquid exfoliation methods, has shown to function well for a large number of layered ionic compounds and yields high quality monolayer nanosheets.[14,15] One of its important advantages compared to other exfoliation techniques is that monolayer nanosheets obtained by ion intercalation exfoliation can be transferred from the liquid-air interface to a solid substrate by deposition techniques such as Langmuir-Blodgett (LB) deposition.[16] The obtained nanosheet films have shown to have advantages in crystal engineering for oriented thin film growth.[17-19]

The mechanism of exfoliation has been intensively for layered titanates ($H_{0.7}Ti_{1.824}O_4 \cdot H_2O$ and $H_{1.07}Ti_{1.73}O_4 \cdot H_2O$).[16,20-22] For layered titanates, exfoliation is normally achieved by mixing protonated layered titanates with tetrabutylammonium hydroxide (TBAOH). The exfoliation of layered titanates is triggered by an acid-base reaction between TBAOH and protonated layered titanates.[22] This exfoliation process is very rapid and can yield monolayer nanosheets in a minute time or less.[22] The molar ratio $TBAOH/H^+$ (where H^+ refers to the number of protons in the protonated titanates) is one of most important parameters for exfoliation. When the molar ratio $TBAOH/H^+$ is as low as 1/16, the yield of nanosheets is low and the obtained nanosheets are relatively defective. When the molar ratio $TBAOH/H^+$ is higher than 1/2, isolated nanosheets form but restacking occurs to some degree.[16] The restacking process, which is known also as precipitation, reduces the yield of

isolated colloidal nanosheets, which makes the synthesis window for titania nanosheets narrow. [16,21,23]

To date, most research on exfoliation is carried out to gain information on nanosheet suspensions. Few reports are available on the yield of nanosheets at the liquid-air interface (LAI) under different synthesis conditions, although it is of prime importance for deposition techniques such as LB deposition. A method to evaluate the yield of nanosheets at the liquid-air interface semi-quantitatively is by monitoring the lift-up point (LUP) in the surface pressure-surface area isotherm of LB films as they are being formed. The formation of LB films made from nanosheets usually goes through three stages, as illustrated in Figure 1. In a very dilute nanosheet solution, the concentration of nanosheets at the LAI is so low that the surface pressure between the barriers increases only slowly upon compression (stage 1). When the barriers have been compressed until the point that the concentration of nanosheets between the barriers is high enough so that they start interacting, then the surface pressure increases more rapidly (stage 2). Further compression introduces a dense monolayer nanosheet film (stage 3). Beyond this point, the surface pressure tends to saturate. The dense nanosheet film may even collapse if the compression proceeds too far. The LUP is determined by extrapolation of the rapid increase of surface pressure in stage 2 to zero pressure as shown in Figure 1.

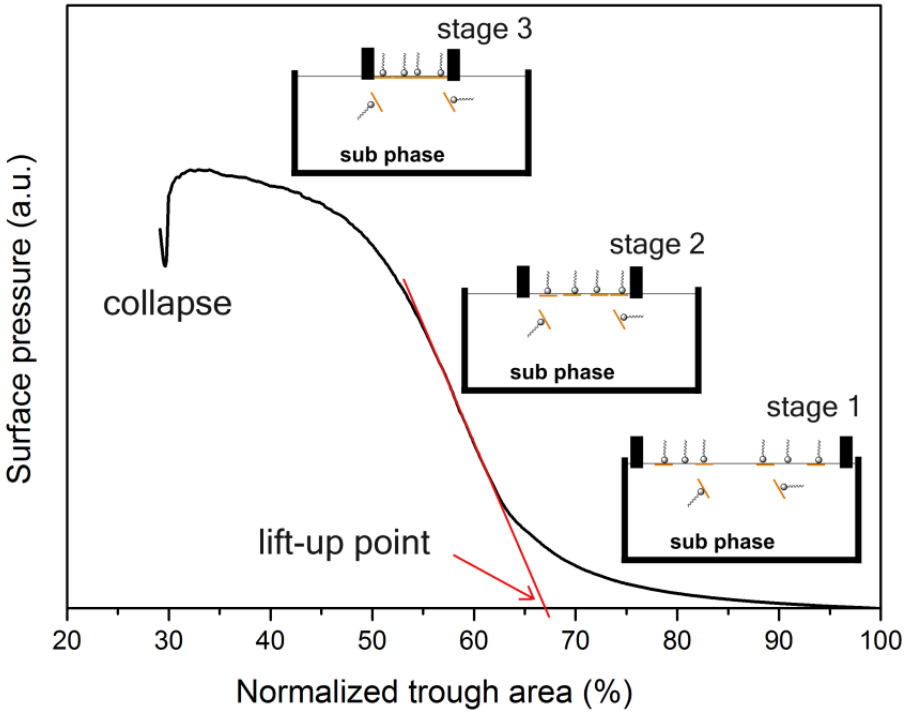

Figure 1. Surface pressure – surface area isotherm of a dilute nanosheet solution. The lift-up point in this curve is at 67%. In stage 1, free floating nanosheets at the LAI; surface pressure is low and increases slowly; In stage 2, the nanosheets are approaching each other; surface pressure increases rapidly; In stage 3, a dense nanosheet film forms; surface pressure is more or less constant.

In this chapter, we studied the yield of nanosheets at the LAI by exfoliation of the layered titanate $H_{1.07}Ti_{1.73}O_4 \cdot H_2O$ (HTO) as a function of molar ratio $TBAOH/H^+$ and reaction time. The nanosheet concentration at the LAI was evaluated by considering the trends in the LUP as a function of process conditions. For the sake of comparison, UV-Vis spectroscopy was employed in order to gain information on the nanosheet concentration in the bulk of the solution.

3.2 EXPERIMENTAL SECTION

Materials. Titanium (IV) dioxide TiO_2 (Ridel-de Haen), molybdenum (VI) oxide MoO_3 (Sigma-Aldrich), anhydrous potassium carbonate K_2CO_3 (Fluka), and lithium carbonate Li_2CO_3 (Ridel-de Haen) had a purity of 99.0% or higher and were used as

received. Tetra *n*-butylammonium hydroxide TBAOH (40 wt% H_2O, Alfa Aesar) was used as received. Demineralized water was used throughout the experiments.

Preparation of lepidocrocite-type protonated layered titanate and its nanosheet suspension. The $K_{0.80}Ti_{1.73}Li_{0.27}O_4$ (KLTO) precursor was obtained with a flux method developed by Tanaka et al.[24] TiO_2, K_2CO_3, Li_2CO_3, and MoO_3 (1.73:1.67:0.13:1.27 molar ratio) were heated to 1150°C, held at that temperature for 30 min, and then slowly cooled down to 950 °C at a speed of 4 °C/h. The oven was then allowed to cool to room temperature by natural cooling. The resulting KLTO powder was washed 3 times in 250 mL water to remove K_2MoO_4. Then KLTO powder was dispersed in a 2 mol/L HNO_3 solution (250 mL) at room temperature while stirring. The acidic solution was replaced daily by a fresh one via decantation. After treatment for 3 days, the acid-exchanged crystals were collected by filtration and washed with a copious quantity of pure water, then air dried to get HTO powder.

Samples were made by mixing 0.1 g of HTO with water and TBAOH with a $TBAOH/H^+$ molar ratio of 1/32, 1/16, 1/8, 1/4, 1/2, 1/1, 2/1, 4/1, 6/1 and 8/1 to a total volume of 20 mL solution. The mixtures were stirred for 2 h. The solutions were then directly used for UV-visible absorption spectroscopy and LB deposition experiments. The time dependency experiments were made using solutions with a $TBAOH/H^+$ molar ratio of 4/1. In a total volume of 20 mL solution, 0.1 g of HTO was used for each sample while stirring for different reaction times, and then used as described below to estimate the nanosheet concentrations at the LAI and in the bulk.

Evaluation of nanosheet concentration at the liquid-air interface. To obtain a suspension for surface pressure-surface area isotherm experiments, 2 mL of the above solutions after reaction for a given amount of time were diluted to 500 mL by adding demineralized water. The diluted suspensions were then left standing for 1 h. 50 mL was taken from the middle or top part of the nanosheet suspension using a syringe for the pressure-surface area isotherm experiments. After the separated suspension was poured into a Langmuir Blodgett trough (KSV Minimicro, a Teflon trough with an active trough surface area of 100 cm^2, L195 x W51 x D4 mm^3 and a dipping well L10 x W28 x D28 mm^3, trough volume 48 cm^3), a stabilization time of 10 min was used to equilibrate and stabilize the surface pressure before compression.

After stabilization, the surface pressure was set to zero and then the compression process was started using a compression speed of 3 mm/min. The compression process continued for about 20 min until a minimum trough area of 30 % of the initial surface area had been reached, unless the surface pressure was already saturated at higher trough area.

Characterization. UV-Vis spectra of samples were recorded with a Cary 50 UV-Vis spectrophotometer in transmission mode. The original suspensions were diluted 300 times by volume in order to obtain an appropriate range of absorbances. Small angle X-ray scattering (SAXS) experiments were carried out using synchrotron radiation on the Dutch-Belgian beamline, DUBBLE BM-26B of the European Synchrotron Radiation Facility (ESRF) in Grenoble.[25] A home-made solution cycling setup including a SAXS measurement chamber, a mixing chamber, a timing injection system and a pump system allowed us to do *in situ* SAXS measurements directly after mixing HTO and TBAOH solutions. The flow was placed in up and down direction. Background scattering data were recorded using demi-water cycled in the setup. After taking the background sample measurement, *in situ* SAXS measurements were started. SAXS scattering curves were recorded every 30 s. For details about the SAXS configuration the reader is referred to ref. 22.

3.3 RESULTS AND DISCUSSION

3.3.1 TBA/H^+ dependence of nanosheets formation.

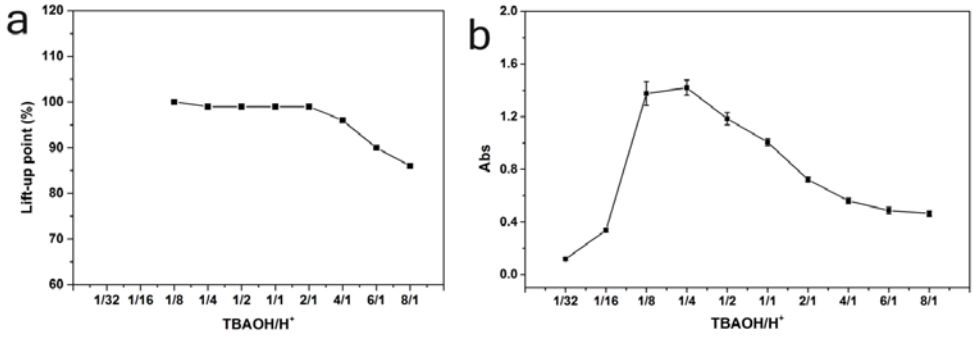

Figure 2. (a) Lift-up point and (b) absorbance of diluted suspensions at TBAOH/H^+ molar ratios of 1/32 to 8/1 after reaction time of 2 h.

The influence of molar ratio TBAOH/H^+ on the concentration of nanosheets at both the LAI and in the bulk of the solution were investigated, and the results are shown

in Figure 2 (See Figure S1 for further details). Figure 2a shows the change of the LUP at different molar ratio TBAOH/H^+. It is noted that the LUP for solutions with a nominal molar ratio TBAOH/H^+ of 1/32 and 1/16 was too low to be measured under our experimental conditions, so these data are omitted. However, at a molar ratio TBAOH/H^+ of 1/8 the LUP was close to 100 %, which indicates that the nanosheet concentration at the LAI was high under these conditions. The LUP remained constant with increasing TBAOH concentration until a molar ratio TBAOH/H^+ of 2/1, and decreased at even higher values. A study of the optical absorption spectrum shows that the absorption peak (Figure S1b) is located at 265 nm, which is consistent with previous reports.[16,26] The peak absorbance at 265 nm provides an estimate of the nanosheet concentration in the bulk of the solution. The change of absorbance is plotted in Figure 1b. The absorbance increased with molar ratio TBAOH/H^+ until a molar ratio TBAOH/H^+ of 1/4, and decreased upon further increase of TBAOH/H^+. These optical data are consistent with our previously reported results on layered titanate nanosheets.[16] The absorbance change demonstrates that the nanosheet yield increases with increasing molar ratio TBAOH/H^+ when TBAOH/H^+ < 1/4, while restacking occurs when TBAOH/H^+ is higher than 1/4.[16] Our results suggest that even though restacking occurs at low molar ratio of 1/4, the restacking process in the bulk has only a minor negative effect on the concentration of nanosheets at the LAI even at TBAOH/H^+ molar ratios >2. It is noted that the nanosheet concentration at the LAI reached a high value even at low TBAOH/H^+, but the layer exhibited a tendency towards collapsing, indicating that the monolayer was not stable compared to monolayers formed at higher TBAOH/H^+ (See Figure S1a).

3.3.2 Time dependence of nanosheets formation

Figure 3 shows the influence of reaction time on the LUP and the absorbance of the nanosheet suspension (Experimental details shown in Figure S2). The LUP had a stable value during the first 6 h. The LUP slightly decreased at t > 6 h, and finally decreased strongly after 3 days. Since the LUP provides an indication of the nanosheet concentration at the LAI, the data show that the concentration of nanosheets at the LAI is higher after short reaction times than after prolonged reaction times. Moreover, the LUP value close to 100 % after only 30 s shows that sufficient nanosheets formed rapidly to for a saturated monolayer at the LAI. The

formation of a dense nanosheet layer at the LAI after short reaction times and the drastic decrease of interface nanosheet concentration after long reaction (exfoliation) times were also observed on protonated calcium niobate and protonated iron titanate (See Figure S3). These results are in agreement with our findings in a previous *in situ* SAXS study that the exfoliation of these layered oxides is a rapid process.[22]

Figure 3b shows the UV-vis absorption spectra of nanosheet solutions, providing an estimate of the concentration of nanosheets in the bulk. The absorbance increased significantly after 2 h of reaction time, and reached a maximum value after 3 days. The reason for the increasing absorbance is thought to be the exfoliation of restacked nanosheets by mechanic force introduced by stirring. The details are discussed below. Comparison of these data with the trend shown in Figure 3a shows that the nanosheet concentration at the LAI is not positively correlated with the nanosheet bulk concentration for long reaction times. The two regions seem to exhibit independent behavior with respect to the nanosheet concentration. For applications such as LB deposition, a short time of exfoliation seems to be more suitable to form a dense film efficiently.

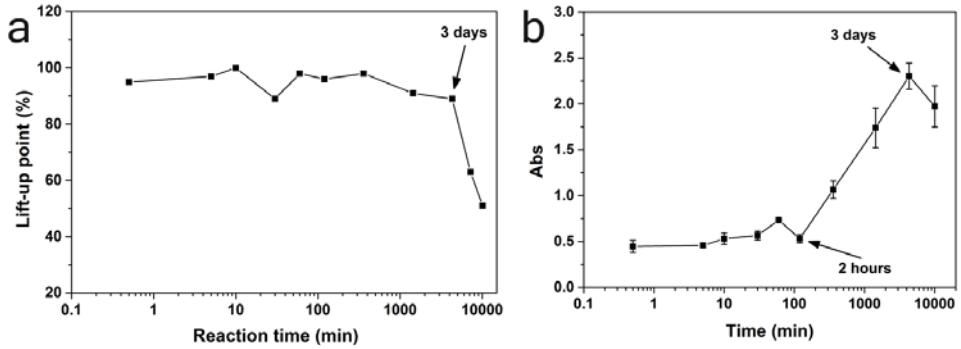

Figure 3. (a) The lift-up point and (b) UV-Vis absorbance of suspensions after different reaction times. The TBAOH/H^+ molar ratio was 4/1.

The optical absorption increased after 2 h which suggests that the nanosheet concentration in the bulk increased. To confirm this hypothesis, a long term SAXS experiment was carried out. Figure 4 shows SAXS curves at a nominal TBAOH/H^+ molar ratio of 4/1 and a nominal nanosheet concentration of 5 g/L. Very rapid exfoliation was observed, in agreement with earlier findings.[22] Details of the first 2 frames of the *in situ* SAXS data showing rapid exfoliation and subsequent restacking, not clearly visible in Figure 4, can be found in the APPENDICES, Figure S4.

However, the restacked structure was exfoliated again after more than 2 h, which is evidenced by the gradual vanishing of the correlation peaks in Figure 4. It is noted that exfoliation of the restacked structure after a prolonged period of time was not reported in our previous paper,[22] as the main focus of that paper was on short time experiments and the high rate of exfoliation of the layered structure due to acid-base reaction irrespective of TBAOH/H^+ molar ratio.[22] Our current data show that the restacked structure became exfoliated again at a TBAOH/H^+ molar ratio of 4/1, which leads to an increasing nanosheet concentration in the bulk.

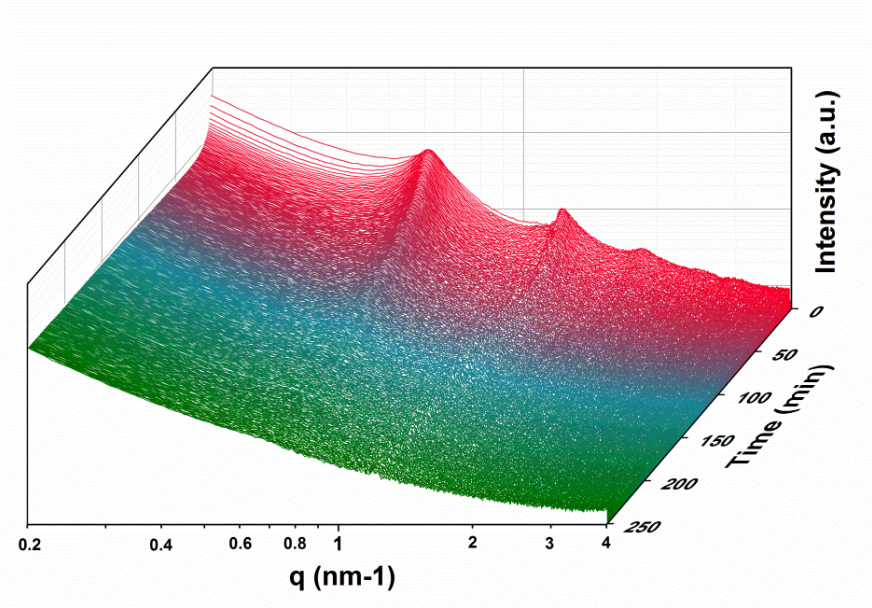

Figure 4. Time resolved SAXS curves in the *q*-range 0.2 – 4 nm^{-1} at TBAOH/H^+ molar ratios of 4/1 and nominal nanosheet concentration of 5 g/L.

3.4 CONCLUSIONS

The influence of exfoliation conditions on nanosheet concentration both at the LAI and in the bulk of the solution was investigated. With increasing molar ratio TBAOH/H^+, the nanosheet concentration at the LAI and in the bulk of the solution increased largely, although the stability of nanosheet monolayers formed at the LAI was much higher at high ratios TBAOH/H^+. Even though restacking occurred at high molar ratio TBAOH/H^+, under the experimental conditions the restacking process

did not retard the formation of nanosheets at the LAI. The time dependent study shows that even short time reaction periods are sufficient for the formation of a high concentration of nanosheets at the LAI. When the reaction time is longer than 3 days, the nanosheet concentration at the LAI became much lower. The results also demonstrate that the nanosheet concentration at the LAI is not (positively) correlated with the concentration of nanosheets in the bulk of the solution. The time dependencies of the concentrations of nanosheets in the bulk and at the interface are quite different. Our results are useful to guide for further fabrication research of 2D materials using deposition techniques such as Langmuir Blodgett deposition.

REFERENCES

1. Xu, M.; Liang, T.; Shi, M.; Chen, H. *Chem. Rev.* **2013**, *113*, 3766.

2. Geim, A. K.; Novoselov, K. S. *Nat. Mater.* **2007**, *6*, 183.

3. Peng, X.; Peng, L.; Wu, C.; Xie, Y. *Chemical Society Reviews* **2014**, *43*, 3303.

4. Naguib, M.; Mochalin, V. N.; Barsoum, M. W.; Gogotsi, Y. *Adv. Mater.* **2014**, *26*, 992.

5. Geim, A. K.; Grigorieva, I. V. *Nature* **2013**, *499*, 419.

6. Stankovich, S.; Dikin, D. A.; Dommett, G. H. B.; Kohlhaas, K. M.; Zimney, E. J.; Stach, E. A.; Piner, R. D.; Nguyen, S. T.; Ruoff, R. S. *Nature* **2006**, *442*, 282.

7. Osada, M.; Sasaki, T. *Adv. Mater.* **2012**, *24*, 210.

8. Novoselov, K. S.; Geim, A. K.; Morozov, S. V.; Jiang, D.; Zhang, Y.; Dubonos, S. V.; Grigorieva, I. V.; Firsov, A. A. *Science* **2004**, *306*, 666.

9. Osada, M.; Sasaki, T. *J. Mater. Chem.* **2009**, *19*, 2503.

10. Chhowalla, M.; Shin, H. S.; Eda, G.; Li, L.-J.; Loh, K. P.; Zhang, H. *Nature Chemistry* **2013**, *5*, 263.

11. Alexandre, M.; Dubois, P. *Materials Science and Engineering: R: Reports* **2000**, *28*, 1.

12. Ma, R. Z.; Liu, Z. P.; Li, L.; Iyi, N.; Sasaki, T. *J. Mater. Chem.* **2006**, *16*, 3809.

13. Cai, M.; Thorpe, D.; Adamson, D. H.; Schniepp, H. C. *J. Mater. Chem.* **2012**, *22*, 24992.

14. Nicolosi, V.; Chhowalla, M.; Kanatzidis, M. G.; Strano, M. S.; Coleman, J. N. *Science* **2013**, *340*.

15. Ma, R.; Sasaki, T. *Accounts Chem. Res.* **2014**.

16. Yuan, H.; Lubbers, R.; Besselink, R.; Nijland, M.; ten Elshof, J. E. *ACS Appl. Mater. Interfaces* **2014**, *6*, 8567.

17. Shibata, T.; Fukuda, K.; Ebina, Y.; Kogure, T.; Sasaki, T. *Adv. Mater.* **2008**, *20*, 231.

18. Nijland, M.; Kumar, S.; Lubbers, R.; Blank, D. H. A.; Rijnders, G.; Koster, G.; ten Elshof, J. E. *ACS Appl. Mater. Interfaces* **2014**, *6*, 2777.

19. Shibata, T.; Ebina, Y.; Ohnishi, T.; Takada, K.; Kogure, T.; Sasaki, T. *Crystal Growth & Design* **2010**, *10*, 3787.

20. Wang, L.; Sasaki, T. *Chem. Rev.* **2014**, *114*, 9455.

21. Besselink, R.; Stawski, T. M.; Castricum, H. L.; Blank, D. H. A.; ten Elshof, J. E. *J. Phys. Chem. C* **2010**, *114*, 21281.

22. Yuan, H.; Dubbink, D.; Besselink, R.; ten Elshof, J. E. *Angewandte Chemie International Edition* **2015**, *54*, 9239.

23. Sasaki, T.; Watanabe, M. *J. Am. Chem. Soc.* **1998**, *120*, 4682.

24. Tanaka, T.; Ebina, Y.; Takada, K.; Kurashima, K.; Sasaki, T. *Chem. Mat.* **2003**, *15*, 3564.

25. Bras, W.; Dolbnya, I. P.; Detollenaere, D.; van Tol, R.; Malfois, M.; Greaves, G. N.; Ryan, A. J.; Heeley, E. *Journal of Applied Crystallography* **2003**, *36*, 791.

26. Sasaki, T.; Watanabe, M. *The Journal of Physical Chemistry B* **1997**, *101*, 10159.

APPENDICES

Experimental details of calcium niobate and iron titanate nanosheets: Precursor crystals $KCa_2Nb_3O_{10}$ (KCNO) were synthesized by the conventional solid state reaction.[1] The raw materials of K_2CO_3: $CaCO_3$: Nb_2O_5 were mixed with a molar ratio of 1.1: 4: 3, then put into an alumina crucible. The mixture was heated with a heating rate of 5 °C/min to a temperature of 900 °C, at which temperature it was heated for 4 hours. Then, the mixture was heated to a temperature of 1150 °C with 0.5 °C/min heating rate and kept there for 10 hours. The powder was collected after cooling to room temperature by natural cooling. Protonation of KCNO was took place in 5 M HNO_3 solution with a K^+: H^+ of 1 : 20 for 3 days and the solution was refreshed every day. Then the resultant powder was collected after washing with large quantities of water.

The preparation of the $K_{0.8}[Ti1_{.2}Fe_{0.8}]O_4$ (KFTO) and the protonation were done following Geng *et al*.[2] A reaction mixture containing the starting materials titanium (IV) dioxide TiO_2, iron oxide Fe_2O_3, anhydrous potassium carbonate K_2CO_3 and molybdenum (VI) oxide MoO_3 in molar ratios of 1.2 : 0.4 : 2.03 : 1.63 was put in a Pt crucible. The mixture was heated to 900 °C and kept at that temperature for 30 minutes. The temperature was increased to 1150 °C at 5 °C/min and kept at that temperature for 10 hours. Then the temperature decreased to 950 °C at a rate of 0.1 °C/min. The powder was collected after cooling in air to room temperature. Protonation of KFTO was done in 2 M HNO_3 solution at a molar ratio K^+ : H^+ of 1 : 20 for 6 days and the solution was refreshed every 2 days. Then the resultant powder was collected after washing with large quantities of water.

The time dependent experiments were made using solutions with a TBAOH/H^+ molar ratio of 4/1 for both protonated calcium niobate and protonated iron titanate. In a total volume of 20 mL solution, 0.1 g protonated calcium niobate or protonated iron titanate was used for each sample while stirring for different reaction times. Then the nanosheet concentration at the LAI was determined. The details of that procedure and the Langmuir Blodgett process can be found in the main text.

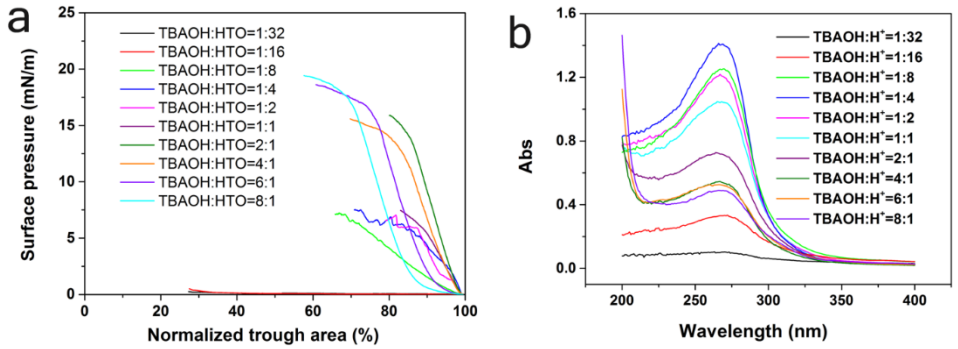

Figure S1. Pressure-area isotherm (a) and UV-Vis spectra (b) of diluted suspensions at TBAOH/H^+ molar ratios of 1:32 to 8:1.

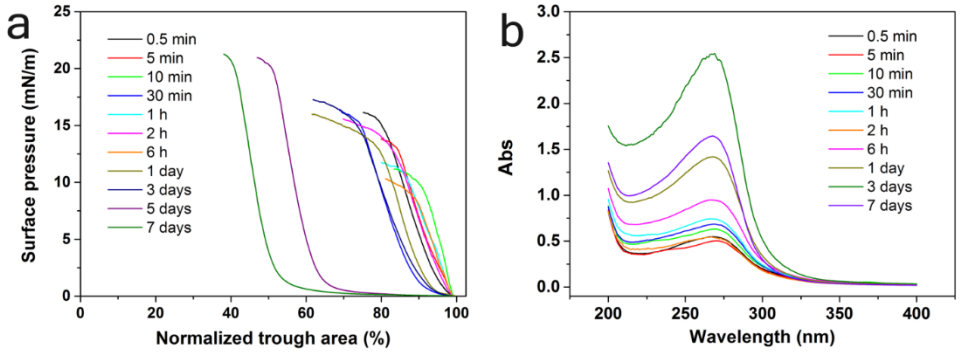

Figure S2. Pressure-area isotherm (a) and UV-Vis spectra (b) of diluted suspensions at different reaction time

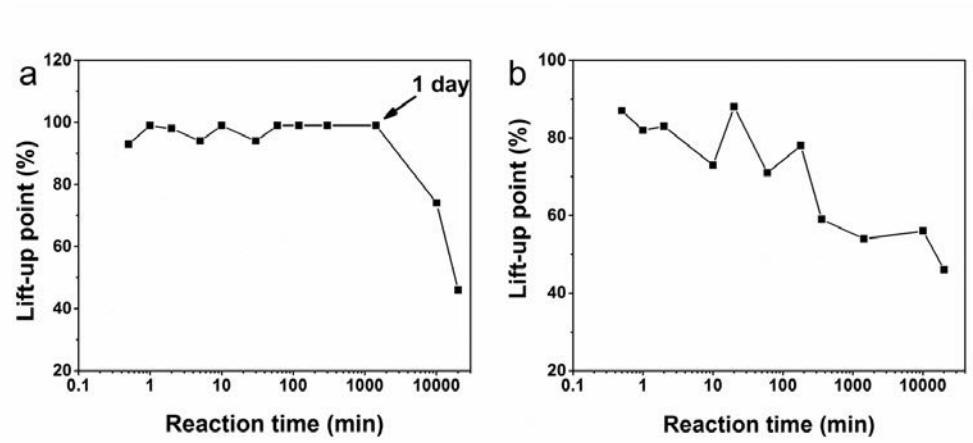

Figure S3. The lift-up point of (a) calcium niobate nanosheets and (b) iron titanate suspension at different reaction time.

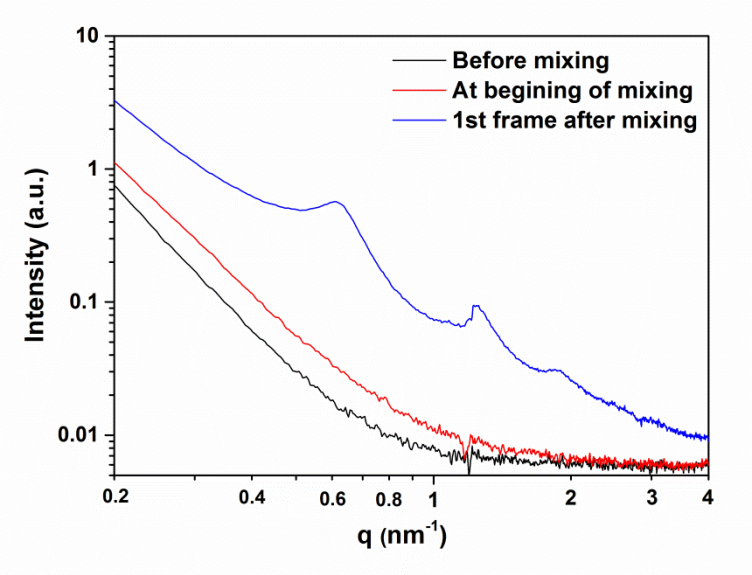

Figure S4. SAXS data from *in situ* SAXS measurements of HTO.

REFERENCES

1. Nijland, M.; Kumar, S.; Lubbers, R.; Blank, D. H. A.; Rijnders, G.; Koster, G.; ten Elshof, J. E. *ACS Appl. Mater. Interfaces* **2014**, *6*, 2777.
2. Geng, F.; Ma, R.; Ebina, Y.; Yamauchi, Y.; Miyamoto, N.; Sasaki, T. *J. Am. Chem. Soc.* **2014,** *136* (14), 5491-5500.

Chapter 4

Improved Langmuir-Blodgett titanate films via in-situ exfoliation study and optimization of deposition parameters

The exfoliation and deposition of large (10 – 100 μm) $Ti_{0.87}O_2$ and small (0.1 – 1 μm) $Ti_{0.91}O_2$ nanosheets from lepidocrocite-type protonated titanates was investigated for getting high quality films. Exfoliation was carried out with different tetra-alkyl ammonium ions (TAA^+) and varying TAA^+/H^+ ratios, and the colloidal solutions were characterized by small-angle X-ray scattering (SAXS) and ultraviolet–visible (UV-Vis) spectroscopy. Using Langmuir-Blodgett deposition the titanate nanosheets were directly transferred onto a Si substrate. The resulting films were characterized by atomic force microscopy (AFM).The results indicate that the $H_{1.07}Ti_{1.73}O_4$ titanate exfoliated at very low ratios of TAA^+/H^+; no lower threshold for exfoliation was observed for the TAA^+ concentration. Nanosheets exfoliated at very low ratios of TAA^+/H^+ typically showed a small size and porous surface. Subsequent exfoliation of the remaining layered titanate particles yielded much higher quality nanosheets. The optimized deposition parameters for Langmuir-Blodgett films suggest that the surface pressure is a key parameter to control the coverage of the film. The bulk concentration of nanosheets was found to be a less important deposition parameter in the LB deposition process. It only influenced whether the desired surface pressure could be reached at a given maximum degree of compression.

*This chapter has been published in *ACS Appl. Mater. Interfaces* **6**, 8567 (2014).

4.1 INTRODUCTION

Two-dimensional (2D) materials such as graphene are attracting much attention because of their interesting properties, which are quite distinct from three-dimensional materials.[1-7] Among the 2D materials graphene is the most thoroughly studied one.[2] However, besides graphene a large number of other 2D materials exists, which are prepared from three-dimensional precursor crystals that have strong covalent or ionic in-plane bonds and weak out-of-plane Van der Waals bonds.[8-10] Those 2D materials are a source of novel advanced materials and they may offer a huge opportunity to design new or downscaled functionalities.[10,11] In particular, due to their 2D nature and semiconducting characteristics, oxide nanosheets are regarded as a promising new channel material in field effect transistors and molecular electronics, e.g. titania.[11] Titania nanosheets have been studied intensively in recent years.[12-16] They are commonly derived from $H_{0.7}Ti_{1.825}O_4$ (denoted further as HTO-1) or $H_{1.07}Ti_{1.73}O_4$ (denoted further as HTO-2) by means of a so-called exfoliation or delamination process.[14,15] Essentially, protonated layered titanates are mixed with tetraalkylammonium hydroxides (TAAOH) in aqueous solution, and the layered oxides are exfoliated via spontaneous intercalation of tetraalkylammonium ions (TAA^+) into the adjacent layers via ion exchange with protons.[15,17] This technique gives large quantities of dispersed nanosheets and may be a promising method to make novel types of 2D nano-objects that can be incorporated into functional thin films and composites.[18,19] The $Ti_{0.91}O_2$ and $Ti_{0.87}O_2$ nanosheets exfoliated from HTO-1 and HTO-2, respectively, have largely different lateral sizes. The lateral sizes of the $Ti_{0.87}O_2$ nanosheets ranged from 10 to 100 μm,[15] and are 2 orders of magnitude larger than the sizes of $Ti_{0.91}O_2$ nanosheets, which ranged from 0.1 to 1 μm.[20] The difference is mainly due to the fact that $K_{0.80}Ti_{1.73}Li_{0.27}O_4$ (denoted further as KLTO), the parent compound for HTO-2 and ultimately $Ti_{0.87}O_2$, was prepared in a liquid flux, while $Cs_{0.7}Ti_{1.825}O_4$ (denoted further as CTO), the parent compound for HTO-1 and $Ti_{0.91}O_2$, was made by conventional solid state reaction.

Sasaki *et al.* studied the exfoliation of HTO-1 by means of X-ray diffraction and UV-visible light absorption spectroscopy.[14] They concluded that a molar ratio TBA^+/H^+ (where H^+ refers to the protons in the protonated titanate, in this case in $H_{0.7}Ti_{1.825}O_4$) of approximately 0.3-0.5 presented a threshold for exfoliation, below which only the usual intercalation reaction occurred. They also studied restacking of

exfoliated titanates and found that drying of the colloids brings about spontaneous reassembly of the nanosheets into layered hybrid materials.[21] We studied the exfoliation and restacking of layered titanates in solution and found that the restacking of titania nanosheets is controlled by electrostatic interactions due to the presence of a diffuse double layer of positively charged ions between negatively charged nanosheets. The interlayer spacing is controlled by the double layer thickness.[16] Recently, Maluangnont *et al.* studied the difference between exfoliation and restacking of protonated layered titanates (HTO-2) by tetramethylammonium hydroxide (TMAOH) and tetrabutylammonium hydroxide (TBAOH) with a molar ratio $TAA^+/H^+ > 0.5$, and found that the lateral size of the nanosheets could be controlled, depending on the type of cation, by the TAA^+/H^+ molar ratio, and the mode of the exfoliation process (manual versus mechanical shaking).[22] So the colloidal state of nanosheets exfoliated in solution is very sensitive to its chemical environment. *In situ* measurements would therefore offer a better way to study the exfoliation of nanosheets.

Langmuir-Blodgett (LB) deposition has been shown a useful technique to transfer oxide nanosheets from the liquid phase to a solid substrate and form dense monolayer films.[23-28] It is widely applicable to hydrophilic substrates such as quartz, silicon, indium-tin oxide (ITO) and glass, but also to hydrophobic Au.[27] Highly ordered nanosheet thin films have been obtained by controlling the LB deposition process.[23,28] However, LB deposition has not been used to study the influence of parameters like the nature of TAA^+ and the molar ratio TAA^+/H^+ on exfoliation. Although efforts have been made to study the effect of LB deposition parameters such as surface pressure and suspension concentration on the formation of nanosheet monolayers,[27] little work was systematically focusing on the relationship between those parameters and the morphology and coverage of monolayer nanosheet films.

In the present paper we chose HTO-2 as a model compound to study the influence of the molecular size of TAA^+ and the ratio TAA^+/H^+ on the exfoliation process, because of the big $Ti_{0.87}O_2$ nanosheets it provides. By using LB deposition and Atomic Force Microscopy (AFM) the exfoliated nanosheets from solution could be visualized directly. We employed $Ti_{0.91}O_2$ and $Ti_{0.87}O_2$ nanosheets to study the relationship between the main LB deposition parameters, namely surface pressure and nanosheet bulk concentration, on the density and structure of the resulting

monolayer film on silicon substrates. Our goal is to understand and control the process of formation of reproducible high quality nanosheet monolayers and multilayer films with coverage close to 100%.

4.2 EXPERIMENTAL SECTION

Materials. Titanium (IV) dioxide TiO_2 (Ridel-de Haen), molybdenum (VI) oxide MoO_3 (Sigma-Aldrich), anhydrous potassium carbonate K_2CO_3 (Fluka), lithium carbonate Li_2CO_3 (Ridel-de Haen), cesium carbonate Cs_2CO_3 (Sigma-Aldrich) had a purity of 99.0% or higher and were used as received. Tetra *n*-methylammonium hydroxide pentahydrate TMAOH (97%, Acros Organics), tetra *n*-ethylammonium hydroxide TEAOH (35% wt. in H_2O, Sigma-Aldrich), tetra *n*-propylammonium hydroxide TPAOH (1.0 M in H_2O, Sigma-Aldrich), and tetra *n*-butylammonium hydroxide TBAOH (40% wt. H_2O, Alfa Aesar) were used as received. Demineralized water was used throughout the experiments.

Preparation of Lepidocrocite-type protonated Layered Titanates. The CTO precursor was prepared according to the solid state synthesis procedure described elsewhere.[29] In a typical synthesis procedure, a mixture of Cs_2CO_3 and TiO_2 in 1:5.3 molar ratio was heated to 800°C and kept for 20 h. The resulting CTO powder was dispersed in 2 mol/L HNO_3 to exchange Cs^+ ions by H_3O^+ ions. Protonation was conducted for 3 days by refreshing the acidic solution every day. Then the resulting powder was washed with water to remove residual acid, filtered and dried in air to obtain crystals of HTO-1.

The KLTO precursor was obtained with a flux method developed by Tanaka *et al*.[15] TiO_2, K_2CO_3, Li_2CO_3, and MoO_3 (1.73:1.67:0.13:1.27 molar ratio) were heated to 1150°C, held at that temperature for 30 min, and then slowly cooled down to 950 °C at a speed of 4 °C/h. The oven was then allowed to cool to room temperature by natural cooling. The resulting KLTO powder was washed 3 times in 250 mL water to remove K_2MoO_4. Then KLTO powder was dispersed in a 2 mol/L HNO_3 solution (250 mL) at room temperature while stirring. The acidic solution was replaced daily by a fresh one by decantation. After treatment for 3 days, the acid-exchanged crystals were collected by filtration and washed with a copious quantity of pure water, then air dried to get HTO-2 powder.

Preparation of TAA^+-titanate solutions. For UV-visible absorption and Small Angle X-ray Scattering (SAXS) experiments, samples were made by mixing 0.5 g of HTO-2 with water and TMAOH, TEAOH, TPAOH or TBAOH, respectively, with a TAA^+/H^+ (HTO-2) molar ratio of 1:32, 1:16, 1:8, 1:4, 1:2 or 1:1 to a total volume of 100 mL solution. The fixed mixing sequence was HTO-2, water and then TAAOH. The mixtures were mechanically shaken (60 rpm) for 7 days. Then the solutions were kept standing for 3 days after which the suspensions were collected. In order to avoid breaking the nanosheets,[22] surfactant devoid solutions for LB deposition were prepared separately with the same procedure but on a shaking plate at a rate of 30 rpm in a soft way. The colloidal suspensions from HTO-1 and HTO-2 for LB deposition study were mixed with TBAOH on a shaking plate with a frequency of 30 rpm for 7 days. The molar ratio of TBA^+/H^+ (where H^+ refers to $H_{0.7}Ti_{1.825}O_4$ or $H_{1.07}Ti_{1.73}O_4$) was kept constant at 1. After 7 days the resulting suspensions were kept standing for 1 day, and then the suspensions were used for LB deposition.

Langmuir–Blodgett deposition. The deposition suspensions were prepared from stock suspensions of the solution. A defined quantity of stock solution was diluted 20 times by volume to obtain a deposition suspension. The diluted suspensions were then left standing for one day. For LB deposition, 50 mL was separated from the middle/top part of the nanosheet suspension by using a syringe. The separated suspension was poured into a Langmuir Blodgett trough (KSV Minimicro, a Teflon trough with an active trough surface area of 100 cm^2, L195 x W51 x D4 mm^3 and a dipping well L10 x W28 x D28 mm^3, trough volume 48 cm^3) and left for 15 min to equilibrate and stabilize the surface pressure before the deposition process was started. Generally a film was deposited at a surface pressure of 10 mN/m unless otherwise stated. The trough was cleaned prior to every experiment with ethanol and a soft brush, rinsed several times with distilled water to remove ethanol and then blown dry with nitrogen.

The silicon substrate was first cleaned with a CO_2 snow jet to remove dust particles and adsorbates. Then, it was cleaned in a Harrick Plasma PDC-002 oxygen plasma cleaner (25 W) for 5 min to oxidize any residual organic residues on the substrate surface. Subsequently, the silicon substrate was immersed vertically into

the suspension. The surface pressure was measured using a Wilhelmy plate attached to the KSV Minimicro frame.

Characterization. UV-Vis spectra for samples were recorded with a Cary 50 UV-Vis spectrophotometer in transmission mode. The original suspensions were diluted 333 times by volume to obtain an appropriate range of absorbances. SAXS experiments were carried out using synchrotron radiation on the Dutch-Belgian beamline, DUBBLE BM-26B of the European Synchrotron Radiation Facility (ESRF) in Grenoble.[30] The colloidal samples were placed in capillary glass tubes (Hilgenberg no. 14, dimensions: 80 mm length; 1.5 mm diameter; wall thickness ~10 μm).[16] Tapping mode Atomic Force Microscopy (AFM; Veeco Dimension Icon) was used to determine the height profile of nanosheets deposited on Si wafers. The AFM data were further analyzed using the Gwyddion (version 2.31) software package. The coverage of the substrate by nanosheets was determined using ImageJ software. The analysis was based on manually set thresholds for contrast and brightness. The coverage can be calculated from the color difference between substrate and areas occupied area by nanosheets. Details can be found in the appendices.

4.3 RESULTS AND DISCUSSION

4.3.1 Influence of molecular size of TAA^+ and molar ratio TAA^+/H^+ on exfoliation

Figure 1 shows the optical absorption spectra of colloidal suspensions at different TAA^+/H^+ (HTO-2) molar ratios. The absorption peak is located at a wavelength of 265 nm, which was blue-shifted in comparison to the absorption peak of bulk anatase TiO_2 and HTO-1.[14,23,28,31] This phenomena indicates the effect of 2D quantum confinement due to the nanosized dimensions of the nanosheets in one direction. According to the Lambert-Beer law, the absorbance should increase linearly with the concentration of nanosized titanates in the suspensions. For the samples with low molar ratios of 1:32 and 1:16, the absorbance appeared to depend more on the nature of the quaternary ammonium ion than on its concentration. The results show that as the size of TAA^+ increases the peak absorbance increases. For the sake of clarity, the peak absorbances are plotted in figure 2.

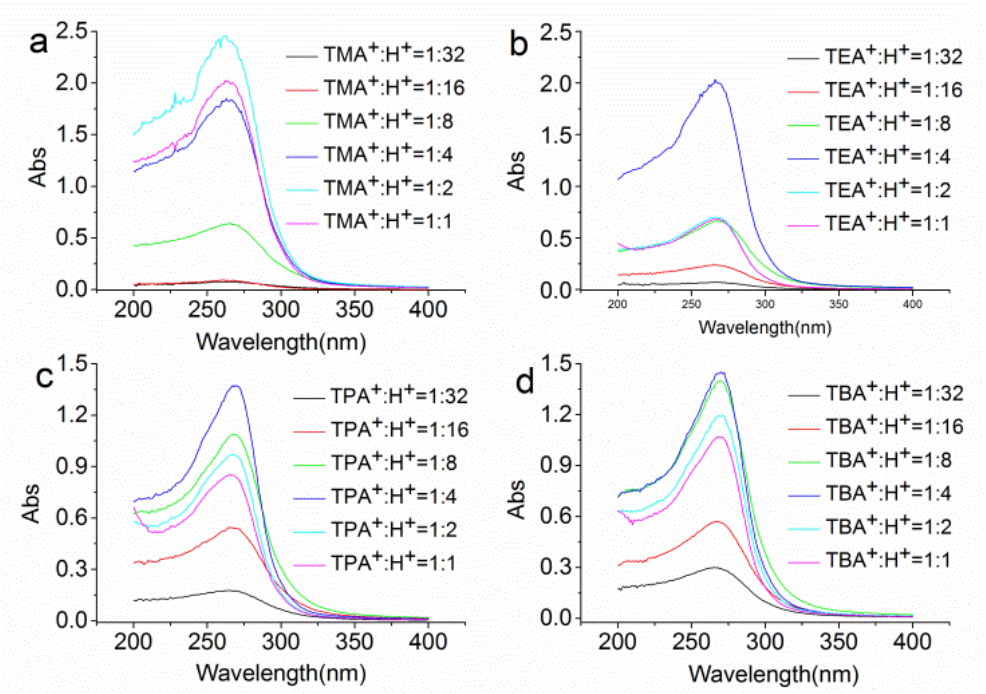

Figure 1. UV-visible spectra of diluted HTO-2 suspensions at different TAA^+/H^+ molar ratios.

Care should be taken to compare absolute values between different TAAOH suspensions with similar TAA^+/H^+ ratio. However, trends with varying TAA^+/H^+ ratio can be compared directly for a given type of TAAOH. For TMAOH and TEAOH a considerable concentration of nanosized titanates was only obtained at a molar ratio above 1:16. For TPAOH and TBAOH the ratio of 1:32 led already to a substantial concentration of nanosheets. Furthermore, except for the TMA^+ based suspension, the maximum absorbance of other suspensions with larger TAA^+ ions was observed with a TAA^+/H^+ molar ratio of 1:4. At molar ratios above 1:4 the intensity was lower, which probably means that some restacking of nanosheets occurred. It is noteworthy that HTO-2 behaved differently from HTO-1, which did not show any restacking at TBA^+/H^+ molar ratios between 0.1 and 1.[14] This may be due to the small size of HTO-1 derived nanosheets, which may decrease the chance that nanosheets coagulate. Meanwhile, suspensions with a molar ratio 1:1 showed a

small absorption increase near 200 nm wavelength, but suspensions with a molar ratio 1:2 did not. This feature is an indication of free hydroxide ions in the suspensions.[32,33] The reason for the presence of this absorption peak at a TAA^+/H^+ molar ratio of 1:1 is the proton deficient nature of HTO-2.[34] Finally, it is noted that TMAOH behaved somewhat differently than the others. For TMAOH the highest absorption was observed at a TMA^+/H^+ molar ratio of 1:2, the other TAA^+ ions showed maxima at around 1:4. The trend may be related to the variation in TAA^+ size.

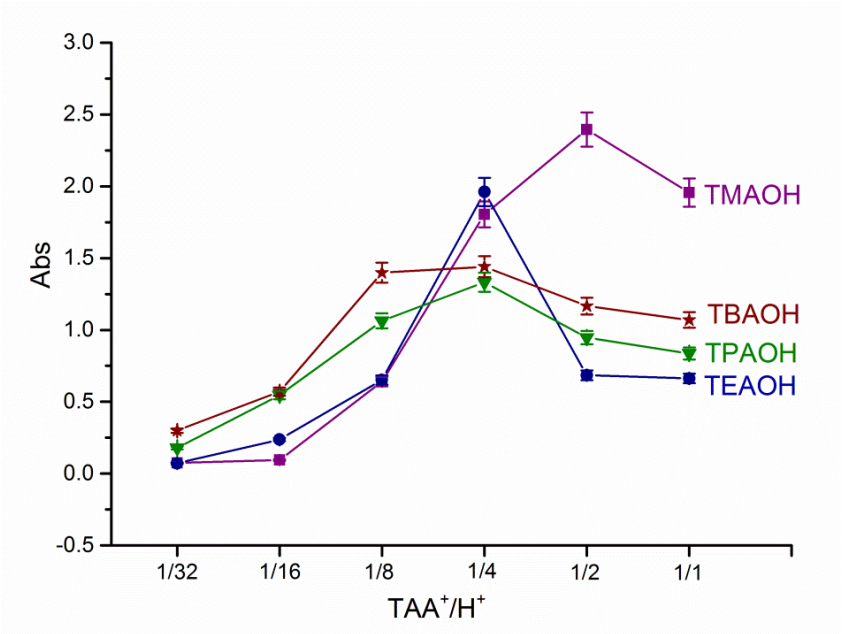

Figure 2. Absorbance of diluted suspensions at TAA^+/H^+ (HTO-2) molar ratios of 1:32 to 1:1.

Hence, the UV-visible absorption spectra confirmed the presence of nanosized particles in the suspensions at low TAA^+/H^+ molar ratio. In order to investigate the structure of these nanosized particles, SAXS experiments were performed on colloidal suspensions. The results are shown in Figure 3.

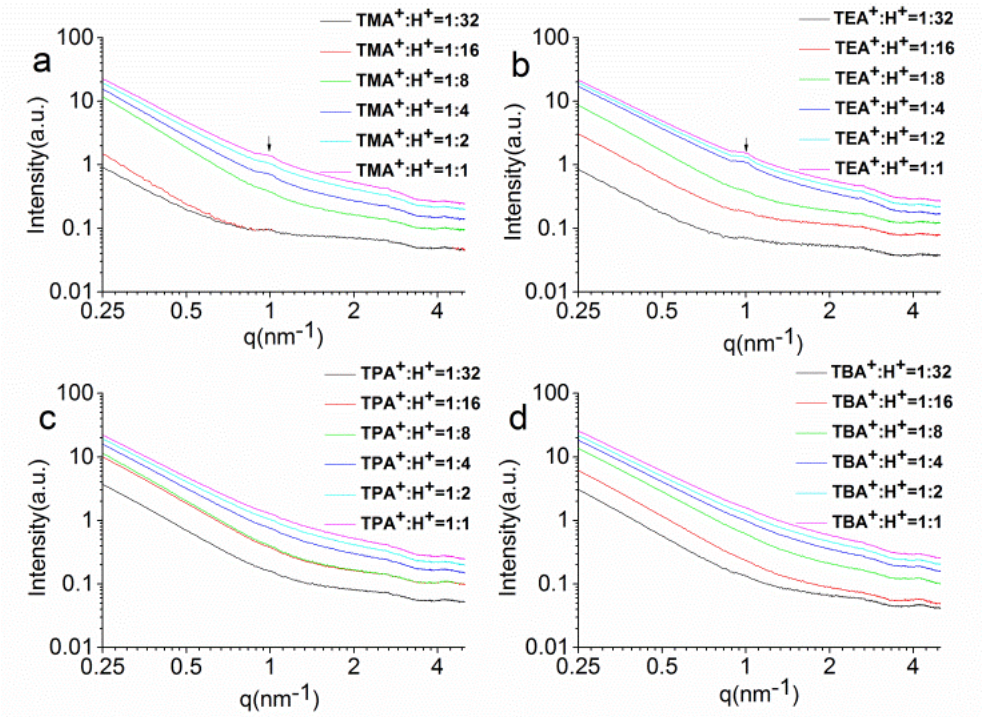

Figure 3. SAXS profiles for the colloidal HTO-2 suspensions at different TAA^+/H^+ ratio.

The SAXS curves from the TMA^+-titanate system and the TEA^+-titanate system showed a small correlation peak at q = 1.0 nm^{-1} at TAA^+/H^+ molar ratios higher than 1:4. This indicates that a low concentration of layered structures was present in these suspensions. The absence of similar pseudo-Bragg peaks in the SAXS data of the TPA^+-titanate and the TBA^+-titanate system indicated that the nanosized titanates in these colloidal suspensions were not layered but were present only as isolated sheets. It is noteworthy that restacking occurred at TAA^+/H^+ molar ratios above 1:4 irrespective of the nature of TAA^+ (See Appendices File, figure S2). This observation is in agreement with the reduction of absorbance in the UV-visible data at high TAA^+/H^+ ratio. However, only the TMA^+-titanate system and the TEA^+-titanate system showed a correlation peak at q = 1.0 nm^{-1} after sedimentation for 3 days. This result indicates that the TMA^+-titanate system and the TEA^+-titanate system tend to restack but disperse stably without precipitation at high concentration after an extended period of time (3 days). In contrast, these systems do not remain

stable and agglomerate at low concentration within a short time period (24 h), based on our experimental observation in LB deposition as described below.

We attempted to make Langmuir–Blodgett films of nanosheets from these suspensions by using different TAA^+-titanate suspensions with TAA^+/H^+ of 1:4. The stock suspensions with a TAA^+/H^+ molar ratio of 1:4 were diluted 20 times by volume. Unfortunately, the TMAOH and TEAOH based suspensions aggregated after one day standing, and the concentration appeared to be insufficient to make a good LB film. The maximum surface pressure that could be obtained after 60% compression for TMAOH and TEAOH based suspensions was less than 2 mN/m. However, isolated nanosheets were found on the substrate (see Figure 4a, b). On the other hand, good quality films were obtained from TPAOH and TBAOH based suspensions (see Figure 4c, d). The nanosheets revealed by AFM were ~1.2 nm thick, which corresponds well with values of titanate nanosheets reported elsewhere.[15,20]

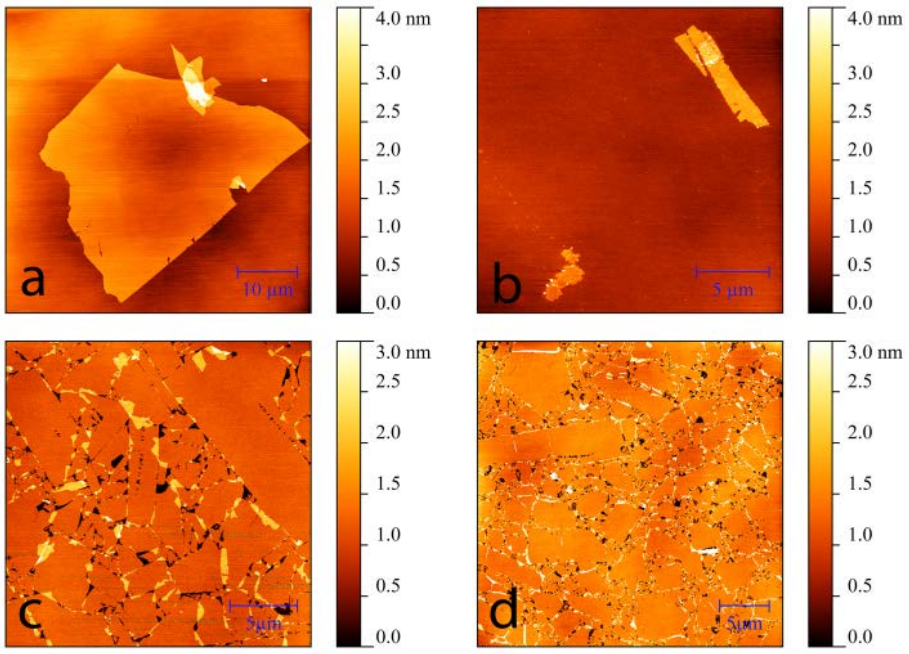

Figure 4. AFM images of LB deposited HTO-2 derived nanosheet films obtained by different types of TAAOH at constant TAA^+/H^+ ratio of 1:4. a) TMA^+/H^+; b) TEA^+/H^+; c) TPA^+/H^+; d) TBA^+/H^+.

Based on the UV-visible spectra of the TBA^+/H^+ (HTO-2) system shown in Figure 1d, the concentration of isolated nanosheets at a TBA^+/H^+ ratio of 1:16 was significantly high. A LB deposition process was therefore performed using an HTO-2 suspension with a TBA^+/H^+ ratio of 1:16. The corresponding AFM image can be found in Figure 5a, b. The AFM results confirm the presence of pores within the nanosheets. In addition, many agglomerated nanoparticles were present. It is worth to note that a large amount of unreacted HTO powder was found on the bottom of the reaction bottle. After removal of the exfoliated nanosheet suspension, further exfoliation and LB deposition was conducted using these unreacted HTO particles. The corresponding AFM images of nanosheets from the second exfoliation process can be found in Figure 5c, d. It can be seen that the average size of the nanosheets in this film is much larger than in Figure 5a. Moreover, porosity was absent in these nanosheets. So although exfoliation of titanate nanosheets occurred at very low TAA^+/H^+ ratio, yielding sufficiently high concentrations of nanosheets to allow deposition of a LB film, the quality of the initial nanosheets was much lower than that of the nanosheets from subsequent exfoliation processes.

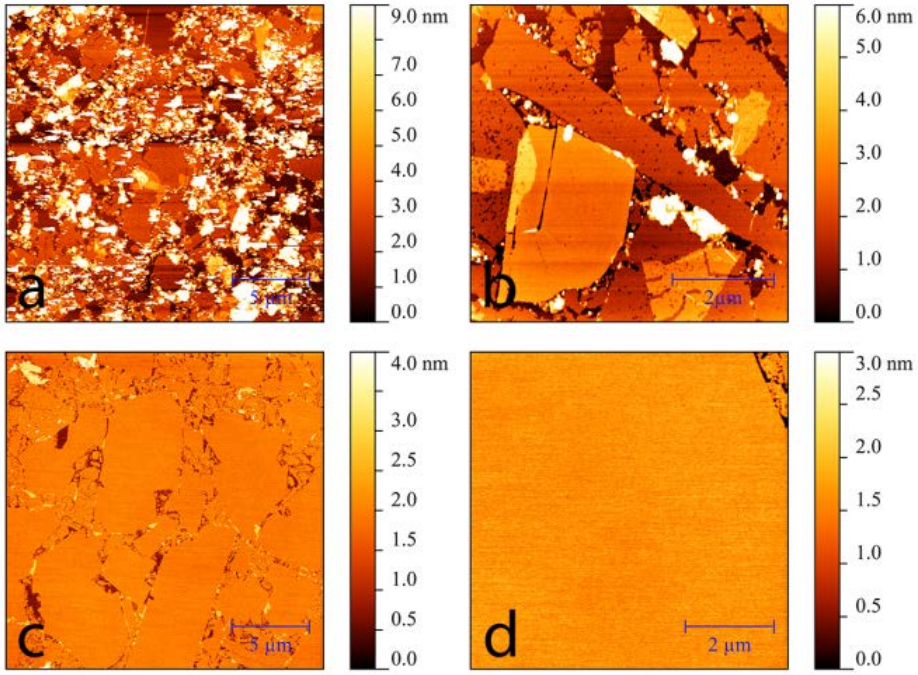

Figure 5. AFM images of LB nanosheet films obtained from a suspension with TBA^+/H^+ (HTO-2)=1:16. a) nanosheets from first exfoliation process; b) magnified image of nanosheets from first exfoliation, showing porous nanosheets; c) Nanosheets from second exfoliation process; d) magnified image of nanosheets from second exfoliation.

Steric hindrance is considered to have a key influence on the delamination rate of layered materials.[14,35] The surface of the nanosheets shown in figure 5a is very porous (see detail image in figure 5b), which means that diffusion of ions into these layered oxides, and the exchange of protons and TAA^+ was probably faster than in stacked nanosheets with more intact titanate layers. As it was previously determined the individual nanosheets in the layered protonated titanate are connected through strong hydrogen bonds.[34] It is reasonable to assume that the exfoliation only occurs after these hydrogen bonds are broken through a reaction between protons and hydroxide ions that were diffusing into HTO from the solvent matrix. For porous and small nanosheets the diffusion path for hydroxide and TAA^+ ions is shorter than with nanosheets without pores and with big nanosheets. So nanosheets with many

pores and small nanosheet stacks are expected to be exfoliated faster than those without pores and big nanosheets. Hence, small and porous nanosheets are probably most sensitive to exfoliation and can be obtained at low TAA^+/H^+ ratio, in qualitative agreement with the morphology shown in Figure 5.

4.3.2 Influence of surface pressure and nanosheet concentration on formation of monolayer nanosheet thin film

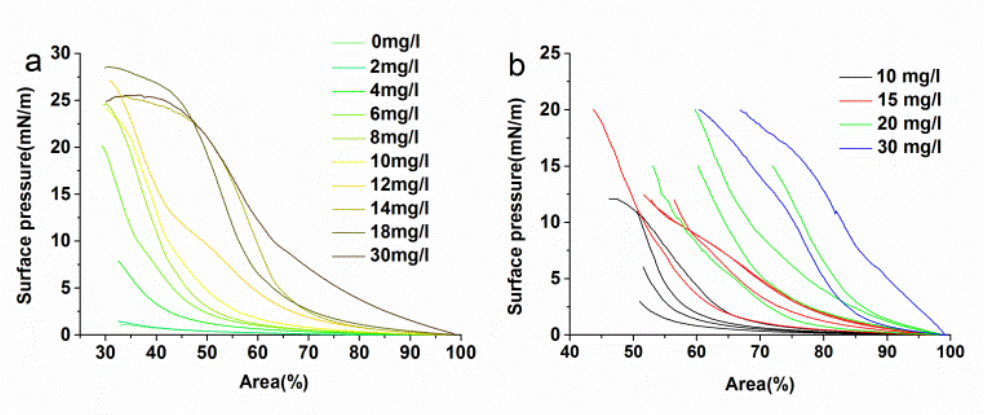

Figure 6. Surface pressure -surface area curves of (a) a $Ti_{0.91}O_2$ nanosheet suspension from HTO-1 (small sheets) and (b) a $Ti_{0.87}O_2$ nanosheet suspension from HTO-2 (large sheets).

Surface pressure – surface area compression curves of $Ti_{0.91}O_2$ and $Ti_{0.87}O_2$ nanosheet suspensions with different concentrations were made to investigate the relationship between surface pressure and bulk nanosheet concentration. See Figure 6. The numbers in figure 6 are based on the nominal 1.5 g/L HTO-1 and HTO-2 stock suspensions, which were diluted to 400 mg/L. The diluted suspension can be regarded as a pure sub-phase on which no nanosheets are present at the liquid-air surface without compression. The bulk concentration of both $Ti_{0.91}O_2$ and $Ti_{0.87}O_2$ nanosheets in the dipping solution has a clear influence on the trend in the surface pressure upon compression. Solutions with higher bulk concentrations needed less compression to achieve a certain surface pressure. For $Ti_{0.91}O_2$ nanosheets, until a bulk concentration of 6 mg/L no maximum in the surface pressure was observed upon 70% compression. At higher bulk concentrations the surface pressure appeared to saturate at values of 25-28 mN/m at 70% compression. This result agrees well with the data reported by Yamaki *et al.*, who found that a pressure of ~25 mN/m was

the saturated point of $Ti_{0.91}O_2$ nanosheets.[24] For the much larger $Ti_{0.87}O_2$ nanosheets the reproducibility was poor, as illustrated in Figure 6b where several compression curves are shown for each bulk composition. The poor reproducibility is likely related to the wide size distribution of the $Ti_{0.87}O_2$ nanosheets.

Compression-expansion experiments were conducted in a Langmuir trough to determine to what extent the LB compression process is reversible for nanosheets. Several repetitive compression and expansion cycles were conducted at several bulk concentrations. Figure 7a shows the surface pressure upon compression to 30% and subsequent expansion to 100% of a $Ti_{0.91}O_2$ suspension with a moderate bulk concentration of 12 mg/L. After every compression cycle the maximum attained surface pressure at a given degree of compression was lower than in the previous cycle, and the qualitative resemblance with a "classical" surface pressure isotherm of a diluted aqueous surfactant was lost. The same trends were also observed at all other concentrations. The decreasing maximum surface pressure after each compression cycle to 30% (Figure 7a) was likely caused by agglomeration or restacking of monolayer nanosheets. However, when the suspension was compressed to a lower maximum surface pressure (i.e. less compression), the expansion was less irreversible, as illustrated in figure 7b for a series of compression and expansion cycles. This can be explained that upon compression a rigid monolayer film formed at the air-water interface, and without enough relaxation time this monolayer is known to stay intact.[27]

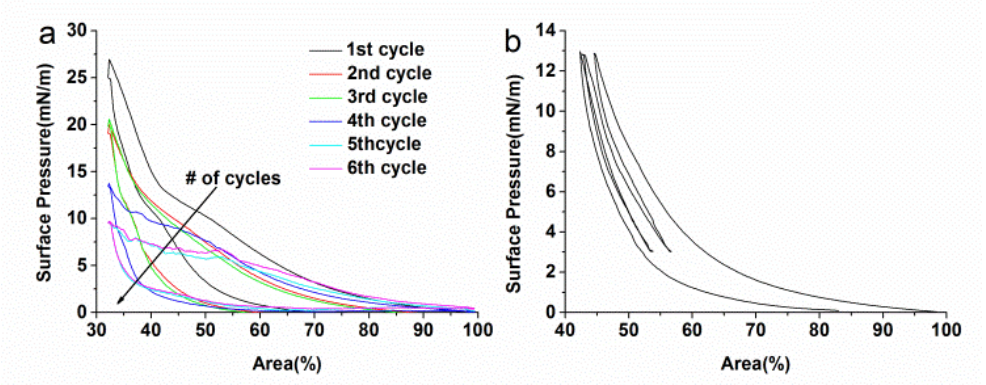

Figure 7. Surface pressure – surface area compression-expansion curves of (a) $Ti_{0.91}O_2$ (12 mg/L) nanosheet suspensions upon repetitive compression to 30% and expansion to 100%; (b) $Ti_{0.91}O_2$ (12 mg/L) nanosheet suspensions upon repetitive experiments (surface

pressure: 0→ 13→3→13→3→13→0 mN/m).

Nanosheets were transferred to silicon substrates to investigate the coverage at different nanosheet bulk concentrations and surface pressures. Figure 8a and 8b show the coverages of a silicon substrate by $Ti_{0.91}O_2$ and $Ti_{0.87}O_2$ nanosheets as a function of the nanosheet bulk concentration and surface pressure. To determine the coverages, at least 3 AFM images of almost every sample were analyzed.

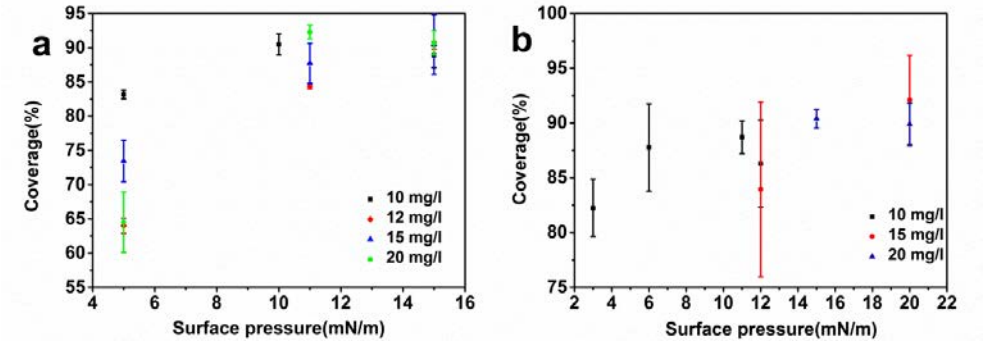

Figure 8. Coverage of substrate by nanosheets (%) versus surface pressure for (a) $Ti_{0.91}O_2$ bulk concentrations of 10-20 mg/L; (b) $Ti_{0.87}O_2$ bulk concentrations of 10-20 mg/L.

For both $Ti_{0.91}O_2$ and $Ti_{0.87}O_2$ nanosheets the coverages increased with increasing surface pressure. However, the surface roughened when a very high surface coverage was reached. Figure 9a shows a high coverage (97%) film of $Ti_{0.87}O_2$ nanosheets and Figure 9b a low coverage (63%) film of $Ti_{0.91}O_2$ nanosheets. The bright areas are indicative of nanosheet stacking and film roughening effects. However, the overlap can be trimmed to get a high coverage and well organized film.[23,28] It is noted that the nanosheets were thoroughly attached to the silicon substrate after deposition. Treatment with a CO_2 snow jet at a pressure of 25-50 bar did not result in a significant change in coverage.

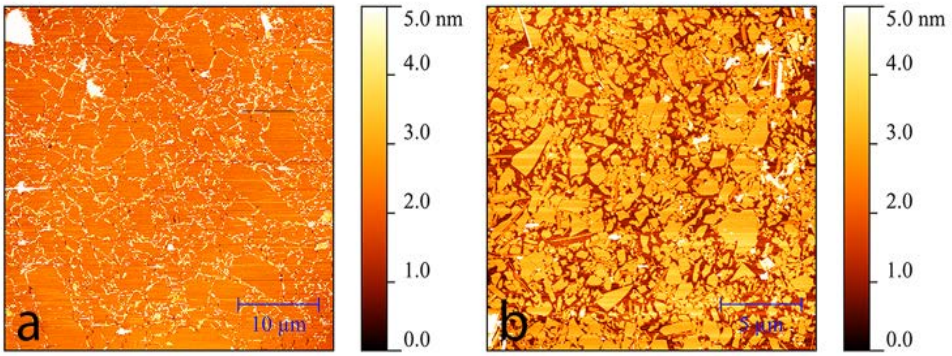

Figure 9. (a) $Ti_{0.87}O_2$ film (suspension concentration 30 mg/L, surface pressure 20 mN/m) at 97% coverage; (b) $Ti_{0.91}O_2$ film (suspension concentration 20 mg/L, surface pressure 5 mN/m) at 63% coverage.

4.4 CONCLUSIONS

The concentration of nanosized titanates formed in a suspension is related to the nature of TAAOH at low ratios of TAA^+/H^+ for HTO-2. Exfoliation occurred already at very low ratios of TAA^+/H^+; no lower threshold of exfoliation for the TAA^+ concentration was observed. Nanosheets exfoliated from an HTO suspension with a low ratio TAA^+/H^+ of 1:16 showed many pores on their surfaces, indicating that these sheets were exfoliated first. Higher quality, intact nanosheets were exfoliated at a later stage from the parent crystals. A two-step exfoliation procedure in which first the defective nanosheets are removed at low TAA^+/H^+ ratio, followed by a second separate exfoliation step in which the rest of the crystals is exfoliated aid in obtaining higher quality LB films of nanosheets. The bulk concentration of nanosheets was found to be a less important deposition parameter in the LB deposition process. It only influenced whether the desired surface pressure could be reached at a given maximum degree of compression. The higher the bulk concentration, the less compression was required to achieve a given surface pressure. By using high surface pressure the high coverage nanosheet films, >95%, were achieved. However, a too high surface pressure leads to overlap, stacking and clustering of nanosheets at the liquid surface, resulting in roughened films.

REFERENCES

1. Castro Neto, A. H.; Guinea, F.; Peres, N. M. R.; Novoselov, K. S.; Geim, A. K. *Rev. Mod. Phys.* **2009,** *81* (1), 109-162.

2. Geim, A. K.; Novoselov, K. S. *Nat. Mater.* **2007,** *6* (3), 183-191.

3. Xia, F.; Mueller, T.; Lin, Y.-m.; Valdes-Garcia, A.; Avouris, P. *Nature Nanotech.* **2009,** *4* (12), 839-843.

4. Ueno, K.; Nakamura, S.; Shimotani, H.; Ohtomo, A.; Kimura, N.; Nojima, T.; Aoki, H.; Iwasa, Y.; Kawasaki, M. *Nat. Mater.* **2008,** *7* (11), 855-858.

5. Stankovich, S.; Dikin, D. A.; Dommett, G. H. B.; Kohlhaas, K. M.; Zimney, E. J.; Stach, E. A.; Piner, R. D.; Nguyen, S. T. *Nature* **2006,** *442* (7100), 282-286.

6. Novoselov, K. S.; Geim, A. K.; Morozov, S. V.; Jiang, D.; Katsnelson, M. I.; Grigorieva, I. V.; Dubonos, S. V.; Firsov, A. A. *Nature* **2005,** *438* (7065), 197-200.

7. Novoselov, K. S.; Geim, A. K.; Morozov, S. V.; Jiang, D.; Zhang, Y.; Dubonos, S. V.; Grigorieva, I. V.; Firsov, A. A. *Science* **2004,** *306* (5696), 666-669.

8. Mas-Balleste, R.; Gomez-Navarro, C.; Gomez-Herrero, J.; Zamora, F. *Nanoscale* **2011,** *3* (1), 20-30.

9. Butler, S. Z.; Hollen, S. M.; Cao, L.; Cui, Y.; Gupta, J. A.; Gutiérrez, H. R.; Heinz, T. F.; Hong, S. S.; Huang, J.; Ismach, A. F.; Johnston-Halperin, E.; Kuno, M.; Plashnitsa, V. V.; Robinson, R. D.; Ruoff, R. S.; Salahuddin, S.; Shan, J.; Shi, L.; Spencer, M. G.; Terrones, M.; Windl, W.; Goldberger, J. E. *ACS Nano* **2013,** *7* (4), 2898-2926.

10. Geim, A. K.; Grigorieva, I. V. *Nature* **2013,** *499* (7459), 419-25.

11. Osada, M.; Sasaki, T. *J. Mater. Chem.* **2009,** *19* (17), 2503-2511.

12. Sasaki, T.; Nakano, S.; Yamauchi, S.; Watanabe, M. *Chem. Mat.* **1997,** *9* (2), 602-608.

13. Sasaki, T. *Supramol. Sci.* **1998,** *5* (3-4), 367-371.

14. Sasaki, T.; Watanabe, M. *J. Am. Chem. Soc.* **1998,** *120* (19), 4682-4689.

15. Tanaka, T.; Ebina, Y.; Takada, K.; Kurashima, K.; Sasaki, T. *Chem. Mat.* **2003,** *15* (18), 3564-3568.

16. Besselink, R.; Stawski, T. M.; Castricum, H. L.; Blank, D. H. A.; ten Elshof, J. E. *J. Phys. Chem. C* **2010,** *114* (49), 21281-21286.

17. Ma, R. Z.; Sasaki, T. *Adv. Mater.* **2010,** *22* (45), 5082-5104.

18. Coleman, J. N.; Lotya, M.; O'Neill, A.; Bergin, S. D.; King, P. J.; Khan, U.; Young, K.; Gaucher, A.; De, S.; Smith, R. J.; Shvets, I. V.; Arora, S. K.; Stanton, G.; Kim, H.-Y.; Lee, K.; Kim, G. T.; Duesberg, G. S.; Hallam, T.; Boland, J. J.; Wang, J. J.; Donegan, J. F.; Grunlan, J. C.; Moriarty, G.; Shmeliov, A.; Nicholls, R. J.; Perkins, J. M.; Grieveson, E. M.; Theuwissen, K.; McComb, D. W.; Nellist, P. D.; Nicolosi, V. *Science* **2011,** *331* (6017), 568-571.

19. Nicolosi, V.; Chhowalla, M.; Kanatzidis, M. G.; Strano, M. S.; Coleman, J. N. *Science* **2013,** *340* (6139).

20. Sasaki, T.; Ebina, Y.; Kitami, Y.; Watanabe, M.; Oikawa, T. *J. Phys. Chem. B* **2001,** *105* (26), 6116-6121.

21. Sasaki, T.; Watanabe, M.; Hashizume, H.; Yamada, H.; Nakazawa, H. *J. Am. Chem. Soc.* **1996,** *118* (35), 8329-8335.

22. Maluangnont, T.; Matsuba, K.; Geng, F.; Ma, R.; Yamauchi, Y.; Sasaki, T. *Chem. Mat.* **2013**.

23. Akatsuka, K.; Haga, M.-a.; Ebina, Y.; Osada, M.; Fukuda, K.; Sasaki, T. *ACS Nano* **2009,** *3* (5), 1097-1106.

24. Yamaki, T.; Asai, K. *Langmuir* **2001,** *17* (9), 2564-2567.

25. Yamaki, T.; Shinohara, R.; Asai, K. *Thin Solid Films* **2001,** *393* (1–2), 154-160.

26. Saruwatari, K.; Sato, H.; Kogure, T.; Wakayama, T.; Iitake, M.; Akatsuka, K.; Haga, M.; Sasaki, T.; Yamagishi, A. *Langmuir* **2006,** *22* (24), 10066-10071.

27. Muramatsu, M.; Akatsuka, K.; Ebina, Y.; Wang, K.; Sasaki, T.; Ishida, T.; Miyake, K.; Haga, M.-a. *Langmuir* **2005,** *21* (14), 6590-6595.

28. Tanaka, T.; Fukuda, K.; Ebina, Y.; Takada, K.; Sasaki, T. *Adv. Mater.* **2004,** *16* (11), 872-875.

29. Sasaki, T.; Komatsu, Y.; Fujiki, Y. *Journal of the Chemical Society, Chem. Commun.* **1991,** *0* (12), 817-818.

30. Bras, W.; Dolbnya, I. P.; Detollenaere, D.; van Tol, R.; Malfois, M.; Greaves, G. N.; Ryan, A. J.; Heeley, E. *J. Appl. Crystallogr.* **2003,** *36* (3 Part 1), 791-794.

31. Sasaki, T.; Watanabe, M. *J. Phys. Chem. B* **1997,** *101* (49), 10159-10161.

32. Pagsberg, P.; Christensen, H.; Rabani, J.; Nilsson, G.; Fenger, J.; Nielsen, S. O. *J. Phys. Chem.* **1969,** *73* (4), 1029-1038.

33. Nielsen, S. O.; Michael, B. D.; Hart, E. J. *J. Phys. Chem.* **1976,** *80* (22), 2482-2488.

34. Yuan, H.; Besselink, R.; Liao, Z.; ten Elshof, J. E. *Sci. Rep.* **2014,** *4*, 4584.

35. Liu, Z.-h.; Ooi, K.; Kanoh, H.; Tang, W.-p.; Tomida, T. *Langmuir* **2000,** *16* (9), 4154-4164.

APPENDICES

1. Substrate coverage determination

The coverage of the substrate was determined using ImageJ software. The analysis was based on a manually set contrast and brightness. The nanosheets are elevated with respect to the substrate and appeared brighter than the underlying silicon substrate. As example, Figure S1 shows a cutout from a specific AFM picture that was analyzed. The red area was calculated to be 26%. The sample therefore had a nanosheet coverage of 74%.

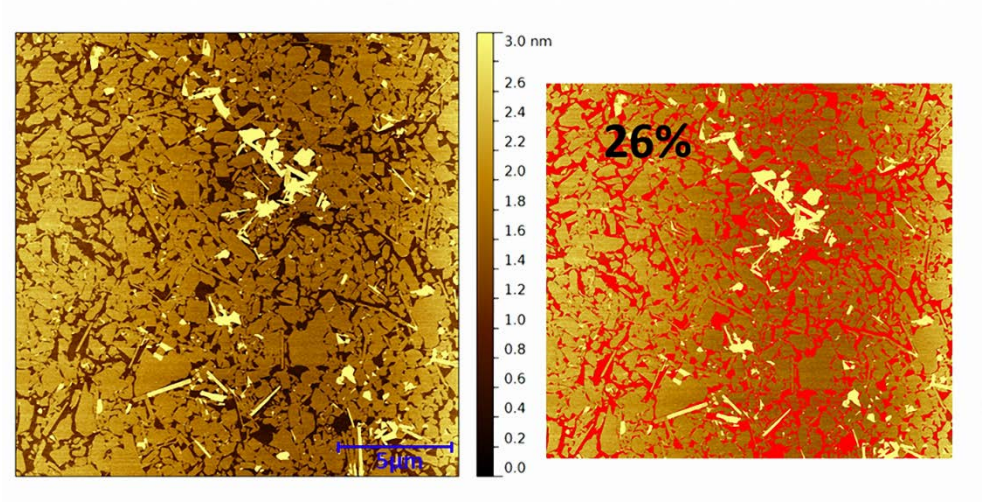

Figure S1. Determination of surface coverage using ImageJ. Example shown is a LB film on silicon from a $Ti_{0.91}O_2$ suspension with concentration of 15 mg/L, and a surface pressure of 5 mN/m.

2. SAXS curves

The colloidal HTO-2 suspensions without sediment at different TAA^+ /H^+ ratio are shown in Figure S2. The TMA+-titanate system and the TEA+-titanate system showed a correlation peak at q = 1.0 nm^{-1} at TAA^+ /H^+ ratio of 1:4 and higher. The TPA+-titanate system and the TBA^+-titanate system show the correlation peak at TAA^+ /H^+ ratio of 1:2 and higher.

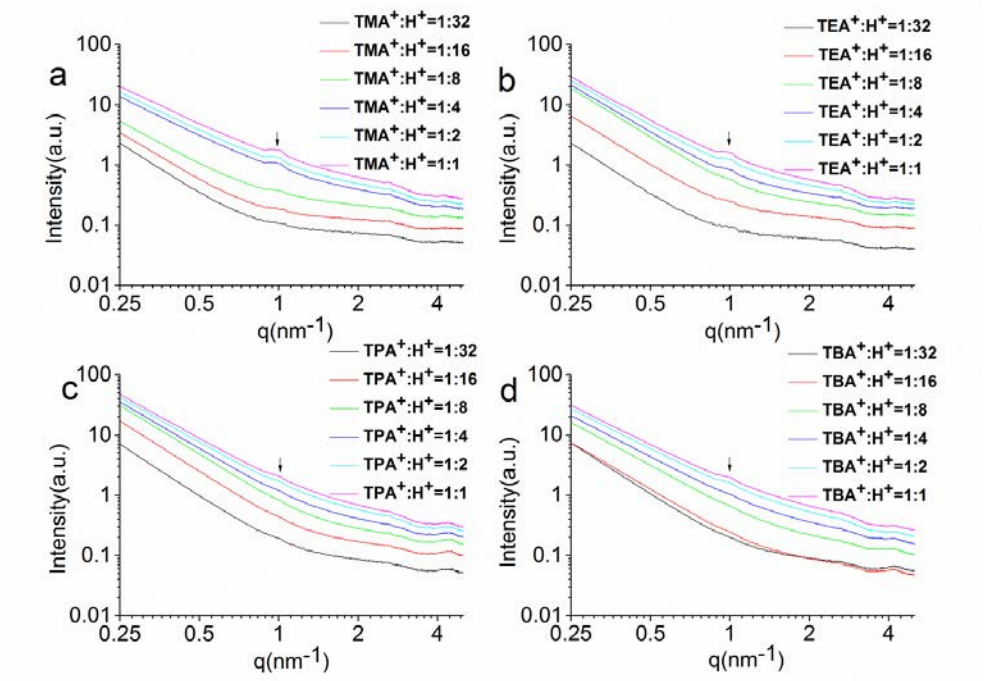

Figure S2. SAXS profiles for the colloidal HTO-2 suspensions without sedimentation at different TAA^+/H^+ ratios.

Chapter 5

Protonation and exfoliation of flux synthesized $KCa_2Nb_3O_{10}$ crystals into large 2D nanosheets as a seed layer for piezoMEMS

The layered perovskite-type niobate $KCa_2Nb_3O_{10}$ and its derivatives show advantages in several fields, such as templated film growth and (photo)catalysis. Conventional synthesis routes generally yield crystal size smaller than 2 μm. We report a flux synthesis method to obtain $KCa_2Nb_3O_{10}$ crystals with significantly larger sizes. By using different flux materials (K_2SO_4 and K_2MoO_4), crystals with average sizes of 8 and 20 μm, respectively, were obtained. The $Ca_2Nb_3O_{10}$ crystals from K_2SO_4 and K_2MoO_4 assisted synthesis were protonated and exfoliated into monolayer nanosheets, and the optimal exfoliation conditions were determined. Using pulsed laser deposition, highly (001)-oriented piezoelectric stacks ($SrRuO_3/PbZr_{0.52}Ti_{0.48}O_3/SrRuO_3$, SRO/PZT/SRO) were deposited onto Langmuir-Blodgett films of $Ca_2Nb_3O_{10}$ nanosheets with varying lateral nanosheet sizes on Si substrates. An enhanced transverse piezoelectric coefficient d_{31}, an important input parameter for the actuation of active structures in micro-electromechanical systems (MEMS) devices, was obtained for PZT films grown on CNO nanosheets with a large lateral size.

*This chapter has been published in *ACS Appl. Mater. Interfaces* **7**, 27473 (2015).

5.1 INTRODUCTION

The layered perovskite-type niobate $KCa_2Nb_3O_{10}$ (KCNO) is a Dion-Jacobson-type oxide.[1] In this niobate, the K^+ ions are sandwiched between thin quasi-2-dimensional $Ca_2Nb_3O_{10}^-$ perovskite slabs composed of corner-sharing NbO_6 octahedra and Ca^{2+} ions.[2] The potassium ions are exchangeable with protons in aqueous acidic solution to give $HCa_2Nb_3O_{10}\cdot 1.5H_2O$ (HCNO), which is a Brønsted acid.[3] These layered HCNO crystals can be exfoliated into single layers, so-called calcium niobate ($Ca_2Nb_3O_{10}^-$; CNO) nanosheets.[4-5] The CNO nanosheets and HCNO crystals have shown to present advantages in the field of templated film growth [6-10], solar cells[11], electrical applications [12], catalysis [13-16], and intercalation chemistry.[2, 17-18]

The current $KCa_2Nb_3O_{10}$ synthesis method, based on the solid state reaction, usually yields platelet-like crystals of about 2 μm in diameter, and it has been found difficult to obtain crystal sizes over 5 μm in diameter.[13] Moreover, since nanosheets easily break up into smaller fragments during or after exfoliation, the resulting CNO nanosheets usually have average lateral sizes of hundreds of nanometers only.[19-20] In the field of templated film growth, variation of crystallite size in the 2D nanosheet seed layer may affect the properties of the subsequently grown film. It is therefore essential to design a method for the formation of larger KCNO crystals. The flux synthesis method has been an appropriate method in comparable cases. For example, by using K_2MoO_4 as flux material, Tanaka *et al.* obtained potassium lithium titanate with a lateral crystallite size of over 1 mm.[21] Regarding the flux synthesis of $KCa_2Nb_3O_{10}$, Fukuoka *et al.* reported a flux synthesis by using K_2SO_4 and studied its crystal structure. However, no specific data on the crystal size, nor on the protonation or exfoliation were reported. [22] Recently, Song *et al*. showed that KCNO crystals obtained by using K_2SO_4 as flux material were much larger than crystals obtained by the conventional solid state calcination procedure, and they could be protonated and exfoliated to get larger CNO nanosheets.[23] Here, we report the synthesis of enlarged $KCa_2Nb_3O_{10}$ crystals by another flux material, i.e. K_2MoO_4. The resulting crystals were successfully protonated and exfoliated into large lateral sized monolayer nanosheets. Combining the CNO nanosheets obtained by both the conventional solid state calcination route and the use of K_2SO_4 as flux material, we were able to study the size dependent properties of these nanosheets as monolayer

nanosheet seed layers to grow functional thin films for piezo-micro-electromechanical systems (piezoMEMS).

5.2 EXPERIMENTAL SECTION

Materials. Calcium carbonate $CaCO_3$ (Sigma-Aldrich), niobium (IV) oxide Nb_2O_5 (Sigma-Aldrich), anhydrous potassium carbonate K_2CO_3 (Fluka), potassium sulfate K_2SO_4 (Sigma-Aldrich) and molybdenum (VI) oxide MoO_3 (Sigma-Aldrich) had a purity of 99.0% or higher and were used as received. Nitric acid HNO_3 (65%, ACROS Organics) and tetra n-butylammonium hydroxide TBAOH (40% wt. H_2O, Alfa Aesar) were used as received. Demineralized water was used throughout the experiments.

Flux synthesis of KCNO. The raw materials K_2CO_3, $CaCO_3$ and Nb_2O_5 were weighed in a molar ratio of 1.1:4:3, and then mixed with the flux materials K_2SO_4 or K_2MoO_4 (i.e., K_2CO_3 + MoO_3) in a flux to reactant molar ratio of 10:1. The powders were mixed on a roller bench for 1 day. After mixing, the mixture (10 g) was placed in an alumina crucible and heated to 1150°C, held at that temperature for 30 min, and then slowly cooled down to 950 °C at a speed of 4 °C/h. The oven was then allowed to cool further to room temperature by natural cooling. The resulting KCNO powders were washed 3 times in 250 mL water to remove K_2SO_4 or K_2MoO_4. The crystals obtained using K_2SO_4 and K_2MoO_4 as a flux material are further denoted as KCNO-m and KCNO-l, respectively.

Protonation and exfoliation. *Ca.* 3 g of KCNO-m or KCNO-l powder was dispersed in a 5 mol/L HNO_3 solution (250 mL) at room temperature while stirring. The acidic solution was replaced daily by a fresh one via decantation and refilling. After treatment for 3 days, the acid-exchanged crystals of KCNO-m and KCNO-l were collected by filtration and washed with a copious quantity of pure water, and then air dried to get HCNO powders (further denoted as HCNO-m and HCNO-l, respectively). The exfoliation of HCNO-m and HCNO-l crystals was carried out by reaction with a TBAOH solution. The HCNO powders (0.4 g) were mixed with TBAOH and water to a TBAOH/H^+ (H^+ refers to the protons of HCNO powder, i.e. [H^+]=[HCNO]) ratio of 1/1 in 100 ml solution. The solution was then placed on a shaking plate (shaking rate 0.5 Hz) for 7 days. Then the solution was used for UV-

vis measurements and Langmuir-Blodgett (LB) film deposition. The procedure of the LB deposition process can be found elsewhere.[24]

For sake of comparison, $KCa_2Nb_3O_{10}$ crystals were also synthesized by the conventional solid state method. The stoichiometric mixture is then heated at 1150 °C for 720 minutes with heating and cooling rates of 3 °C/min and 5 °C/min, respectively. The obtained KCNO crystals were protonated and exfoliated in same way as described above. The KCNO crystals and their resulting protonated forms are denoted as KCNO-s and HCNO-s, respectively.

Fabrication of $SrRuO_3/Pb(Zr_{0.52}Ti_{0.48})O_3/SrRuO_3$ thin films. Piezoelectric heterostructures $SrRuO_3/Pb(Zr_{0.52}Ti_{0.48})O_3/SrRuO_3$ (SRO/PZT/SRO) were grown on different laterally sized CNO-nanosheet buffered Si substrates with pulsed laser deposition (PLD), using a KrF excimer laser source (Lambda Physik, 248 nm wavelength). For the PZT film the conditions were: laser repetition rate 10 Hz, energy density 2.5 J/cm^2, oxygen pressure 0.1 mbar and substrate temperature 600 °C. In order to decrease the surface roughness of PZT thin films on nanosheets, a thin layer of $SrTiO_3$ (STO, ~10 nm) was deposited on the nanosheets and a SRO bottom electrode was then grown on STO/nanosheet/Si. The STO thin layer was deposited at a laser repetition rate of 1 Hz, energy density of 1.3 J/cm^2, oxygen pressure of 0.01 mbar and substrate temperature of 700 °C. The SRO electrodes were grown at a laser repetition rate of 4 Hz, energy density 2.5 J/cm^2, oxygen pressure 0.13 mbar and substrate temperature 600 °C. All layers were deposited successively without breaking the vacuum. After deposition, the stacked film structure was cooled down to room temperature in a 1 bar oxygen atmosphere at a rate of 6 °C/min. The thickness of the PZT and SRO films was 1 µm and 100 nm, respectively. A detailed fabrication procedure of PZT and SRO films has been described in a previous paper.[25]

Characterization. Powder X-ray diffraction (XRD) and thin film XRD data were acquired on a Bruker D2 PHASER and Panalytical X'Pert Pro (Cu Kα radiation with a wavelength of 0.15405 nm). High resolution scanning electron microscopy (HRSEM; Zeiss MERLIN) was used to acquire information on the particle size and morphology. Atomic force microscopy (AFM; Veeco Dimension Icon) was used to

determine the height profile of nanosheets deposited on Si substrates. The AFM data were further analyzed using the Gwyddion (version 2.31) software package. UV-Vis spectra of samples were recorded with a Cary 50 UV-Vis spectrophotometer in transmission mode. The original suspensions were kept standing for 1 day before measurement and were then diluted 300 times by volume to obtain an appropriate range of absorbances. For each exfoliation condition, at least 3 samples were measured. The zeta potential data were measured by a Malvern Zetasizer Nano ZS. The sample was ultrasonicated for 10 min to get a nicely dispersed solution and the pH of the samples was titrated manually with HCl aqueous solution (0.2 mol/L). The pH was measured by a Fisher Scientific Accumet Research AR15 pH meter.

For electrical measurements, 200×200 μm^2 capacitors were patterned by a standard photolithography process and structured by argon-beam etching of the top-electrodes and wet-etching (HF-HCl solution) of the PZT films. The process for fabricating piezoelectric driven Si cantilevers has been described in a previous paper.[26] Cantilever structures (length: 400 µm, width: 100 µm, Si-beam thickness: 10 µm) consisting of a piezoelectric stack (SRO/PZT/SRO) grown on a CNO-nanosheet buffered 10-µm thick Si supporting layer were obtained by backside etching of a silicon-on-insulator (SOI) wafer.

The polarization hysteresis (*P*-*E*) loop measurements were performed with the ferroelectric mode of the aixACCT TF-2000 Analyzer using a triangular *ac*-electric field of ±200 kV/cm at 1 kHz scanning frequency. A double-beam laser interferometry (aixDBLI) was used to measure the longitudinal piezoelectric coefficient (d_{33}) of the piezoelectric thin-film capacitors. The d_{33}-*E* loops were measured at an applied *dc*-electric field of ±200 kV/cm with an *ac* signal of 0.4 V and 1 kHz frequency. The transverse piezoelectric coefficient d_{31} was determined from the tip-displacement of the cantilever beam. A piezoelectric vibration was generated by applying a sinusoidal wave voltage (*ac*-amplitude of ±3 V, *dc*-offset of 3 V, and 8 kHz frequency) between the top and bottom electrodes, and the tip displacement was measured using laser Doppler vibrometry (LDV). The calculation of the d_{31} value from the tip-displacement of cantilevers can be found in ref. 27.

5.3 RESULTS AND DISCUSSION

5.3.1 Synthesis and exfoliation of layered calcium niobates

Figure 1a shows the XRD patterns of KCNO-s, KCNO-m, and KCNO-l. The patterns of flux synthesized KCNO (KCNO-m and KCNO-l) are identical to the pattern of the reference material KCNO-s. The interlayer spacing between the CNO planes in the different KCNO crystals is in the range of 1.45-1.48 nm. The HRSEM images shown in Figure 1b-d demonstrate a clear difference in particle size for the three products. Solid state synthesis yielded KCNO-s with crystal sizes less than 5 μm as shown in Figure 1b, which is consistent with literature data.[13] The K_2SO_4 and K_2MoO_4 flux assisted syntheses yielded crystal sizes up to 20 and 100 μm, respectively, which is a significant enlargement in the lateral size of KCNO crystals compared to solid state synthesis. The average crystal size of KCNO-m and KCNO-l was found to be 8 and 20 μm, respectively. The crystal size of KCNO-m is consistent with literature data. [23]

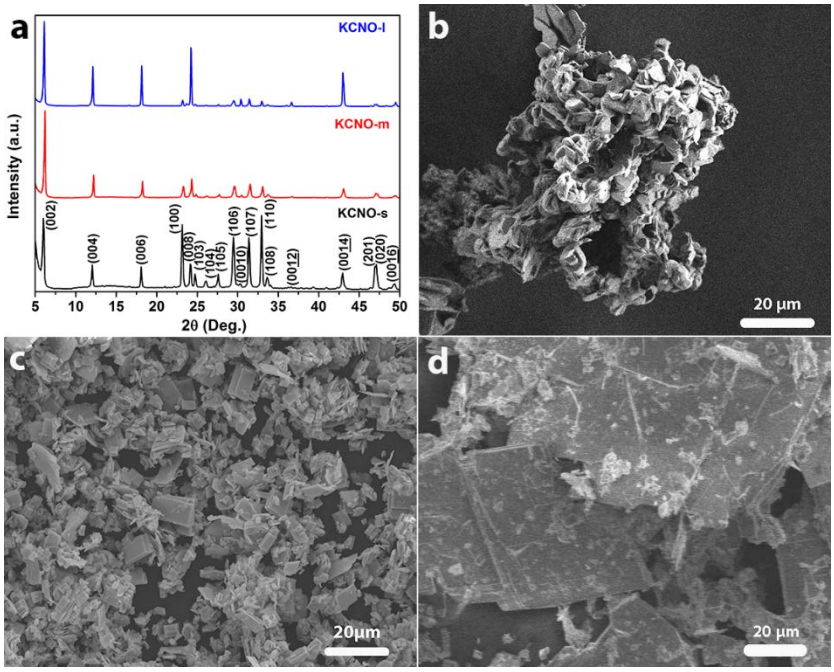

Figure 1. (a) XRD patterns of KCNO-s, KCNO-m, and KCNO-l; HRSEM images of (b) KCNO-s, (c) KCNO-m, and (d) KCNO-l.

KCNO-s and KCNO-m are known to possess an ion – exchange ability in acidic solution, which yields the protonated form HCNO-s, which is reactive to Brønsted bases.[2-3, 23] The ion – exchange ability of KCNO-l was also investigated, and the results showed that the protonated phase (See Figure 2a) is consistent with the findings of Jacobson *et al.*[3] After protonation, the interlayer spacing increased to 1.59-1.62 nm. KCNO-l was also successfully transformed into its protonated form HCNO-l, although the diffusion distances for the exchange of K^+ by H^+ are significantly larger than in KCNO-s owing to its larger lateral size. We measured the zeta potential of these 3 different forms of HCNO at varying pH. The results are shown in Figure 2b. The points of zero charge (pzc) of all three HCNO compounds are close to pH of *ca.* 2.7, indicating a similar surface chemistry for HCNO-s, HCNO-m and HCNO-l.

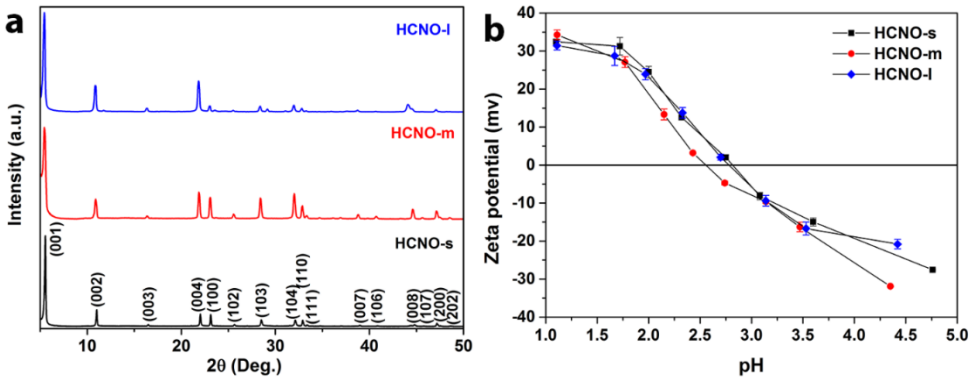

Figure 2. (a) XRD patterns of HCNO-s, HCNO-m, and HCNO-l; (b) zeta potential of HCNO-s, HCNO-m and HCNO-l versus pH.

Figure 3 shows the nanosheet monolayer films from HCNO-s, HCNO-m and HCNO-l, visualized by the AFM technique after LB deposition (Figure 3a-c). The films are further denoted as CNO-s, CNO-m and CNO-l, respectively. The thickness of CNO-s and CNO-m is *ca.* 2.3 nm and the thickness of CNO-l is *ca.* 2.8 nm as determined from AFM height profiles. The reason for the difference is not clear. The size of nanosheets from HCNO-s, HCNO-m and HCNO-l differs. The lateral size of most of CNO-s nanosheets is less than 2 μm (Figure 3a), consistent with literature data.[15, 28] In the case of CNO-m or CNO-l, more than 80% of the total surface area was covered by nanosheets with lateral sizes of more than 2 μm (Figure 3b and 3c).

CNO-m nanosheets showed larger lateral sizes of up to 6 μm (Figure 3b). Among the three types of CNO nanosheets, CNO-l presented the largest lateral sizes of up to 10 μm (Figure 3c). Our analysis showed that the average lateral size of CNO-m and CNO-l sheets with a lateral size of more than 2 μm was around 4 and 6 μm, respectively.

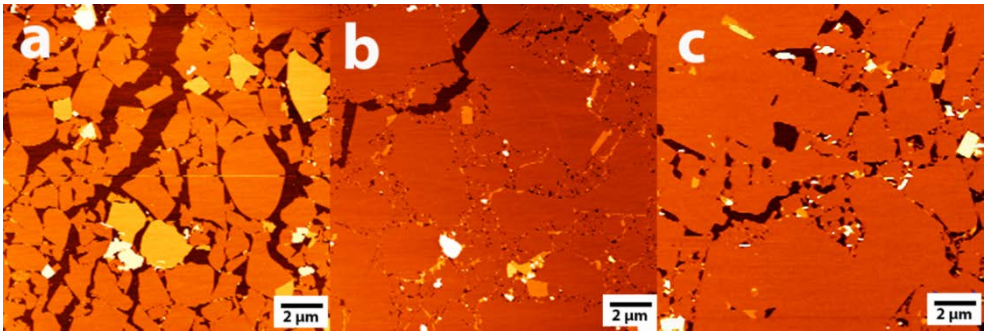

Figure 3. AFM images of exfoliated nanosheets: (a) CNO-s, (b) CNO-m, and (c) CNO-l.

The ratio of surfactant/protonated oxide crystals has a significant influence on the yield of oxide nanosheets.[24, 29] In order to optimize the exfoliation condition of HCNO, we examined the influence of the TBAOH/HCNO molar ratios on exfoliation for HCNO-s, HCNO-m and HCNO-l by means of UV-vis spectroscopy. The peak intensity of the UV-Vis spectra provides a rough indication of the nanosheet yield in solution. The results are shown in Figure 4. The absorption maximum of all three types of crystals was found to be at *ca.* 270 nm (see Figure 4a-c), which is blue shifted in comparison to the absorption peak of bulk HCNO at *ca.* 320 nm.[30] The nanosheet yield expressed in terms of peak absorbance at 270 nm at different $TBAOH/H^+$ molar ratios is plotted in Figure 4d. The absorbance of all of three types of HCNO crystals increased as the $TBAOH/H^+$ molar ratio increased from 1/32, reached a local maximum at around 2/1, and then decreased at high $TBAOH/H^+$ ratio of 4/1. The absorption increase at low $TBAOH/H^+$ molar ratios indicates that the concentration of exfoliated nanosheets increased with increasing $TBAOH/H^+$ molar ratio. The final decrease at high $TBAOH/H^+$ molar ratio suggests that the exfoliated nanosheets restacked under those conditions, thereby decreasing the photon absorption capacity.[24]

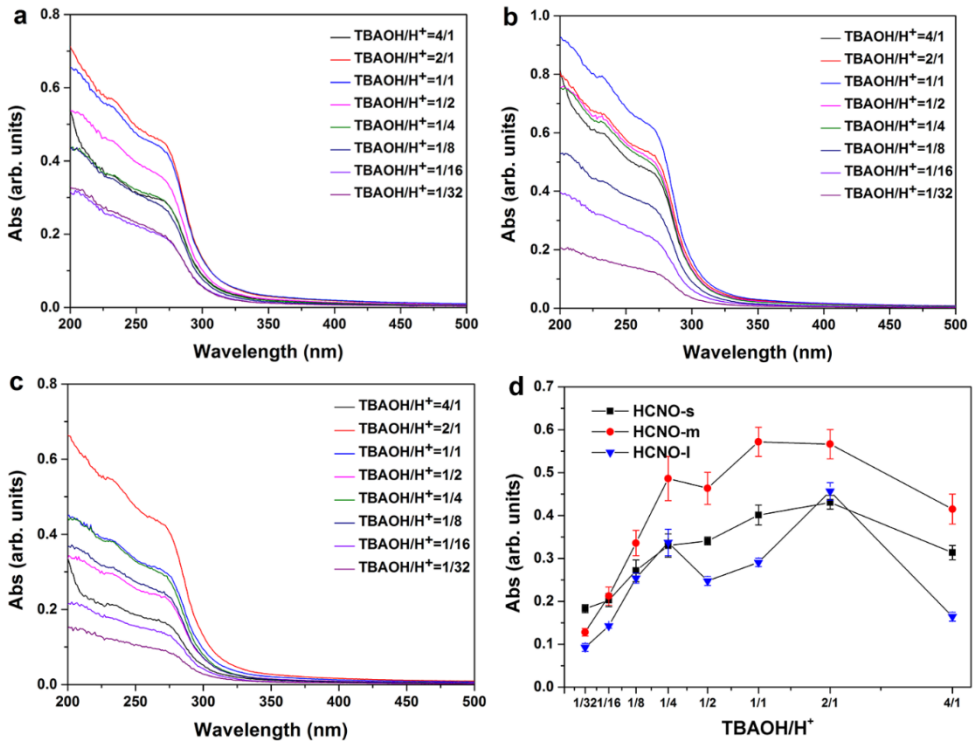

Figure 4. UV−visible spectra of diluted colloidal suspensions of (a) HCNO-s, (b) HCNO-m, and (c) HCNO-l at different TBAOH/H^+ molar ratios; (d) Absorbance at 270 nm by diluted suspensions at TBAOH/H^+ molar ratios of 1:32 to 4:1.

In Figure 4d, the absorption decreased at 1/2 and then increased again. The decrease at 1/2 most likely doesn't come from restacking of nanosheets because restacking would cause continuous decrease of absorption with increasing molar ratio of TBAOH/H^+. We ruled out the possibility that kinetics of aggregation played a role by performing reference experiments in which the colloidal solution was only kept standing for 30 min instead of 1 day, but we observed no indications for (fast) aggregation. Hence, the trends seem to be associated with the nanosheet yield only. Most likely the effect can be attributed mainly to the large pH change at TBAOH/H^+ molar ratios between 1/8 and 1/2, as shown in Figure S1. Han *et al.* observed a large chemical environment change as indicated by the zeta potential during the exfoliation of HCNO-s.[30] They found that the zeta potential decreased from *ca.* -23 mV at pH 8 to *ca.* -45 mV at pH 10, indicating the deprotonation of HCNO into

CNO^-. The data in Figure S1 show that the pH changed from *ca.* 7 at a $TBAOH/H^+$ molar ratio of 1/8 to *ca.* 11 at a TBAOH/ H^+ molar ratio of 1/2, which implies that HCNO deprotonation occurred in this pH range. After the deprotonation process, the more negatively charged nanosheets reasonably require more TBA^+ ions to stay dispersed in an exfoliated state. However, the relatively low amount of TBAOH present in solution may be limiting that process, thus leading to a lower nanosheet yield compared to the situation prior to deprotonation. Therefore, our data suggest that the exfoliation process of HCNO included two stages: the first stage at a $TBAOH/H^+$ molar ratio < 1/4, in which HCNO gradually became fully deprotonated, and a fully deprotonated stage at molar ratios $TBAOH/H^+$ between 1/4 and 2/1. Based on the discussion above, we conclude that the optimal $TBAOH/H^+$ molar ratio for complete exfoliation of HCNO is in the range of 1/1 to 2/1.

5.3.2 Function as a seed layer for piezoMEMS

The LB nanosheet films obtained from CNO-s, CNO-m and CNO-l were used as seed layers for subsequent growth of piezoelectric thin films for piezoMEMS devices on Si substrates. The coverage of nanosheet films used for further growth was more than 95%. The structure of a capacitor encompassing the piezoelectric stack (SRO/PZT/SRO) grown on a CNO nanosheet buffered Si substrate is shown in Figure 5a. Figure 5b depicts the XRD patterns of the PZT/SRO films deposited onto CNO/Si substrates (The AFM images of these films are shown in Figure S2). The PZT and SRO films have preferred (001) orientation with minor (110) orientation, which is consistent with a previous report.[6] The full-width at half maximum (FWHM) values (Table 1) defined from the rocking curves of the PZT(002) peaks (not shown here) are similar in value, indicating that the crystallinity of the PZT films is similar for films grown on CNO nanosheets of different sizes. It is noted that the sample buffered by CNO-s shows a more clearly separated peak at the SRO (002) position than the other samples do. We verified that the peak consists of two peaks from the top and bottom SRO electrodes, respectively. The larger peak separation indicates that the crystallinity difference between the top and bottom SRO electrodes grown on CNO-s is larger than for the other two systems. We believe that the reason is due to the presence of a higher concentration of grain boundaries in the CNO-s nanosheet based film than in the other films.

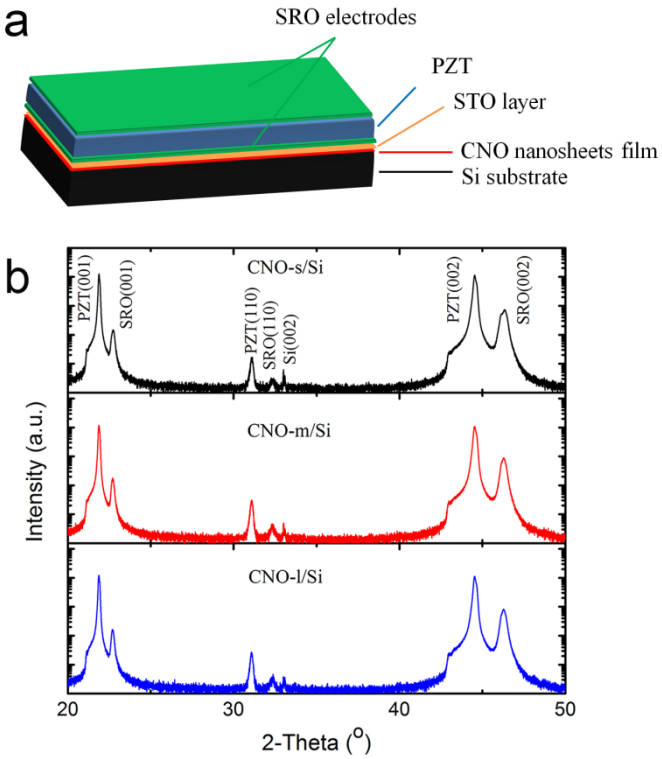

Figure 5. (a) A piezoelectric-stack capacitor structure, (b) XRD patterns of PZT films grown on CNO nanosheet/Si substrates.

Table 1. The full-width half maximum values of PZT films grown on CNO nanosheet/Si substrates.

CNO nanosheets/Si	**FWHM of PZT (002) peak**
CNO-l	0.74°
CNO-m	0.72°
CNO-s	0.75°

Figure 6a compares the *P-E* hysteresis loops for PZT films grown on CNO nanosheet/Si substrates. It shows that the remnant polarization P_r of PZT films increases slightly with increasing size of the underlying CNO nanosheets.

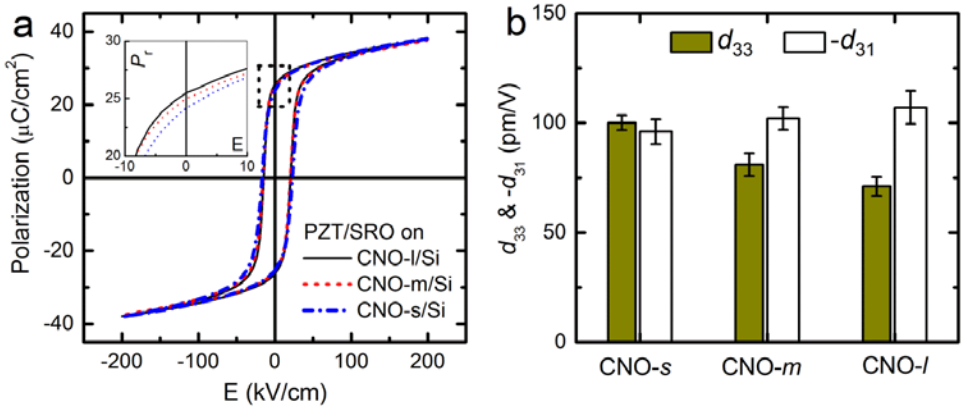

Figure 6. (a) Ferroelectric (*P-E*) hysteresis loops, and (b) longitudinal d_{33} and transverse d_{31} piezoelectric coefficients of (001)-oriented PZT/SRO films grown on CNO nanosheet buffered Si substrates with varying CNO crystallite sizes. The inset in (a) shows the zoomed *P-E* loops.

Figure 6b demonstrates the d_{33} and d_{31} values of PZT films as a function of CNO nanosheet size (See Figure S3 for the d_{33}-*E* hysteresis loops of PZT films grown on CNO nanosheet/Si substrates). The ferroelectric and piezoelectric properties are also summarized in Table S1. It indicates that larger d_{33} but smaller d_{31} values are obtained in the PZT film grown on smaller sized CNO nanosheets and vice versa.

The lower d_{31} value of the PZT film grown on smaller CNO nanosheets as compared to that of the film on larger CNO nanosheets is believed to be related to morphology differences between the different nanosheet layers. The cross sectional image in Figure S4 shows a very dense structure in the PZT film grown on CNO-s nanosheets (Figure S4a), and a clear columnar growth structure in the film at the grain boundary of the nanosheet (Figure S4b). The open columnar structure makes a large fraction of the film ineffective in contracting the film as a whole. The columns contract in width with applied electric field, but since they are not connected over most of the film thickness the film itself is much less contracted,

giving rise to much less tip deflection and therefore to a lower apparent d_{31} value of the film. The enhanced d_{31} value is obtained on larger sized CNO nanosheets due to the lower nanosheet grain boundary concentration, and/or because of the decreasing amount of columnar structure in the PZT film. Thus, by controlling the lateral dimensions of the CNO nanosheets in the seed layer, specific applications of piezoelectric PZT thin films that require either a large in-plane (d_{31}) or out-of-plane (d_{33}) piezoelectric displacement can be modulated.

5.4 CONCLUSIONS

We accomplished size-controllable synthesis of KCNO crystals under assistance of flux materials K_2SO_4 and K_2MoO_4. The K_2SO_4 and K_2MoO_4 assisted syntheses yielded average crystal sizes of 8 and 20 μm, respectively. The resulting KCNO crystals could be protonated and exfoliated into 2D nanosheets. The resulting nanosheets showed a larger lateral size compared to the hundreds of nanometers typical for nanosheets obtained from conventional solid state synthesis. The optimal exfoliation condition for HCNO was found to be a TBAOH/H^+ molar ratio between 1/1 and 2/1. Highly (001)-oriented PZT/SRO films were successfully deposited on Si substrates using CNO nanosheet films as a buffer layer. The films with larger lateral sized CNO nanosheets exhibited higher d_{31} and lower d_{33} values than films grown on nanosheets of smaller lateral size. It implies that larger CNO nanosheets can be useful for piezoMEMS devices, such as micro-actuators.

REFERENCES

1. Dion, M.; Ganne, M.; Tournoux, M. *Mater. Res. Bull.* **1981,** *16* (11), 1429-1435.

2. Jacobson, A. J.; Johnson, J. W.; Lewandowski, J. T. *Inorg. Chem.* **1985,** *24* (23), 3727-3729.

3. Jacobson, A. J.; Lewandowski, J. T.; Johnson, J. W. *J. Less Common Met.* **1986,** *116* (1), 137-146.

4. Treacy, M. M. J.; Rice, S. B.; Jacobson, A. J.; Lewandowski, J. T. *Chem. Mater.* **1990,** *2* (3), 279-286.

5. Xu, F. F.; Ebina, Y.; Bando, Y.; Sasaki, T. *J. Phys. Chem. B* **2003,** *107* (36), 9638-9645.

6. Nijland, M.; Kumar, S.; Lubbers, R.; Blank, D. H. A.; Rijnders, G.; Koster, G.; ten Elshof, J. E. *ACS Appl. Mater. Interfaces* **2014,** *6* (4), 2777-2785.

7. Naoomi, Y.; Tatsuo, S.; Kenji, T.; Yasushi, H.; Shoichiro, N.; Ngoc Lam Huong, H.; Taro, H.; Toshihiro, S.; Takayoshi, S.; Tetsuya, H. *Appl. Phys. Express* **2011,** *4* (4), 045801.

8. Tetsuka, H.; Takashima, H.; Ikegami, K.; Nanjo, H.; Ebina, T.; Mizukami, F. *Chem. Mater.* **2008,** *21* (1), 21-26.

9. Shibata, T.; Fukuda, K.; Ebina, Y.; Kogure, T.; Sasaki, T. *Adv. Mater.* **2008,** *20* (2), 231-235.

10. Taira, K.; Hirose, Y.; Nakao, S.; Yamada, N.; Kogure, T.; Shibata, T.; Sasaki, T.; Hasegawa, T. *ACS Nano* **2014,** *8* (6), 6145-6150.

11. Chang, L.; Holmes, M. A.; Waller, M.; Osterloh, F. E.; Moule, A. J. *J. Mater. Chem.* **2012,** *22* (38), 20443-20450.

12. Osada, M.; Akatsuka, K.; Ebina, Y.; Funakubo, H.; Ono, K.; Takada, K.; Sasaki, T. *ACS Nano* **2010,** *4* (9), 5225-5232.

13. Igarashi, S.; Sato, S.; Takashima, T.; Ogawa, M. *Ind. Eng. Chem. Res.* **2013,** *52* (9), 3329-3333.

14. Domen, K.; Yoshimura, J.; Sekine, T.; Tanaka, A.; Onishi, T. *Catal. Lett.* **1990,** *4* (4-6), 339-343.

15. Compton, O. C.; Carroll, E. C.; Kim, J. Y.; Larsen, D. S.; Osterloh, F. E. *J. Phys. Chem. C* **2007,** *111* (40), 14589-14592.

16. Sabio, E. M.; Chi, M. F.; Browning, N. D.; Osterloh, F. E. *Langmuir* **2010,** *26* (10), 7254-7261.

17. Gao, L.; Gao, Q.; Wang, Q.; Peng, S.; Shi, J. *Biomaterials* **2005,** *26* (26), 5267-5275.

18. Jacobson, A. J.; Lewandowski, J. T.; Johnson, J. W. *Mater. Res. Bull.* **1990,** *25* (5), 679-686.

19. Maeda, K.; Eguchi, M.; Youngblood, W. J.; Mallouk, T. E. *Chem. Mater.* **2009,** *21* (15), 3611-3617.

20. Ebina, Y.; Sasaki, T.; Watanabe, M. *Solid State Ion.* **2002,** *151* (1–4), 177-182.

21. Tanaka, T.; Ebina, Y.; Takada, K.; Kurashima, K.; Sasaki, T. *Chem. Mater.* **2003,** *15* (18), 3564-3568.

22. Fukuoka, H.; Isami, T.; Yamanaka, S. *J. Solid State Chem.* **2000,** *151* (1), 40-45.

23. Song, Y.; Iyi, N.; Hoshide, T.; Ozawa, T. C.; Ebina, Y.; Ma, R.; Miyamoto, N.; Sasaki, T. *Chem. Commun.* **2015**.

24. Yuan, H.; Lubbers, R.; Besselink, R.; Nijland, M.; ten Elshof, J. E. *ACS Appl. Mater. Interfaces* **2014,** *6* (11), 8567-8574.

25. Nguyen, M. D.; Nazeer, H.; Karakaya, K.; Pham, S. V.; Steenwelle, R.; Dekkers, M.; Abelmann, L.; Blank, D. H. A.; Rijnders, G. *J. Micromech. Microeng.* **2010,** *20* (8), 085022.

26. Nguyen, M. D.; Dekkers, M.; Vu, H. N.; Rijnders, G. *Sensor Actuat. A-Phys.* **2013,** *199*, 98-105.

27. Dekkers, M.; Boschker, H.; Zalk, M. v.; Nguyen, M.; Nazeer, H.; Houwman, E.; Rijnders, G. *J. Micromech. Microeng.* **2013,** *23* (2), 025008.

28. Schaak, R. E.; Mallouk, T. E. *Chem. Mater.* **2000,** *12* (9), 2513-2516.

29. Maluangnont, T.; Matsuba, K.; Geng, F.; Ma, R.; Yamauchi, Y.; Sasaki, T. *Chem. Mater*. **2013,** *25* (15), 3137-3146.

30. Han, Y.-S.; Park, I.; Choy, J.-H. *J. Mater. Chem.* **2001,** *11* (4), 1277-1282.

APPENDICES

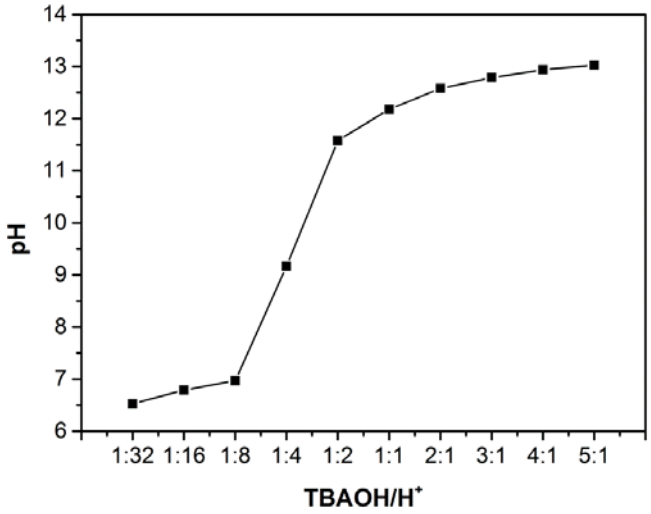

Figure S1. pH dependence on TBAOH/H^+ molar ratio for HCNO-l.

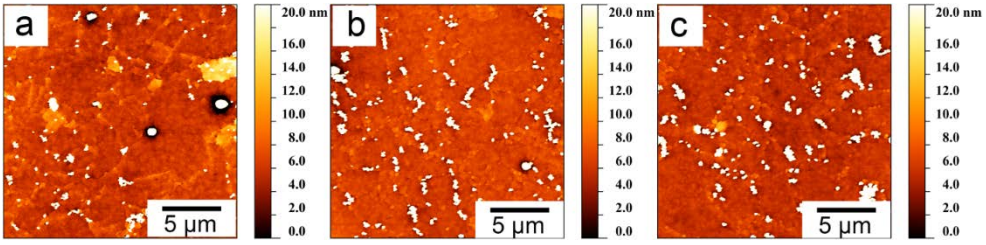

Figure S2. AFM images of (001)-oriented PZT/SRO films grown on (a) CNO-s, (b) CNO-m and (c) CNO-l, buffered Si substrates.

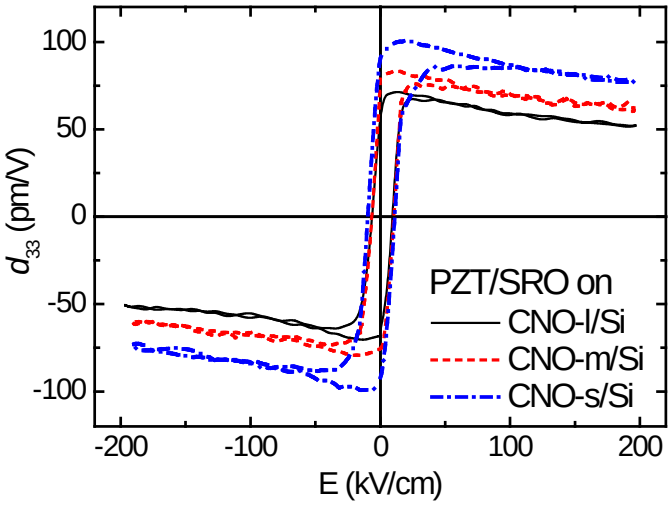

Figure S3. Piezoelectric (d_{33}-E) loops of the (001)-oriented PZT/SRO films grown on different sizes of CNO nanosheets buffered Si substrates.

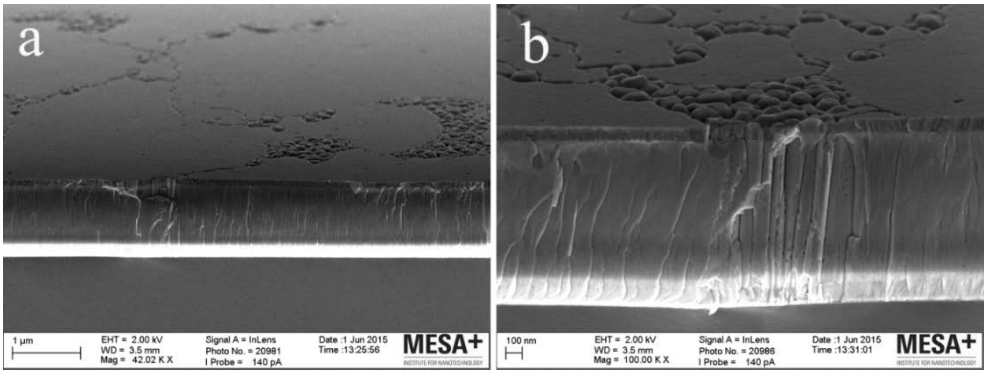

Figure S4. Cross-sectional SEM images of the PZT film grown on CNO-s/Si substrate.

Table S1. Properties of PZT films grown on different sizes of CNO nanosheets buffered Si.

	(001)PZT/SRO on CNO-*s*/Si	(001)PZT/SRO on CNO-*m*/Si	(001)PZT/SRO on CNO-*l*/Si
P_r (μC/cm^2)	24.1	24.9	25.5
d_{33} (pm/V)	100	81	72
-d_{31} (pm/V)	96	102	107

Chapter 6

Further challenges and opportunities in fabrication of metal oxide nanosheets and their Langmuir Blodgett films

Current research have already shown that the metal oxide nanosheets offer numerous opportunities for advancement of technology and could improve our life. However, there are still challenges remaining to bring the nanosheets into our daily life. These challenges leave opportunities for the community to further explore the land of 2D metal oxides.

In this thesis, a study of the exfoliation of layered metal oxides and their Langmuir Blodgett films is presented. As shown in the previous chapters, a combination of techniques such as small angle X-ray scattering (SAXS), Langmuir-Blodgett (LB) deposition, and UV-Vis spectroscopy are powerful tools to study the synthesis of metal oxide nanosheets. Based on the results, efficient exfoliation and fabrication of high quality nanosheets has been accomplished. However, some issues are worth to be mentioned here for further development of nanosheets.

6.1 FORMATION OF LB NANOSHEET FILMS

Even though the LB nanosheet films can be obtained as shown in the previous chapters, not all work is done. A problem observed with LB deposition of CNO-l nanosheets is that compared with other types of nanosheets, a higher concentration was needed to realize a dense film. A further study of the formation mechanism of LB nanosheet films would be advisable to find out the reason behind this problem.

Nanosheets obtained by ion intercalation-based exfoliation can be transferred from solution to solid substrates by LB deposition. The reason that LB deposition of nanosheets works is associated to the ability of hybridization of hydrophobic organic molecules and nanosheets.[1] So a successful LB deposition satisfies two demands, namely strong interaction between nanosheets and organic molecules, and sufficiently high hydrophobicity of organic molecules, in order to concentrate nanosheets at the liquid-air interface. The study of the interaction between nanosheets and organic molecules, evaluation of the hydrophobicity of this system and the relationship between hydrophobicity and different nanosheets would be an interesting topic for further study.

The interaction between nanosheets and organic molecules is expected to follow the predictions of the electrical double layer theory.[2] This would be a good starting point for further theoretical modelling to elucidate the influence of hydrophobicity of this hybridized system in various compositions. Such a study would also be helpful to optimize fabrication conditions of LB nanosheet films in general, and might answer the question why CNO-l is more difficult to deposit into LB films than other types of nanosheets.

6.2 STABILITY OF LB NANOSHEET FILMS IN CHEMICAL SOLUTION

Nanosheet films have already been used to control the film growth in several different thin film fabrication techniques, such as the sol-gel method and pulsed laser deposition.[3-5] In those processes, a high temperature is needed to get fully crystalline thin films. The high temperature process is not favorable for some applications, such as flexible electronics. Hydrothermal synthesis can yield crystalline thin films at relatively low temperatures.[6] In terms of orientation control, nanosheets could be a useful tool to engineer thin films at low temperature if the nanosheets would be stable under hydrothermal synthesis conditions. It would be interesting to investigate the stability of nanosheet films in various chemical solutions.

A preliminary study of the stability of monolayer titanium oxide nanosheet films at different pH and temperatures was carried out. The experimental details to prepare nanosheet films are the same as described in chapter 4. The pH tests were carried out under ambient conditions in the pH range of 1-14. The temperature tests were investigated at a pH of 5 at temperatures of 75, 100, 120 and 150 °C. The testing time for all the samples was 24 h. By using the AFM technique, it was found that the titanium oxide nanosheet films can survive at pH between 3 and 11. It is noted that the nanosheet films were stable even at a pH of 1 during a short testing time of 2 h. At a pH >11, the Si substrates were not stable, which makes those results unreliable. Even though an attempt was made to investigate the influence of temperature on nanosheet films, no solid conclusions could be drawn from AFM characterization alone. Nevertheless, the preliminary results show that nanosheet films are promising substrates for crystal engineering in combination with wet chemical synthesis routes.

6.3 CHARACTERIZATION OF MONOLAYER NANOSHEETS IN LARGE AREA

Metal oxide nanosheet thin films have already found advantages in crystal engineering for thin film growth.[7] These films can serve in a wide range of applications, for example piezoMEMS (chapter 5). In such applications, the characterization of nanosheet thin films over large areas is essential to determine the quality, which is required to enable the transfer of this technique from research to industry. AFM is a suitable technique to characterize nanosheet thin films in terms

of coverage, homogeneity and quality of sheets. However, with the current AFM technique it is difficult to scan a sample over 100 μm lateral distance, which makes it unsuitable for integral large area characterization of nanosheet thin films. An alternative technique is needed to assess LB film quality over larger surface areas is needed.

REFERENCES

1. Muramatsu, M.; Akatsuka, K.; Ebina, Y.; Wang, K.; Sasaki, T.; Ishida, T.; Miyake, K.; Haga, M.-a. *Langmuir* **2005**, *21*, 6590.

2. Besselink, R.; Stawski, T. M.; Castricum, H. L.; Blank, D. H. A.; ten Elshof, J. E. *J. Phys. Chem. C* **2010**, *114*, 21281.

3. Kikuta, K.; Noda, K.; Okumura, S.; Yamaguchi, T.; Hirano, S.-i. *J Sol-Gel Sci Technol* **2007**, *42*, 381.

4. Tetsuka, H.; Takashima, H.; Ikegami, K.; Nanjo, H.; Ebina, T.; Mizukami, F. *Chem. Mat.* **2008**, *21*, 21.

5. Shibata, T.; Fukuda, K.; Ebina, Y.; Kogure, T.; Sasaki, T. *Adv. Mater.* **2008**, *20*, 231.

6. Clark, B. L.; Keszler, D. A. *Inorg. Chem.* **2001**, *40*, 1724.

7. Nijland, M.; Kumar, S.; Lubbers, R.; Blank, D. H. A.; Rijnders, G.; Koster, G.; ten Elshof, J. E. *ACS Appl. Mater. Interfaces* **2014**, *6*, 2777.

Summary

Research on 2D materials has been booming since the experimental discovery of graphene. As one of the key enablers in 2D materials research, a mature synthesis route to form 2D materials is the way to push those new materials forward from the lab to practical applications. Insight into the exfoliation process is undoubtedly helpful to develop and establish a mature fabrication route. In this thesis, the results from exfoliation studies on layered metal oxides and the formation of their Langmuir-Blodgett (LB) films are presented. *In situ* experiments showed that the exfoliation of layered titanates follows a different mechanism from what is generally assumed in the prevalent concept (***chapter 2***). The layered titanate crystal goes directly through exfoliation under assistance of an acid-base reaction, and the as-formed 2D nanosheets rapidly restack at high molar ratios of $TBAOH/H^+$. Monolayer nanosheet LB films could be obtained from solutions which had endured less than a minute of reaction time. This finding can help to significantly reduce the fabrication time of metal oxide nanosheets and their LB films. The study gives insight into the exfoliation of layered metal oxides driven by acid-base reaction and helps to understand the exfoliation process in more detail.

Based on the finding of rapid exfoliation of layered metal oxides, the formation of titanium oxide LB films was investigated in terms of reaction time and TBAOH content (***chapter 3***). The results show that the nanosheet concentration at the liquid-air interface (LAI) is not directly correlated with the nanosheet concentration in the bulk of the solution. At short exfoliation time the nanosheet concentration at the LAI is higher than after long exfoliation time even though the nanosheet concentration in the bulk of the solution is much higher after longer time. This finding is important for the fabrication of monolayer nanosheet films by LB deposition.

Complete exfoliation of layered titanates yields nanosheets of different size and quality, because as-synthesized layered titanate crystals are not homogeneous in size and quality. The study of exfoliation under TBAOH deficient conditions shows that exfoliation occurs even at low molar ratios $TBAOH/H^+$ of 1/16. It is shown that it is possible to selectively remove the nanosheets that are of small size and defective under surfactant deficient exfoliation conditions. Furthermore, a study on the influence of LB parameters on the coverage of LB films shows that the coverage is

not determined by the nanosheet concentration, but only by the surface pressure during deposition. In combination with a study on the influence of LB parameters on the coverage of LB films, a step exfoliation process has been established to guide the fabrication of high quality nanosheet films (***chapter 4***).

Efforts were also made to synthesize calcium niobate (CNO) nanosheets with different sizes. By using conventional solid state synthesis and flux synthesis methods, it is possible to synthesize variously sized potassium calcium niobate (KCNO) crystals, which can then be used as precursor for the synthesis of CNO nanosheets. ***Chapter 5*** describes the synthesis of KCNO crystals obtained by flux synthesis with assistance of K_2SO_4 and K_2MnO_4 as flux materials. The KCNO crystals can be protonated and exfoliated into their monolayer nanosheet form. The optimal exfoliation conditions for these crystals is a molar ratio TBAOH/H^+ of 1 - 2. A further study in which these nanosheets were used as seed layers for the fabrication of piezoMEMS demonstrates that large nanosheets improve the longitudinal piezoelectric coefficient (d_{33}).

Although some work has been accomplished, the current findings from research on 2D materials are, only the “tip of the iceberg”. Mysteries and challenges for further exploration remain and this also leaves opportunity for the community. In ***chapter 6***, three scientific issues for further development of 2D metal oxide nanosheets and their thin films applications are presented. Nevertheless, the nanosheet research and application are much wider than as presented in this thesis. It is definitely an interesting research field to work, and there is plenty of work to do.

Samenvatting

Het onderzoek naar 2D-materialen is sterk gegroeid sinds de experimentele ontdekking van grafeen. Een robuuste syntheseroute voor deze nieuwe materialen is cruciaal om ontwikkelingen in het lab om te zetten in praktische toepassingen. Inzicht in het exfoliatieproces van 2D-materialen helpt hierbij. In dit proefschrift worden de resultaten van exfoliatiestudies van gelaagde metaaloxiden en de fabricage van hun Langmuir-Blodgett(LB)-films gepresenteerd. *In situ*-experimenten toonden aan dat de exfoliatie van gelaagde titanaten volgens een ander mechanisme plaatsvindt dan het algemeen aangenomen concept (**hoofdstuk 2**). Het gelaagde titanaatkristal wordt instantaan geëxfolieerd met behulp van een zuur-basereactie, waarna de gevormde 2D-nanoplaatjes snel herstapelen bij hoge concentraties $TBAOH/H^+$. Monolagen van nanoplaatjes konden worden gefabriceerd uit exfoliatieoplossingen met minder dan een minuut exfoliatietijd. Deze ontdekking kan helpen om de fabricagetijd van metaaloxide nanoplaatjes en hun LB-films aanzienlijk te verkorten. De studie geeft inzicht in de exfoliatie van gelaagde metaaloxiden gedreven door zuur-basereacties en helpt het exfoliatieproces meer in detail te begrijpen.

Naar aanleiding van de ontdekking van de snelle exfoliatie van gelaagde metaaloxiden is de vorming van titaniumoxide LB-films onderzocht met betrekking tot reactietijd en TBAOH-concentratie (**hoofdstuk 3**). De resultaten lieten zien dat de concentratie nanoplaatjes op het raakvlak tussen de vloeistof en de lucht (LAI) niet direct gecorreleerd is met de concentratie nanoplaatjes in de bulk van de oplossing. De concentratie nanoplaatjes op het LAI is na korte exfoliatietijden hoger dan na lange exfoliatietijden, terwijl de concentratie in de bulk van de oplossing na lange exfoliatietijden aanzienlijk hoger is. Deze vinding is belangrijk voor de fabricage van monolagen van nanoplaatjes met LB-depositie.

Complete exfoliatie van gelaagde titanaten geeft nanoplaatjes van verschillende grootte en kwaliteit, omdat de gesynthetiseerde gelaagde titanaatkristallen niet homogeen zijn in grootte en kwaliteit. Een studie naar exfoliatie onder TBAOH-deficiënte condities liet zien dat exfoliatie zelfs plaatsvindt bij een lage $TBAOH/H^+$ ratio van 1/16. Tevens is aangetoond dat het mogelijk is om kleine en defecte nanoplaatjes selectief te verwijderen bij exfoliatiecondities met een tekort aan

oppervlakte-actieve moleculen. Een studie naar de invloed van LB-parameters op de dekkingsgraad van LB-films liet zien dat de dekkingsgraad niet bepaald wordt door de concentratie nanoplaatjes, maar alleen door de oppervlaktedruk tijdens de depositie. Een stapsgewijs exfoliatieproces is ontwikkeld voor de fabricage van films van nanoplaatjes met hoge kwaliteit (**hoofdstuk 4**).

Tot slot is de synthese van nanoplaatjes van calciumniobaat (CNO) met variërende grootte onderzocht. Bij gebruik van conventionele vastestofsynthese en synthesis in een flux is het mogelijk om kristallen van kaliumcalciumniobaat (KCNO) te synthetiseren met variërende grootte, die vervolgens gebruikt kunnen worden als precursor voor de synthese van CNO nanoplaatjes. **Hoofdstuk 5** beschrijft de fluxsynthese van KCNO-kristallen met K_2SO_4 en K_2MnO_4 als fluxmaterialen. De KCNO-kristallen kunnen worden geprotoneerd en geëxfolieerd tot nanoplaatjes. Voor deze kristallen is de optimale TBAOH/H^+ molaire ratio 1-2. Een verdere studie waarin deze nanoplaatjes zijn gebruikt als kiemlagen in de fabricage van piëzoMEMS demonstreerde dat grote nanosheets de longitudinale piëzoelectrische coëfficiënt (d_{33}) verbeteren.

Hoewel er voortgang is geboekt, vormen de huidige vindingen in het onderzoek naar 2D-materialen slechts het “topie van de ijsberg”. Er blijven mysteries en uitdagingen voor verder onderzoek en hier liggen mogelijkheden voor de wetenschappelijke gemeenschap. In **hoofdstuk 6** worden drie wetenschappelijke aspecten besproken van de verdere ontwikkeling van metaaloxide 2D-nanoplaatjes en hun toepassingen in dunne films. Desondanks beslaan het onderzoek naar en de toepassingen van nanoplaatjes een veel groter gebied dan wat in dit proefschrift is gepresenteerd. Het is beslist een interessant onderzoeksveld en er moet nog veel werk worden gedaan.

全文总结

随着石墨烯在实验室中被成功制备，二维材料迎来了研究热潮。成熟的制备技术作为二维材料研究中一个关键技术，是推动该类新材料从实验室到实际应用的必经之路。对于剥离过程的深入了解无疑可以帮助建立和发展一种成熟的制备路径。本论文介绍了多项关于对层状金属氧化的剥离以及其 Langmuir-Blodgett (LB) 膜的研究成果。原位实验揭示了层状钛酸盐的剥离过程是不同于目前学术界普遍流行的学说（**第二章**）。该研究发现在酸碱反应的驱动下，层状钛酸盐晶体快速剥离；在高 TBAOH/H^+摩尔比的情况下，得到的二维纳米片会快速地重新堆叠。利用反应时间少于 1 分钟的溶液，单层纳米片 LB 膜可以被成功制备。这些研究成果可以大大地缩短金属氧化物纳米片和其 LB 膜的制备时间；同时，帮助深入了解层状氧化的剥离过程，对设计氧化物纳米片的制备具有指导意义。

基于层状氧化物快速剥离被发现的基础上，本论文介绍了反应时间和 TBAOH 含量对于制备氧化钛 LB 膜的影响（**第二章**）。结果表明在溶液内的纳米片浓度不直接关系到气液界面处的纳米片浓度。虽然长剥离时间的溶液中纳米片浓度远高于短剥离时间的溶液，但是利用短剥离时间制备的纳米片溶液相较长时间剥离的溶液在气液界面处具有更高的纳米片浓度。该研究结果对于氧化物 LB 膜的制备具有重要的意义。

由于高温制备的层状钛酸盐晶体的尺寸和质量不均匀，所以层状钛酸盐的完全剥离会得到不同尺寸和质量的纳米片。在低浓度 TBAOH 条件下对钛酸盐进行剥离的尝试结果显示，即使 TBAOH/H^+摩尔比低于 1/16 剥离也是存在的。利用低浓度 TBAOH 剥离可以选择性地剔除小尺寸和有缺陷的纳米片。另外，LB 实验参数对于 LB 膜的覆盖度研究表明，LB 膜的覆盖度和纳米片的浓度没有直接关系，而是由试验参数表面压力决定的。结合以上两项研究结果，**第四章**中提出了分步剥离法以指导高质量纳米片 LB 膜的制备。

第五章介绍了不同尺寸的铌酸钙盐纳米片的制备方法和其在压电式微机电系统中作为种层的作用。通过利用固相烧结和助溶剂烧结的方法，不同尺寸的铌酸钙钾被成功制备出来，从而作为前驱体用来制备铌酸钙盐纳米片。其

中助溶剂烧结利用了硫酸钾和锰酸钾作为助溶剂。通过助溶剂法得到的铌酸钙钾晶体可以被成功酸化，并继而被剥离成单层纳米片。实验表明酸化的铌酸钙盐的最优剥离条件是在 TBAOH/H^+摩尔比为 1-2 之间. 种层实验表明相较小尺寸纳米片，大尺寸纳米片可以起到增强压电薄膜的纵向压电效应的作用。

虽然本论文介绍了一些关于二维氧化物材料的研究发现，但是当前关于二维材料的发现只是冰山一角。关于二维材料仍然有很多谜团和挑战，这些也为材料界留下很多宝贵的机会。在**第六章**中罗列了关于进一步发展二维氧化物材料及其薄膜应用方面的三个科学议题。不过需要指出的是，纳米片的研究和应用领域远远不止本论文中介绍和提到的。可以肯定地说，二维氧化物领域是一个非常有吸引力的研究领域，并且有许多工作需要去完成。

Acknowledgements

Time flies! I still remember the day when we met Andre in Den Haag 3 years ago, it seems to me that it just happened last week. ***I feel lucky to meet you and choose you as my supervisor, Andre!*** I would never finish this PhD without your supervision. Your encouragement and suggestions helped me to overcome so many challenges I was facing, and will keep guiding me in the road I pursue the answers for more scientific questions. I also would like to thank you for the patience and freedom you gave to me when we had arguments about our subjects.

Many thanks go to all the members (former and current) of inorganic materials science (IMS) group for the help in my research and life. First of all, special thanks go to Minh, Zhaoliang, David, Rogier, Maarten, Roy, Sjoerd, Pablo, I enjoyed the time a lot to work together with you. Your help and collaboration make my scientific journey much easier. Secondly, I would like to thank Guus, Gertjan, Bernard, Dave and Mark for their help and suggestions during my PhD. Experimental assistances from Giuseppe Portale (DUBBLE), Daniel Hermida Merino (DUBBLE), Wim Bras (DUBBLE), Mark Smithers (Nanolab), Rico Keim(Nanolab), Dominic Post, Henk Veldhuis are also much appreciated. Besides, I would like to thank my students Tom Hammer, Marijn van der Putter and Melvin Timmerman for their contributions to this thesis. There are still many people I would like to thank for their helps to my research: Petra, Gerard, Wouter, Kurt, Ben, Werner, Brian……

I would also like to express my gratitude to my committee members, Professor Gerwin Gelinck, Professor Fokko Mulder, Professor Pascal Jonkheim, Professor Rob Lammertink, Professor Gertjan Koster, for their time.

Besides research, I feel lucky to join this group and live in Enschede as one foreigner being far away from home. During my PhD at IMS I have been enjoying the friendly and nice atmosphere, your kindness and being tolerant to a foreigner like me make my life here much easy and colorful. First, I would like to thank Guus, Gertjan, Bernard, Dave and Mark for the help and kindness. And, I would also like to show my gratitude to my officemates, Petra (my paranymph), Boota, Rogier, and Wouter, thank you for all the fun we had. Besides, I would also like to thank our SAXS teams for the valuable experiences during trips to Grenoble in France and during the stay:

Rogier, Pablo, Sjoerd, Roy, Hessel and Alessandro, thank you for the fun and beer. Thanks also go to chemical community for nice time in the lab: Petra, Gerard, Pablo, Rogier, Wouter, Maarten, Sjoerd and Tom, Marijn, Melvin, Bahruz…. Thank you! I am thankful to the rest friends and colleagues at the IMS group and other groups helping me and keeping friendship with me: Zhaoliang, Lin, Jun, Minh, Marion, David, Kees, Dominic, Jose, Laura, Henk, Karin, Nirupam, Tjeerd, Evert, Deepak, Ruud, Ben, Daniel, Jaap, Anirban, Rik, Ron, Alim, Kurt, Werner, Tom, Alexander, Pramodh, Peter, Bouwe, Xin, Kasper, Kai HAN, Jesus, Cindy and friends from Eurekite company for all the friendly atmosphere you created around me. I also would like to thank Prof.dr. F. Bijkerk for taking me into your team as a postdoc. I have been enjoying the time working with Andrey, Sasha, Ben and other group members since I started.

Special thanks go to Marion and Jose. I much appreciate the work you have done for me.

I would like to thank all my Chinese friends in the Netherlands for the nice time and help: Zhaoliang, Lin, Jun, Yunlong, Jinfeng, Zhengchao, ZHANG Sheng family (my paranymph), CHEN Xuelong family, ZHAO Yong, Lijie, Weitao family, WANG Rong, Meiru, Xiaohua, Kai HAN, WANG Yiwei family in Den Haag, Peng Qinxuan in Utrecht and friends in Delft, Qingbao family, Xiaojun, LU Qi family, Weiling family, Xinchao, Zhenpei, Louise…

At the end, I would like to thank my family for their endless and unconditional supports in my home language. 爸爸妈妈，爷爷奶奶，岳父岳母还有姐姐一家，言语已无法表达我对你们的感谢之意。是你们的栽培和鼓励还有支持让我有了向人生新巅峰迈进的勇气！同时要感谢关心我的亲戚和朋友。最后我要感谢我的妻子玲和儿子浩轩，感谢你们的爱和为我远在他乡的生活带来的快乐，特别感谢玲的鼓励，以及为我做出的牺牲和无私的奉献。

Huiyu Yuan / 原会雨

December, 2015

Enschede, the Netherlands